NORTHWESTERN UNIVERSITY

A CALPHAD based approach for modeling the thermodynamics and kinetics of thermoelectric materials

A DISSERTATION

SUBMITTED TO THE GRADUATE SCHOOL

IN PARTIAL FULLFILLMENT OF THE REQUIREMENTS

for the degree

DOCTOR OF PHILOSOPHY

Materials Science and Engineering

By

Matthew Peters

EVANSTON, IL

July 2018

Abstract

A CALPHAD based approach for modeling the thermodynamics and kinetics of thermoelectric materials

Matthew C. Peters

Thermodynamic and kinetic modeling of Pb based chalcogenides in the PbX (X=S,Se,Te) system have been performed. The thermodynamic and kinetic models are based on the CALPHAD method with input from first-principles calculations using density functional theory (DFT) as well as experimental data. These models can be used in the design and optimization of these materials for thermoelectric purposes. In addition, thermodynamic assessments of the A-Q (A=Bi, Sb; Q=Te, Se) systems have been formed and a technique for modeling homologous compounds has been addressed.

Many thermodynamic assessments of the Pb-X systems use stoichiometric models to describe the PbX phase; however, the native defects of the PbX semiconductor create intrinsic carriers that play key roles in optimizing the carrier concentration of the thermoelectrics. First-principles calculations using density functional theory and the dilute limit approximation have been performed to determine the dominant defects in the PbSe compound. The dominant defects were found to be Pb and Se vacancies for Se-rich and Pb-rich growth conditions, respectively. The formation energies of the defects were calculated along with the total number of defects and compared to experimental data in the literature, which agree in type, but differ in overall magnitude from the first-principles calculations.

To get a more accurate thermodynamic description of the intrinsic carriers, CALPHAD assessments have been performed using a five-sublattice (5SL) model and a simpler two-sublattice (2SL) model. Each model contains parameters used in the optimization that can be linked to

physically measurable constants or values that can be derived from first-principles or experiments. The two models agree well with each other as well as the experimental and DFT data. The 2SL model was used to build a thermodynamic database for the pseudobinaries and pseudoternary Pb(S,Se,Te) system. In addition, Na doping in the PbX phase has been calculated via first-principles and incorporated into the CALPHAD models.

A kinetic assessment of the PbS-PbTe has been performed using experimental data derived from a diffusion couple. A forward simulation method was used to determine the interdiffusivities from the annealed composition profiles. The interdiffusivities were used to build a mobility database, which agrees reasonably well with the experimental data.

Lastly, an overview of how these models can be used to optimize thermoelectric materials has been given. The lattice thermal conductivity can be modeled using the Debye-Callaway model, which can be used to determine an optimal particle size for a second phase dispersion. A single parabolic band model is used to describe the transport properties dependence on the carrier concentration, which can be determined from the previously determined phase diagram. The thermodynamic and kinetic databases can then be used with PrecipiCalc to determine appropriate annealing times to achieve desired microstructure. Annealed microstructures of the Pb(Te,S) system indicate that this material does not go through homogenous nucleation but instead a discontinuous precipitation process that deserves further investigation.

Acknowledgements

The amount of people I need to thank and the gratitude I would like to show could probably rival the length of this dissertation, but I will attempt to keep it brief.

This work would not have been possible without the guidance from my advisor Prof. Peter Voorhees. He has not only modeled excellent scientific research skills but also those of an exemplarily leader. His constant support, feedback, and mentorship allowed me to grow and I always appreciated his support to pursue activities in and outside of the lab, especially his support for interning at SpaceX, which is where I will find myself next.

I also had outstanding support from my thesis committee. Prof. Greg Olson provided the opportunity to further my management experience by allowing me to participate as a 390 coach and gave excellent feedback to my teams' reports. Prof. Jeff Snyder invited me to attend and present at his group meetings, which greatly helped improve my knowledge of thermoelectrics. Lastly, Dr. Ursula Kattner introduced and taught me about CALPHAD, which plays a fundamental role in my dissertation. My work greatly benefited from collaborating with all of these great minds.

The past five years at Northwestern were greatly enriched by my peers and colleagues. I am thankful to the rest of the Voorhees group who helped provide feedback on presentations and were always available to toss ideas around, both scientific and non-scientific alike. I have had the wonderful opportunity to work with many people through various organizations such as The Leadership Fellowship, QuesTek LLC, and Lunch Club for which I am truly grateful. I would be remiss to not acknowledge my Tulane experiences and would like to thank my undergraduate friends from Clara Street as well as my undergraduate advisor Dr. Bahram Khoobehi.

This work was made possible by Northwestern University through the Center for Hierarchical Materials Design (CHiMaD) and financial support from the DARPA SIMPLEX

program through SPAWAR (Contract #N66001-15-C-4036). I was also supported by the Department of Defense (DoD) through the National Defense Science & Engineering Graduate Fellowship (NDSEG) Program.

Lastly, I would like to thank my family. Through all the change that has occurred over my life, you all have been the one constant. To Alex, for always looking after me and even confronting my sixth-grade math teacher who thought I wasn't ready for the accelerated group. To Aaron, who I got to share my time at NU with and was always a scientific inspiration. To Garrett, who never complained about doing the 10 hour round trip drive up from St. Louis to visit his brothers. To Mom, for taking me to every single science demo growing up and making sure I had every educational opportunity available. And to Dad, for modeling what a hard work ethic is and what it means to have a Commitment to Excellence. I owe so much to all of you and love you all.

Table of Contents

List of Figures

List of Tables

1. Introduction

Human history has been sequenced by its interaction and use of materials. From the Stone Age followed by the Bronze, Iron, and now what some refer to as the Silicon Age, our technological progress has been shaped by the materials society uses. Therefore, the advancement of human civilization depends on the focus and development of new materials. In fact, many of the Grand Challenges for Engineering outlined by the National Academy of Engineering can be addressed with novel materials, such as improving the efficiency of solar cells or increasing the access to clean water[1].

Unfortunately, the traditional development and optimization of new materials is an economic and time intensive endeavor. Often, decades pass between when a new material is discovered and its eventual commercial use due in large part to a dependence on trial and error testing. To address this issue, the Obama administration launched the Materials Genome Initiative (MGI) in order to support the development of tools, databases, and best practices to reduce the time to market for new materials[2]. The MGI is a wide ranging, collaborative effort between experimentalists, theorists, and data scientists that hopes to lay the groundwork for how the future research of materials should be conducted.

One of the most promising practices for the development of new materials is an approach known as Integrated Computational Materials Engineering (ICME), which focuses on the interplay between experiments and computational methods to model the process-structure-property-performance relationship[3, 4]. Computational materials research has progressed enough to the point where optimal compositions or processing conditions can be predicted and tested, thereby eliminating many unnecessary tests. The models and databases can be further fine-tuned with additional experimental testing, which in turn leads to a more narrow and focused experimental

conditions to explore. The two practices have a symbiotic relationship and are able to produce far more together than they ever could separately. Companies that have embraced ICME practices, such as Ford, General Electric, Boeing, and Toyota, have reported returns on investment to be over 7:1 and a significant reduction in development time of new materials[3]. ICME methodologies can range from using machine learning on large datasets to determine promising unexplored compositional spaces, to a narrowed focus on the optimal microstructure for a given alloy.

One of the most fundamental tools for ICME related projects is a well-established thermodynamic database, which functions as a "genome". The knowledge of the thermodynamics of a system allows for the creation of phase diagrams, from which, essential information can be determined and calculated. Although the thermodynamics dictate the final equilibrium state of the system they are also required for modeling the kinetics of an evolving system. There are many ways to model the thermodynamics of the system but one of the most accepted techniques is through the CALPHAD (CALculation of PHAse Diagrams) method[5]. The CALPHAD method is a semi-empirical approach that models the Gibbs free energy of various compounds based on available experimental data. Recent efforts have sought to include data from first-principles calculations in order to supplement the experimental data that is either unavailable or not measurable in the laboratory setting[6]. This practice creates more physically appropriate models, which are necessary for phase diagrams as well as more accurate extrapolation into higher ordered systems.

The CALPHAD method has had wide use and acceptance in the metallurgical field; however, its use in semiconductors is much more limited and therefore an area that requires further advancement. A particularly interesting group of semiconductors that would benefit from an ICME motivated optimization are thermoelectric materials. Their unique ability to convert temperature

gradients into electricity allow them to be used in waste heat recovery efforts[7]. Nearly 60% of our energy use is lost to waste-heat, therefore, thermoelectrics could play a key role in addressing our growing energy needs[8]. Thermoelectrics are also able to convert electrical currents into temperature differences, thereby offering a solid-state heating and cooling solution. Despite the fact that these materials have such interesting properties and have been known since the late 1800's, they have only been used in very niche applications, where cost is not a limiting factor. Their widespread adoption is limited by their low efficiency, which is usually described by its zT value, calculated as:

$$zT = \frac{S^2 \sigma T}{\kappa} \quad (1.1)$$

Where S, σ, T, and κ are the Seebeck coefficient, electrical conductivity, temperature, and thermal conductivity, respectively. It is thought that a zT value of 3 is necessary in order for thermoelectrics to be economically feasible; however, current high performing materials only approach 2.5[9].

Optimizing these materials has proved to be difficult as the individual properties are all intrinsically linked such that beneficially changing one will adversely affect another resulting in no increase in zT. As an example, the Seebeck coefficient and electrical conductivity are both functions of the carrier concentration as depicted in Figure 1.1[10]. Increasing the carrier concentration generally increases the electrical conductivity, which simultaneously decreases the Seebeck coefficient. Despite this, there are some proven methods for increasing the overall zT. The power factor, defined as $S^2\sigma$, can be optimized through carrier concentration tuning[11]. This is exemplified by the carrier concentration and power factor relationship depicted in Figure 1.1, for which there exists a maximum in the power factor at a given carrier concentration. The thermal conductivity has contributions from the electronic and lattice components. The lattice thermal

conductivity can be reduced through hierarchical structuring that introduces defects such as grain boundaries, precipitates, and point defects that scatter heat-carrying phonons of various wave lengths[12]. Careful consideration of the defects results in a decrease of the thermal conductivity without adversely affecting the other variables. Lastly, band engineering where thermoelectrics are alloyed with other elements in order to beneficially alter their band structure has also increased their transport properties[13]. The carrier concentration of a semiconductor is a function of the amount of intrinsic and extrinsic defects of the system, which can be determined by the phase diagram[14]. In addition, the volume fraction of precipitates and degree to which a material can be alloyed are also found from the phase diagram. Therefore, knowledge of a thermoelectric's phase diagram and the thermodynamics play a fundamental role in predicting optimizing these novel materials[15] and will be the focus of this work.

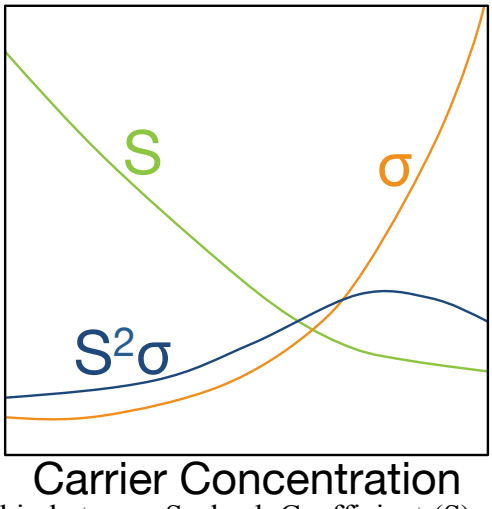

Figure 1.1: General relationship between Seebeck Coefficient (S), electrical conductivity (σ) and power factor ($S^2\sigma$) vs. carrier concentration

Chapter 2 of this dissertation focuses on first-principles calculations of the binary PbSe system to determine what the dominant defects are as well as provide fundamental inputs for the CALPHAD models discussed later. These calculations are a necessary step in order to build our models and help to ensure the CALPHAD parameters are physically consistent. Chapter 3

introduces and compares two CALPHAD models, a 5-sublattice (5SL) and 2-sublattice (2SL) model, used in building the thermodynamic databases and their descriptions of the intrinsic carriers of the binaries in the PbX (X=S,Se,Te) system are discussed. Chapter 4 provides a thermodynamic description of the pseudobinaries and pseudoternary of the PbX system, as well as the Na solubility limits in the individual compounds and extrapolation to higher ordered systems. Chapter 5 discusses the kinetic modeling using the established thermodynamics of the PbS-PbTe system and new kinetic database. Chapter 6 explores how the models built for the PbX system can also be applied to other thermoelectric materials in the A-Q (A=Bi,Sb; Q=Se,Te) systems as well as a method for modeling homologous compounds that are found in many thermodynamic assessments. Lastly, Chapter 7 provides an outline for how these models can be used in the design of a thermoelectric material and what future work should be done in order to optimize these thermoelectric materials.

2. First-principles calculations for understanding defects in the PbSe system

2.1 Introduction

Defects are often responsible for many interesting and desirable properties of materials. They can provide strengthening mechanisms, alter the diffusion of the system, or affect the solubility limits of compounds[16]. In the case of semiconductors, one of the most important roles of defects are to produce the charge carriers of the system[17]. Defects can be defined as either intrinsic, which are native to the specific compound, or extrinsic, which are introduced as dopants. Defects come in many forms from interstitials, antisites, or vacancies and can vary in charge state. The number of different possible combinations makes the analysis and determination of the type of defect quite difficult. There are experimental methods for determining both the type and charge of defects, but they rely on indirect observation and complex analysis techniques[18]. The implementation of first-principles calculations allows researchers to have direct control of the defects and charge state of the system, which is impossible to obtain experimentally[19]. In addition to being a powerful tool of its own, first-principles calculations have also been shown to effectively complement CALPHAD model development by providing physically relevant data that is not accessible through experiment[6].

The calculation of defects in semiconductors via first-principles calculations has garnered much attention. Density functional theory (DFT) has been used to show that unwanted *n-type* conductivity in ZnO originates from impurities in the source material, in lieu of the previously thought intrinsic defects[20]. This was done by comparing the formation energy of the intrinsic defects, which were generally large, to that of common impurities. Hydrogen interstitials as well as hydron substituting on the O site were both shown to be shallow donors and likely the cause of

the *n-type* conductivity. This was an unexpected result as hydrogen often changes charge state depending on the growth condition but had consistent donor-like behavior in ZnO. Ensuring growth conditions in a hydrogen poor environment would thus reduce the likelihood of unintentional *n-type* doping. First-principles calculations have also been used to predict the carrier concentration in Pb-based chalcogenides[21, 22]; however, careful consideration of the functionals within DFT are necessary due to the well-known "band-gap problem". The most common functionals used in DFT, local density approximation (LDA) and the generalized gradient approximation (GGA), are inaccurate at predicting band-gaps, causing errors in the formation energy, to be discussed below [23].

Incorporating first-principles calculations into CALPHAD models is becoming increasingly common[24, 25]. CALPHAD assessments depend on phase diagram as well as thermochemical data in order to build physically accurate models. Often times, this requires knowing the thermodynamics of phases in either unstable structures or compositions, which are unable to be determined experimentally. Work arounds include approximating these values, although this is no longer necessary with the implementation of first-principles calculations[5]. DFT calculations can provide the enthalpies of formation of various compounds and has been used to successfully model a number of systems, including Al-Sr[26], Al-Ca[27], and Cu-Si[28] to name a few. First-principles calculations can also be used to determine the enthalpy of mixing of random solid solutions using special quasi-random structures (SQS) as in the Al-Mg system[29], as well as model the magnetic properties and magnetic transitions found in α-Ce and γ-Ce[30].

In order to accurately model thermoelectric compounds, we first need to gain insight into what the dominant carriers of the system are. In addition, the parameters in the CALPHAD models can be linked to physical properties such as the formation energy of a defect as well as ionization

energies[31]. Thereby, we can ensure that the models developed here are physically reasonable by fixing parameters to the DFT determined values or comparing the final optimized parameters to those calculated from first-principles. In this work, the carrier concentration of binary PbSe has been investigated under the dilute-limit approximation in order to determine the dominant defects, carrier concentration, and formation energy as determined by DFT.

2.2 Dilute-limit Approximation

In order to determine the dominant defects of the system, the formation energy of defects in the system must be known. First-principles calculations have been successfully used in similar systems and that approach has been used here[21, 22]. The dilute-limit approximation is used to determine the formation energy and concentration of the defects in the PbSe system. The formation energy of a defect is calculated as[19]

$$\Delta E_f^j(\Delta\mu, \Delta\mu_e) = \left[E^j - E^0\right] - \sum_{i=1}^{N} \Delta N_i^j(\mu_i^0 + \Delta\mu_i) - \Delta N_e^j(E_{VBM} + \Delta V_{PA} + \Delta\mu_e) + \Delta E_{IC} \quad (2.1)$$

where E^0 and E^j are the total energies of the defect-free and defect containing supercell for defect j, respectively. ΔN_i^j is the number of atoms of type i removed (ΔN_i^j<0) or added (ΔN_i^j>0) from the system. μ_i^0 is the chemical potential of atom i in its standard reference state (fcc for Pb and hexagonal for Se) and $\Delta\mu_i$ is the change in chemical potential of element i relative to its standard reference state dependent on the equilibrium conditions, i.e. Pb-rich or Se-rich. Similar to ΔN_i^j, ΔN_e^j is the number of electrons added or removed from the system, where ΔN_e^j is greater than zero for electrons added to the system and less than zero for electrons removed from the system. E_{VBM} is the energy of the valence band, ΔV_{PA} a potential alignment term, and $\Delta\mu_e$ the Fermi level of the system relative to the E_{VBM}. Lastly, ΔE_{IC} is an image charge correction term. The parameters

E^0, E^j, μ_i^0, $\Delta\mu_i$, and E_{VBM} can all be derived from the DFT calculations, ΔV_{PA} and ΔE_{IC} are post-processing correction terms, and $\Delta\mu_e$ can numerically be solved for as described below.

The chemical potentials of Pb and Se are given by their DFT determined total energies in their stable structure at 298 K and 1 atmospheric pressure, known as their stable-element reference (SER) state. The chemical potential, μ_i, is unchanged when in equilibrium with the SER of atom *i*. Therefore, under Pb-rich conditions, the chemical potential of Pb is equal to μ_i^0 and $\Delta\mu_i$ is equal to zero. Since there are no other stable phases in equilibrium with PbSe other than the SER of Pb and Se, the chemical potential of Se is then fixed by the chemical potential of PbSe, μ_{PbSe}, which is calculated from the chemical potential of its constituents, μ_{Pb} and μ_{Se}[18]:

$$\mu_{Pb} + \mu_{Se} = \mu_{PbSe} \quad (2.2)$$

Under Pb-rich conditions the chemical potential of μ_{Se} is reduced from its SER. The same process can used to determine the change in chemical potential of a Pb atom in a Se-rich environment in equilibrium with hexagonal Se. Since these are the only two solid phases in equilibrium with PbSe, no further adjustment of the chemical potentials is necessary.

To determine the concentration of defects, the formation energies of the defects and thus the Fermi level of the system must be known. To fix the Fermi level, the charge neutrality condition must be enforced

$$\sum_j \Delta N_e^j n_j + n^- - p^+ = 0 \quad (2.3)$$

where , n_j is the number of defects *j* per formula unit, and n^- and p^+ are the concentration of electrons and holes respectively. To determine the number density of electrons and holes under the

rigid band approximation, the density of states, $g(E)$, determined via first-principles calculations, can be multiplied by the Fermi function and integrated over the appropriate energy levels:

$$n^{-}(T,\Delta\mu_e) = \int_{E_g}^{\infty} g(E) \frac{1}{1+e^{(E-\Delta\mu_e)/k_BT}} dE \quad (2.4)$$

$$p^{+}(T,\Delta\mu_e) = \int_{-\infty}^{0} g(E) \frac{1}{1+e^{(\Delta\mu_e-E)/k_BT}} dE \quad (2.5)$$

where E and k_b are the energy of the system and Boltzmann constant, respectively. All energies here are relative to the valence band maximum and E_g is the band gap of the host material. The concentration of point defects n_j is given by a simple Arrhenius equation under the dilute-limit approximation[19]

$$n_j(T,\Delta\mu,\Delta\mu_e) = N_{site}^{j} e^{-\Delta E_f^j/k_BT} \quad (2.6)$$

where N_{site}^{j} is the number of possible sites for defect j in the formula unit and ΔE_f^j is calculated using equation 2.1. Equations 2.4, 2.5, and 2.6, are combined with the charge neutrality condition, equation 2.3, which yields the Fermi level, $\Delta\mu_e$, for a given temperature. This allows for the enthalpy of formation as well as concentration of electrons, holes, and other defects to then be determined.

2.3 Correction Schemes

The creation of charged defects in a supercell calculation requires correction terms. To ensure charge neutrality conditions are not violated, a background neutralizing charge is introduced, which affects the potential of the calculation[32]. The shift in potential means that the energy levels

of a defect containing supercell and a defect-free supercell are not directly comparable and thus an adjustment, taking the form of a constant offset, is required. By assuming that the electrostatic potential far away from the defect should be identical to that of the host cell, the offset can be determined. The offset is determined by calculating the average difference in electrostatic potential around each atom in the supercells between the defect cell, $\overline{V_{el,\iota}^{d}}$, and the perfect cell, $\overline{V_{el,\iota}^{0}}$, at a distance greater than or equal to one half the distance between periodic image defects,

$$\Delta V_{PA} = \frac{1}{N}\sum \left(\overline{V_{el,\iota}^{d}} - \overline{V_{el,\iota}^{0}}\right) \quad (2.7)$$

In this study, the value ΔV_{PA} for various defects ranges from near zero to approximately 0.15 eV in magnitude. The largest offset was found to be -0.13 eV for a negatively charged (-2) vacancy on the Pb site, which is shown in Figure 2.1(a) for Va_{Pb}^{-2} and Figure 2.1(b) for Va_{Se}^{+2}.

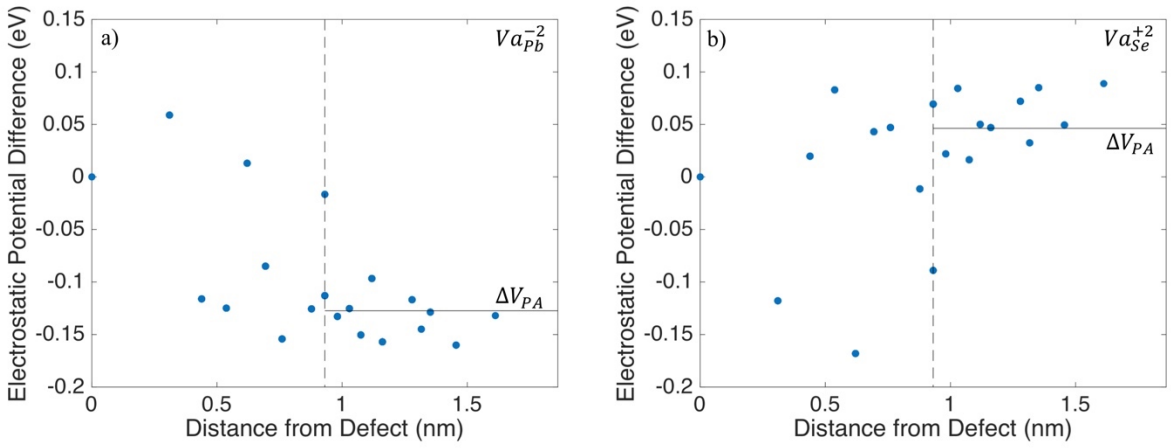

Figure 2.1: The potential alignment term for defects a) Va_{Pb}^{-2} and b) Va_{Se}^{+2}. The potential alignment is determined by averaging the difference in electrostatic potential from the defect and defect-free supercell for atoms equal to one half of the unit cell away for the defect.

In addition to the potential alignment term, we must also correct for the defect-defect interactions that occur due to the periodic boundary conditions. The corrections are determined

through a Makov-Payne expansion, which is given to third order in L for a 3-D array of length, L[33]

$$\Delta E_{IC} = \frac{q^2 \alpha}{2L\eta} + \frac{2\pi qQ}{3L^3\eta} + O(L^{-5}) \quad (2.8)$$

where α is the Madelung constant (1.75) of the periodic array of defects, Q the second radial moment of the charge density, η the dielectric constant, and q the charge of the defect. The dielectric constant is calculated to be 232 for PbSe, which agrees with the room temperature value of 204. This large dielectric constant drastically reduces the image correction term such that it has a negligible effect on the formation energies, as has been seen in other studies[22] [21] [34].

2.4 Computational Methodology

The total energies of the perfect and defect containing supercell were determined by DFT[35] [36] calculations performed with the Vienna Ab-initio Simulation Package[37] (VASP) [38] with projector-augmented wave[39] (PAW) potentials utilizing the generalized gradient approximation (GGA) exchange-correlation functional of Perdew, Burke, and Ernzerhof[40] (PBE). These calculations treat the $6s^2 6p^2$ and $4s^2 4p^4$ electrons as valence in the Pb and Se atoms, respectively. The NaCl crystal structure for PbSe was taken from the Inorganic Crystal Structure Database[41] (ICSD). For the defect calculations, 3 x 3 x 3 supercells were created from the conventional unit cell of PbSe and contain 216 total atoms. Structures were allowed to relax with a maximum cutoff energy of 350 eV and Monkhorst-Pack 4 x 4 x 4 k-point meshes[42]. These parameters were determined to converge the defect formation energies to within 15 meV with respect to cutoff energies and Monkhorst-Pack k-point meshes. Lattice parameters and atomic positions were allowed to relax until energy convergence reached 0.1 meV and a final static calculation was

performed to determine the total energy. The dielectric constant was calculated using density functional perturbation theory implemented in VASP and includes ionic contributions[43-45].

2.5 DFT Calculations

In order to determine the dominant defects in PbSe, both antisite, vacancy, and interstitial defects ranging in charge from -2 to +2 are considered. Equations 2.1 and 2.3-2.6 are used to solve for the Fermi level, from which defect formation energies and concentration of defects as a function of temperature are determined. The temperature dependence comes from the Arrhenius expression for the concentration of defects as well as the change in density of states. The range of Fermi levels, calculated by the charge neutrality condition as a function of temperature and equilibrium conditions, are shown in Figure 2.2. The Fermi level under Se-rich conditions approaches the valence band maximum, causing *p-type* carriers in the system. Conversely, under Pb-rich conditions, the Fermi level lies much closer to the conduction band resulting in *n-type* carriers. This result matches the qualitative results of the carriers found in experimental investigations, which determined *p* and *n-type* carriers for Se-rich and Pb-rich growth conditions, respectively[46].

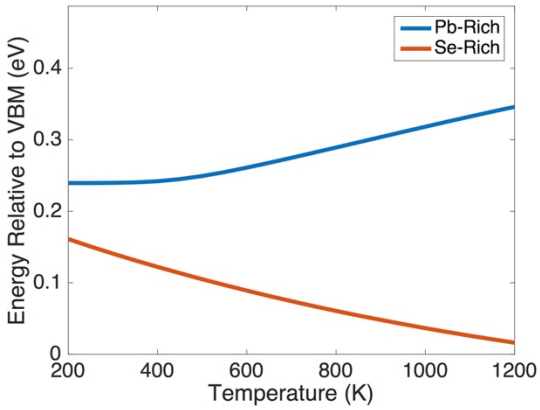

Figure 2.2: Calculated Fermi level as a function of temperature. Fermi levels are calculated by enforcing charge neutrality at a given temperature.

The formation energies of various defects as functions of the Fermi level are shown in Figure 2.3. The temperature-dependent Fermi levels calculated from the charge neutrality condition are also shown through the green shaded region. Under Pb-rich conditions, the defect Va_{Se}^{+2} is the lowest formation energy for all Fermi energies. Similarly, the Va_{Pb}^{-2} defect is lowest in Se-rich conditions. These are consistent with the results found in both the PbS and PbTe systems in similar studies[22] [21, 47]. In addition, the doubly ionized vacancies are consistent with experimental evidence for vacancies playing the dominant role as defects within this system. Ohashi ruled out interstitial defects as playing a role and identified vacancies as the dominant defects in their selenium partial pressure effects on carrier concentration investigation [48]. This result is also in agreement with Chou's study, whose maximum solubility measurements could only be explained if vacancy defects were assumed[49].

The ionization energy, or transition energy, of the doubly ionized vacancies required for the CALPHAD model can also be calculated from these figures. The ionization energy of a defect is the Fermi level at which the neutral defect and charged defect are the same[20]. The ionization energy of Va_{Pb}^{-2} and Va_{Se}^{+2} are -0.13 eV and 0.49 eV relative to the valence band maximum,

respectively. Due to the disagreement of the DFT calculated band gap of 0.487 eV and the temperature dependent experimental band gap of 0.275 eV at 300 K[50], these transition energies are scaled as a fraction of the DFT derived band gap and converted to an equivalent fraction of the experimental band gap to be used in the 5SL model[22] to be discussed later.

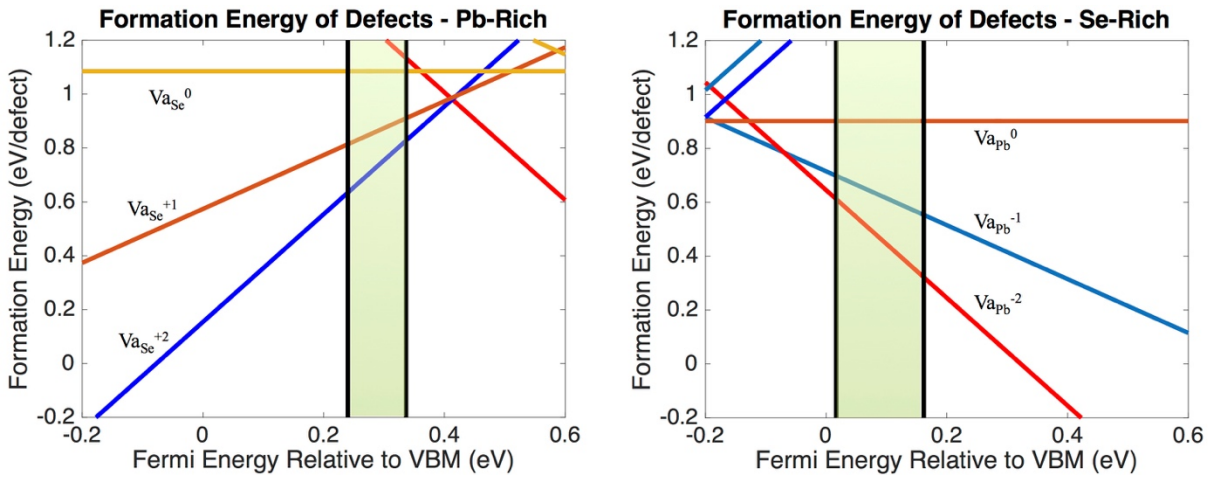

Figure 2.3: Formation energies of various defects as predicted by DFT as a function of the Fermi energy relative to the valence band edge (VBM). By enforcing charge neutrality, a range of possible Fermi levels can be determined as shown in the shaded region. Doubly-ionized vacancies have the lowest formation energy in either condition.

The DFT predicted carrier concentrations are shown in Figure 2.4 along with experimental data from several studies[46, 49, 51, 52]. The calculations are in qualitative agreement with the experimental data. However, the DFT calculations under predict the experimental carrier concentration in the Pb-rich condition and over predict it in the Se-rich regime. The slope, with respect to inverse temperature, agrees well with experiment; nonetheless, the magnitude of carriers is in slight disagreement for Pb-rich and even more so in Se-rich conditions. This discrepancy is likely due to the difference in equilibrium conditions in the experiment, where PbSe is in equilibrium with liquid Pb and Se. Conversely, the calculations only take into account being in equilibrium with solid Pb or Se. In addition, the disagreement between the calculated and room

temperature band gap could also play a role. Calculations that include spin-orbit coupling (SOC) could provide greater accuracy as they more accurately predict the band gap of these materials, but are much more computationally expensive[53]. Nonetheless, the agreement between the slope of the calculations and experimental data should provide confidence that our enthalpies of formation, as given in Table 2.1 for various defects are accurate.

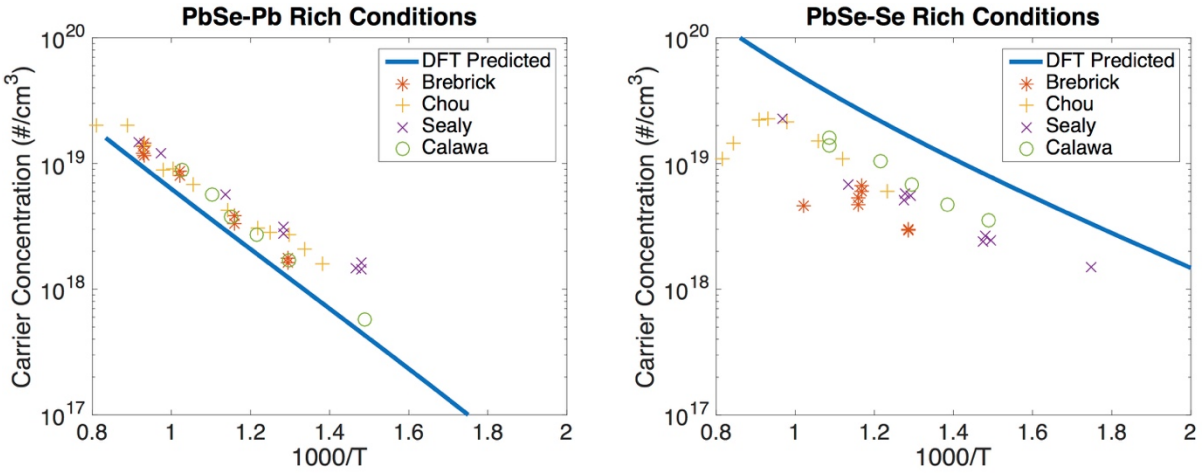

Figure 2.4: DFT predicted carrier concentrations with experimental data. The calculations agree qualitatively; however, disagree on the magnitude. This could be due to the difference in equilibrium conditions, as much of the experimental data is in equilibrium with the liquid, or the error in the predicted band gap.

Based on these results, the CALPHAD model will consist of doubly ionized vacancies on the Pb and Se lattice, along with their associated neutral defects that will serve as optimizing parameters for the 5SL model. The formation energies of neutral vacancies has also been calculated, which are not affected by the error in band gap measurements as their formation energies are independent of the Fermi level according to equation 2.1. The 5SL model uses non-degenerate semiconductor physics to describe the Gibbs free energy of electrons and holes of the ionized system. The neutral defects serve as reference values for the end-members containing

unionized defects and the DFT energies are used as a starting point for the optimization, listed in Table 2.1.

Table 2.1: Formation values as calculated by DFT in Pb-rich and Se-rich growth conditions.

PbSe Formation Energies at 300 K as Determined by DFT (eV/defect)		
Defect	Pb-Rich Conditions	Se-Rich Conditions
Va_{Se}^{+2}	0.59	1.60
Va_{Se}^{+1}	0.82	1.90
Va_{Se}^{0}	1.08	2.25
Va_{Pb}^{-2}	1.33	0.32
Va_{Pb}^{-1}	2.59	0.55
Va_{Pb}^{0}	2.06	0.90
Va_{Pb}^{+1}	2.59	1.35

Recent work has outlined the difficulty in accurately calculating the correct carriers in narrow bandgap semiconductors using GGA potentials. In the work done by Doak et al[21], which also calculated the formation energy of Na defects in various charge states in PbTe and PbS, they found that some Na defects had negative formation energies, which would not be physically reasonable. They attributed this to a possible unknown ternary compound that existed below the convex hull that when taken into account would have increased the formation energy of the compounds due to a change in the chemical potential of the individual elements. Later work done by Bajaj et al[34] determined that these anomalous negative formation energies were created by delocalized electron states caused by unexpected charge defects. The delocalized electrons would compensate the unexpected charge state, resulting in a configuration which would be representative of the correct charge state. Therefore, only defects with expected charge states, determined by simple electron counting, should be used in these calculations. To address this issue, the calculations above have been repeated using only expected charge states (i.e. doubly ionized vacancies, interstitials, and antisites). The formation energies under this condition remain

unchanged for Va_{Se}^{+2} and Va_{Pb}^{-2}, which can be attributed to the fact that the defect formation energies of the other defects are higher and therefore do not contribute many carriers, thereby not affecting the charge neutrality condition.

The inaccuracy of band gap calculations from GGA potentials is a well-known problem. In order to better calculate the band gap, more accurate potentials can be used. The effect of various potentials on PbTe has been studied and determined that only hybrid functions (HSE) that utilize spin-orbit coupling (SOC) and GW theory are capable of accurately predicting the carriers in PbTe[23]. The calculations here could be improved by using this higher-level theory, but at a much greater computational cost. For example, the calculations done in the work done by Goyal[23] were done on a 64-atom supercell as opposed to 216-atom supercell used in this study. The smaller cell size required to utilize the more complex potentials may introduce errors that cancel out the increased accuracy. Lastly, the discrepancy in band gap determined by GGA vs experiment in PbTe is much larger than the discrepancy in PbSe and therefore we would expect the error to be mitigated in PbSe as well.

2.1 Conclusions

The intrinsic defects of PbSe have been investigated via first-principles calculations using DFT. Vacancy, antisite, and interstitial defects were all taken into account and the doubly ionized vacancies on the Pb and Se site under Se-rich and Pb-rich conditions, respectively, were found to be the defects of lowest energy. The Fermi level was determined by enforcing charge-neutrality and the concentration of the defects was determined. PbSe shows *n-type* and *p-type* conductivity for Pb-rich and Se-rich growth conditions, matching experiment. The magnitude of carriers differs from experiment, but the slope and thus formation energy of the primary defects are in agreement with experiment. Methods for improving these calculations using more accurate potentials were

discussed; however, the agreement between the first-principles calculation and experiments are sufficient here. Knowledge of the primary defects as well as some of the physical properties such as defect formation energies, are necessary for building an accurate CALPHAD model to be explained in the next chapter.

3. CALPHAD Modeling of binary semiconductors

3.1 Introduction

The thermodynamics of a system lay the groundwork for addressing many materials-based problems as it dictates the equilibrium state the system is trying to achieve. The stability of certain phases in a given set of conditions is determined by the thermodynamics and often represented as a phase diagram. These phase diagrams play a fundamental role in any investigation of materials and a plethora of information can be determined from an accurate phase diagram. The thermodynamics also play a key role in more complex processes such as determining the driving force for nucleation of a second phase or determining the chemical potentials, which are necessary for simulating diffusion in materials[5]. It is clear that any study of materials must first start with a solid foundation of its thermodynamics.

There are many ways to model the thermodynamics of the system, each of which contains their own pros and cons. In Chapter 2, first-principles calculations using DFT were discussed as a method for predicting both the type and concentration of carriers in the system. Although a very powerful tool, first-principles calculations have their own limitations, which were discussed in the previous chapter. Mainly, the fact that first-principles are determined from fundamental laws and quantities makes them extremely inflexible. Correction schemes and more accurate exchange potentials can be used to improve the accuracy of the calculations, but there is limited leeway if the calculations are in contradiction to experiment[18]. A much more flexible method for modeling the thermodynamics of a system is through the CALPHAD (CALculation of PHAse Diagrams) method, which uses models that consist of adjustable parameters[5]. These parameters can then be optimized to describe either experimental data or first-principles calculations. These parameters

allow CALPHAD models to be much more flexible in describing the thermodynamics of a system than first-principles calculations alone.

CALPHAD models are generally built from assessments of individual systems and start from a bottom-up approach where unaries are used to build binaries, then ternaries and beyond[54]. The added flexibility of the CALPHAD method allows for the development of multicomponent thermodynamic databases. If appropriate models are selected and the models are fit to accurate data, then CALPHAD models can be used to extrapolate into higher ordered systems, which have not been assessed. The reliability of the extrapolation relies on the accuracy of the constituent subsystems, so careful attention should always be made to the models and experimental data used in CALPHAD assessments.

The fundamental thermodynamic property of interest in most CALPHAD assessments is the Gibbs free energy, which is determined at constant temperature and pressure, consistent with many experiments[55]. The Gibbs free energy of a phase, α, is calculated from a sum of individual components

$$G_m^\alpha = {}^{srf}G_m^\alpha + {}^{phys}G_m^\alpha - T^{cnf}S_m^\alpha + {}^{E}G_m^\alpha \quad (3.1)$$

The first term represents the "surface of reference" and is the Gibbs free energy of the unreacted components, ${}^{phys}G_m^\alpha$ contains any contributions from physical models, such as magnetic or electronic contributions, ${}^{cnf}S_m^\alpha$ is the configurational entropy due to ideal mixing, and ${}^{E}G_m^\alpha$ is an excess term for all other contributions.

One of the most basic phases to model is one for which composition is constant. In this case, the Gibbs free energy is only dependent on pressure and temperature. When pressure is constant, the Gibbs free energy can be modeled with a power series in temperature as

$$G_m^\alpha - \sum_i b_i H_i^{SER} = a + bT + cTln(T) + dT^2 + eT^3 + fT^{-1} + \cdots \quad (3.2)$$

where b_i is the stoichiometric factor of element i in α, H_i^{SER} is the enthalpy of element i in its stable element reference (SER) state, and coefficients a through f are fitting parameters. Basic thermodynamic relationships can be used to determine the relationships between the coefficients and physically measurable quantities. The enthalpy of formation, entropy, and heat capacity can all be determined by:

$$H_m^\alpha - \sum_i b_i H_i^{SER} = a - cT - dT^2 - 2eT^3 + 2fT^{-1} + \cdots \quad (3.3)$$

$$S_m^\alpha = -b - c(1 + \ln(T)) - 2dT - 3eT^2 + fT^{-2} + \cdots \quad (3.4)$$

$$C_p^\alpha = -c - 2dT - 6eT^2 - 2fT^{-2} + \cdots \quad (3.5)$$

Therefore, if the enthalpy of formation or heat capacity is measured experimentally or via first-principles calculations, the coefficients in the power series can be used to describe the data and the Gibbs free energy of the phase is determined.

For more complicated phases that exist over a range of compositions the compound energy formalism (CEF) is most commonly used[56]. In the CEF, a phase is separated into a number of sublattices, often dictated by the crystal structure, and elements, known as components, are allowed to populate specific sublattices. A phase containing two equal sublattices with components A, B, C, and D where components A and B are on the first sublattice and C and D on the second, can be written as (A,B)(C,D). According to the CEF, the Gibbs free energy is calculated as

$${}^{srf}G_m^\alpha = y_A' y_C'' \ {}^\circ G_{A:C} + y_A' y_D'' \ {}^\circ G_{A:D} + y_B' y_C'' \ {}^\circ G_{B:C} + y_B' y_D'' \ {}^\circ G_{B:D} \quad (3.6)$$

$$^{cnf}S_m^{\alpha} = -R[y_A'\ln(y_A') + y_B'\ln(y_B') + y_C''\ln(y_C'') + y_D''\ln(y_D'')] \quad (3.7)$$

$$^{E}G_m^{\alpha} = y_A'y_B'y_C''L_{AB:C} + y_A'y_B'y_D''L_{AB:D} + y_A'y_C''y_D''L_{A:CD} + y_B'y_C''y_D''L_{B:CD} + y_A'y_B'y_C''y_D''L_{AB:CD} \quad (3.8)$$

where y_i' and y_i'' are the site fraction of component *i* on the first and second sublattice, respectively. The terms $^{\circ}G_{i:j}$ are commonly referred to as end-members and represent the Gibbs free energy of a phase where the first and second sublattices are completely filled with components *i* and *j*. These end-members are modeled using an equation similar to equation 3.2 as they represent phases of fixed composition. Often times, these phases are either unstable or metastable and difficult to measure experimentally. There are a number of different approximations to describe aspects of these end-members, such as the Kopp-Neumann rule, which can be used to estimate the heat capacity; however, first-principles calculations can now be used to fix any unknown values. Lastly, the term $L_{i,k:j}$ are interaction parameters that describe the mixing of components *i* and *k* on the first sublattice, with a filled second sublattice of component *j*. Analogous relationships apply for the other interaction parameters. The interaction parameters are often modeled using Redlich-Kister polynomials, which in a binary system is defined as

$$L_{ij} = \sum_{v=0}^{k}(x_i - x_j)^v \, {}^vL_{ij} \quad (3.9)$$

where x_i is the mole fraction of component *i*. The Redlich-Kister polynomial is a very flexible power series that has the added benefit of approaching zero near the compositional extremes where there is no mixing.

It's clear that careful consideration needs to be done when selecting appropriate models and the parameters within the model. The flexibility of these models allows for the same data to be modeled in many different ways. Although qualitatively the models may appear to describe the

data similarly, they may predict vastly different data when used in other systems or predicted data in its own system.

This chapter performs CALPHAD assessments of the semiconductor compounds found in the Pb-Te, Pb-S, and Pb-Se systems. Although the systems have recently been assessed by Bajaj et al.[22], Huang et al.[57], and Liu et al.[58], respectively, the aim of this chapter is to improve the accuracy of the PbX (X=Se,S,Te) semiconductor through a five-sublattice model specifically developed for binary semiconductors[59]. This model can reproduce both phase stability as well as carrier concentrations, which are of the utmost importance for describing electronic materials. This model utilizes both experimental and first-principles calculations and shows a large improvement over previous models, and are the first time PbS and PbSe have been assessed using the CEF. In addition to the 5SL model, a two-sublattice model is also developed for compatibility in multicomponent databases. The 2SL parameters can be similarly linked to first-principles data. This chapter first reviews the data in the literature, describes the models used, and discusses the results of the CALPHAD assessments.

3.2 Literature Review

3.2.1 PbTe

The thermodynamics and off-stoichiometric nature of PbTe has been studied extensively. Due to the extremely narrow homogeneity range of this compound, typical metallographic techniques for measuring the solubility cannot be used. Instead, measurements of the carrier concentration through Hall coefficients, coupled with assumptions of the defects, determine the solubility limits. There are a number of such studies done in this way for PbTe. One of the first such studies was conducted by Brebrick and Allgaier[14]. In this study, ingots of PbTe with either Pb or Te rich compositions were heat treated at various temperatures and quenched. Hall constants

were then calculated at room temperature to determine the carrier concentration. A later study by Brebrick and Gubner questioned the previous study's results due to Cu impurities in the Pb-rich samples. The study was repeated; again with Pb-rich and Te-rich ingots and Hall coefficients measured 273 K[60]. In the same year, Scanlon also measured the carrier concentrations at lower annealing temperatures, from 453 K to 673 K[61].

Harman studied the $Pb_{1-x}Sn_xTe$, $Pb_{1-x}Sn_xSe$, and $PbS_{1-x}Se_x$ systems through single crystals grown via Bridgman technique[62]. At the same time, Hewes et al. were also investigating the $Pb_{1-x}Sn_xTe$ system[63]. Their results largely agreed with previous ones, though there were large deviations in carrier concentrations at higher temperature in Te-rich samples. The discrepancy was thought to be due to measuring the Hall coefficient at 77 K instead of 273 K[63]. Despite discrepancies in absolute magnitude, all studies agreed that Te-rich samples exhibited *p-type* conduction and Pb-rich samples *n-type*.

An explanation for the discrepancy at high temperature for Te-rich samples was first proposed by Albers et al.[64], who believed that quenching of these materials above a certain temperature was ineffective in maintaining their equilibrium states due to the material's low thermal conductivity. This was finally proved by Mühlberg and Hesse using TEM by confirming the presence of Te precipitates when quenching from high temperature[65]. They determined that the temperature at which equilibrium was not maintained due to inefficient quenching to be approximately 798 K. Thus, any measurements above this temperature on Te-rich samples were not included in this study. Schenk et al. circumvented this problem by calculating the carrier concentration *in situ* at higher temperatures[66]. Their numbers are orders of magnitude higher than the ones previously reported and have not been replicated, therefore, we have chosen not to include them during the optimization.

Carrier concentration experiments are useful in determining the number of defects in a material; however, they give no insight into the nature of the defects. Measurements of the effect of partial pressure on the carrier concentration have been used in the past to provide insight into the type of defects in a system[67]. First-principle calculations can now provide us with the energies of formation of a multitude of different charged and neural defects within the system. Recent studies by Doak et al. and Bajaj et al. have determined that the lowest formation energy under Te-rich and Pb-rich conditions are doubly charged Pb and Te vacancies, respectively[21]. These calculations are based on the dilute-limit approximation, where formation energies are determined by energy differences in defect containing and defect-free supercells. Care has to be taken when dealing with charged defects in first-principle calculations due to the long-range electrostatic interactions that arise in periodic boundary conditions. Both studies use similar correction terms to address this issue. Their final values for formation energies vary (i.e. the formation energy of a doubly-ionized Pb vacancy in Te-rich conditions are 0.35 and 0.53 eV/atom for [22] and [21], respectively), but are in qualitative agreement. These calculations could be improved with the use of spin-orbit coupling to better describe the experimental band-gap, but are computationally expensive on supercells of these sizes. To be consistent between PbTe and PbS, this study will use values from Doak et al, as it contains information on both the PbS and PbTe system. Therefore, our model uses these defects as the predominant ones. Similar choices have been made for non-CALPHAD models with success[68].

3.2.2 PbS

The Pb-S system has been studied very similarly to the Pb-Te system. Most studies involve single crystals annealed at high temperature in either Pb-rich or S-rich environments, followed by a quench, and subsequent Hall measurements. The results by Bloem and Kroger[69], Nensberg

and Petrov[70], and Chou et al.[49] are all in close agreement. However, similar to the PbTe system, Albers et al. determined that Bloem and Kroger were not able to maintain the equilibrium concentration of PbS above 973 K when quenching[64]. Therefore, we did not include their data, along with Nensberg and Petrov, and Chou et al. as they are all in close agreement and therefore equally questionable. No data points below 973 K are provided for either study and therefore, cannot be used.

Strauss calculated the carrier concentration of *n-type* PbS by quenching Bridgman-grown single crystals[71]. Their data is in disagreement with the previously mentioned Nensberg and Petrov and Bloem and Kroger data, which was attributed to the latter's unsuccessful quench and incorrect anneal times. Data from Strauss was used in a later study by Harman, who supplemented it with *p-type* data below 973 K[62]. These two experiments are used to optimize the parameters for the PbS semiconductor models.

PbS also has very similar defect chemistry to PbTe. Again, first-principle calculations have shown that doubly charged vacancies in PbS exhibit the lowest formation energies in the system[21, 72, 73]. In addition, the doubly charged vacancies have been used previously in other models with success[74] and therefore will be used for modeling the defects in PbS.

3.2.3 PbSe

The studies done for PbSe are analogous to those done for PbTe and PbS. The homogeneity region of PbSe is too narrow, making direct measurement difficult, therefore the homogeneity must be inferred from carrier concentration data. Brebrick and Gubner were some of the first to measure carrier concentrations of single crystal PbSe annealed in either Pb-rich or Se-rich conditions, which were determined to be *n-type* and *p-type*, respectively[46]. A similar study done by Calawa et al.[51] is in good agreement with Brebrick's data, though the identification of the

defect was still unknown. Chou et al. determined that vacancies must be the dominant carriers by plotting the observed maximum solid solubility of PbSe against temperature and carrier concentration, which showed better agreement with a vacancy mechanism than the antisite model[49]. In addition, the lattice parameter decreased for compounds grown in either Pb-rich or Se-rich, conditions, which is indicative of a vacancy mechanism. The carrier concentration measurements done by Sealy and Crocker later are also in agreement with the previous studies' data[52]. Although insufficient quenching should be considered in the PbSe compounds, the carrier concentrations monotonically increase with temperature and therefore does not play a large role and no data needs to be excluded.

A thermodynamic model that describes the off-stoichiometry was developed by Ngai and a resulting phase diagram presented by Lin[75]. It should be noted that an inconsistency in the formula used to convert carrier concentration to solubility limits, used in previous studies, results in a homogeneity range that is twice as large as expected. A recent CALPHAD assessment done by Liu et al treats PbSe as a stoichiometric compound[58]. However, the assessment shows good agreement with the experimental data and its parameters for the liquid and stoichiometric PbSe are used in this study.

3.3 CALPHAD Modeling

3.3.1 5-Sublattice Model

The CALPHAD method has been used several times to describe the Pb-Te system, notably by Kattner et al. [76] and even more recently by Gierlotka et al. [77], and Bajaj et al. [22]. The crystal structure of PbTe, PbS and PbSe are all NaCl B1[50], which is generally modeled using two sublattices, one for each atomic site. Gierlotka modeled PbTe using a two sublattice anti-site model. First-principle calculations indicate this to likely not be the most accurate model, as

formation energies for antisite defects are larger than vacancies. This was improved in Bajaj's assessment, which correctly placed vacancies on either sublattice. The stoichiometric PbTe and associate liquid models show excellent agreement between the description and experimental information, therefore we chose to use Bajaj's description of the liquid and stoichiometric PbTe in our own optimization. The full phase diagram of the Pb-Te system is shown in Figure 3.1. The Pb-S system has not been so thoroughly investigated via the CALPHAD method. A recent assessment by Huang et al. is the only CALPHAD study of note, although it models PbS as a stoichiometric compound[57]. This phase diagram is shown in Figure 3.2. Similarly, there is a recent Pb-Se assessment that treats the PbSe phase as stoichiometric. This is shown in Figure 3.3.

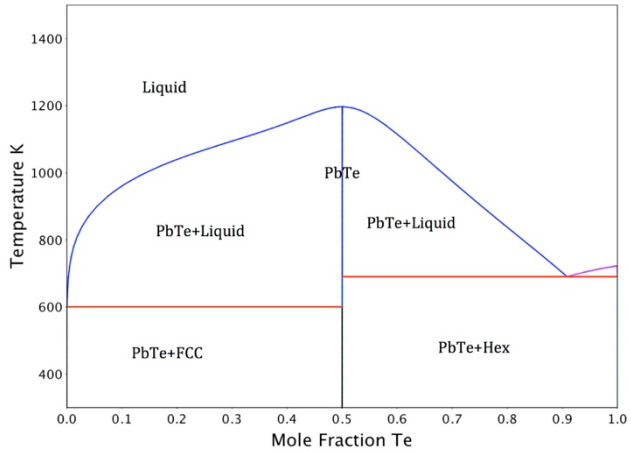

Figure 3.1: Full Pb-Te Phase Diagram taken from Bajaj 's assessment[22]

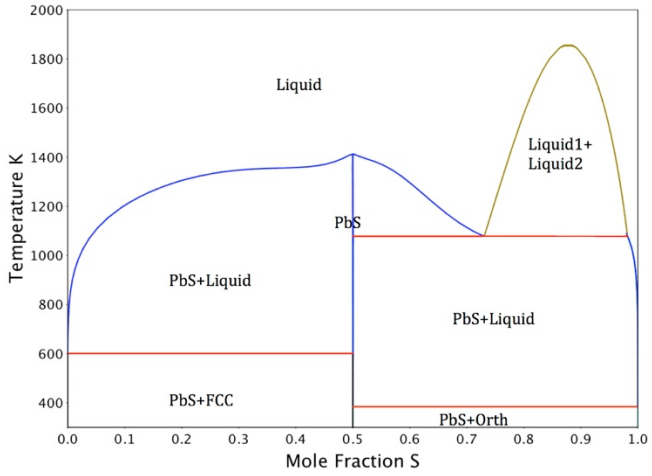

Figure 3.2: Full Pb-S Phase Diagram taken from Huang's assessment[57]

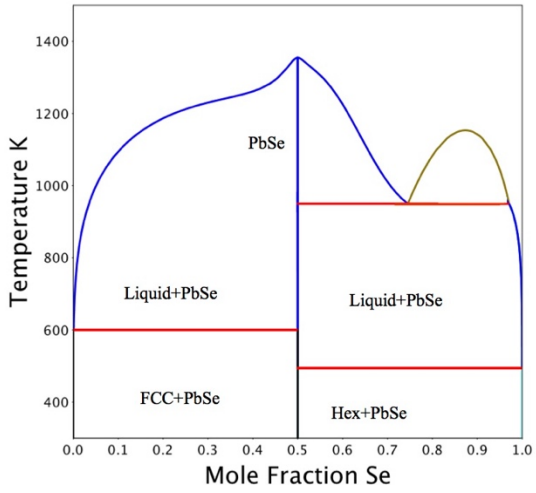

Figure 3.3 Full Pb-Se Phase Diagram taken from Liu's assessment [58]

The goal of this study is to implement the five-sublattice model for semiconductors developed by Chen et al. for PbTe, PbS, and PbSe[59]. The five-sublattice model uses the Wagner-Schottky defect model and compound energy formalism (CEF) to better describe carrier concentration and defect energies. The model has its roots in the species chemical potential/bond energy (SCPBE) model developed by Oates et al.[78]. Chen transformed that model into the CEF formalism, which can be easily implemented in programs such as ThermoCalc. Chen then used

this model to successfully model the semiconductor compounds GaAs[79] as well as CdTe[59]. It has also been used for the GaN semiconductor[80] and recently for ZnO[81].

The five sublattice model for the PbX (X=S,Se,Te) is given as: (**Pb**,Va,Va^{-2})(**X**,Va,Va^{+2})(**Va**)(**Va**,e^{-1})(**Va**,h^{+1}), where the first, second, third, fourth, and fifth sublattices are for the Pb, X, interstitial, electrons, and holes respectively. Mathematically the CEF is given below:

$$G^{\mathrm{PbX}} = \sum_i \sum_j \sum_k \sum_l \sum_m y_i^{Pb} y_j^{X} y_k^{I} y_l^{e} y_m^{h} G_{ijklm} + \mathrm{RT}\left(\sum_i y_i^{Pb} \ln y_i^{Pb} + \sum_j y_j^{X} \ln y_j^{X} + \sum_k y_k^{I} \ln y_k^{I} + \sum_l y_l^{e} \ln y_l^{e} + \sum_m y_m^{h} \ln y_m^{h}\right) \quad (3.10)$$

Where y_i^s represents the site fraction of *i* on sublattice *s*, R is the gas constant, and T is temperature. The interstitial sublattice will not be used in this study, but is kept for completeness and for possible ternary extrapolations. The introduction of charged species within this model add an additional constraint when the Gibbs free energy is minimized. In addition to the usual requirement that the total amount of components is constant and that all site fractions sum to one for individual sublattices, all phases must be electrically neutral. With five sublattices, the number of end-members in this model becomes 36. Chen et al. describe how to reduce the number of optimized end-members, which will be given below.

The creation of an electron and hole pair is given by[79]:

$${}^{0}G_{PbXVae^{-1}Va} + {}^{0}G_{PbXVaVah^{+1}} = 2\ {}^{0}G_{PbXVaVaVa} + \mathrm{E_g} - \mathrm{RT}(\ln \mathrm{N_c} + \ln \mathrm{N_v}) \quad (3.11)$$

E_g is the band gap energy of PbX, $G_{PbXVaVaVa}$ are taken from the stoichiometric descriptions in Bajaj and Huang's assessments, and N_c and N_v are the effective density of states for non-degenerate semiconductors given by:

$$N_{c,v} = 2\left(\frac{2\pi m_{c,v}{}^* k_b T}{h^2}\right)^{3/2}\left(\frac{a^3}{4}\right) \quad (3.12)$$

where $m_{c,v}{}^*$, k_b, h, and a are the effective masses of the electron and holes, Boltzmann constant, and lattice parameters respectively. The parameters for PbX used in these equations are given in Table 1. E_g is temperature dependent for PbX and increases with temperature, but there is limited data on the high temperature dependence. The band gap plateaus above 500 K, therefore, the band gap at 500 K is used here as a constant at higher temperatures[50]. A reference state for the energy levels of the charge carriers must be chosen. Due to the non-degenerate behavior of these semi-conductors, the middle of the band gap, where the assumed Fermi energy is an appropriate choice and one used by convention in previous assessments using this model [59, 78, 79, 81]. Using this reference, the Gibbs free energy for the end members containing electrons and holes can be determined using equation 3.12[59]:

$${}^0G_{PbXVae^{-1}Va} = {}^0G_{PbXVaVaVa} + \frac{E_g}{2} - RT\ln N_c \quad (3.13)$$

$${}^0G_{PbXVaVah^{+1}} = {}^0G_{PbXVaVaVa} + \frac{E_g}{2} - RT\ln N_v \quad (3.14)$$

Charged defects are modeled with respect to their neutral end-member defects as well as the creation of their respective charge carrier and ionization energies. Since doubly charged vacancies

are the dominant defects in the system, each charged defect end-member creates two charge carriers and are calculated as[59]:

$$^{0}G_{Va^{-2}XVaVaVa} = {}^{0}G_{VaXVaVaVa} - 2\,{}^{0}G_{PbXVaVah^{+1}} + 2\,{}^{0}G_{PbXVaVaVa} + \Delta E_{V_{Pb}^{-2}} \quad (3.15)$$

$$^{0}G_{PbVa^{+2}VaVaVa} = {}^{0}G_{PbVaVaVaVa} - 2\,{}^{0}G_{PbXVae^{-1}Va} + 2\,{}^{0}G_{PXVaVaVa} + \Delta E_{V_{X}^{+2}} \quad (3.16)$$

The values $\Delta E_{V_{Pb}^{-2}}$ and $\Delta E_{V_{X}^{+2}}$ represent the ionization energies or defect transition energies of vacancies on the Pb and X sublattice with respect to the valence and conduction band, respectively. The transition energies used are those determined at 0 K by first-principle calculations and are assumed to be constant at higher temperature. These energies are calculated by determining the chemical potential of an electron at which the formation energy of the neutral defect and charged defect are equal to one another[20]. In the PbX system, the transition of importance is between that of the neutral vacancy and its charge state of $^{+/-}2$. The ionization energies can therefore be calculated from the given energies in[21] and the values are summarized in Table 3.1. Due to the discrepancy between the experimental and DFT calculated band gaps, these chemical potentials have been scaled by the ratio of their respective DFT values.

$$\frac{\mu_{e,DFT}}{E_{g,DFT}} = \frac{\mu_{e,exp}}{E_{g,exp}} \quad (3.17)$$

Therefore, we can determine the experimental chemical potential at which ionization occurs by solving for $\mu_{e,exp}$ in Equation 8 above.

Table 3.1: Physical parameters used in the five-sublattice model for PbX (X=S,Te) semiconductors

Model Parameter	PbTe	PbS	PbSe
E_g (ev)	0.360[a]	0.472[a]	0.329[a]

m_e^*	0.30 m_0[b]	0.39 m_0[c]	0.27[e]
m_h^*	0.36 m_0[b]	0.38 m_0[d]	0.27[e]
a (nm)	0.6462[a]	0.5936[a]	0.612[a]
$\Delta E_{V_{Pb}^{-2}}$ (ev/defect)	-0.011	-0.097	-7,000
$\Delta E_{V_X^{+2}}$ (ev/defect)	0.19	0.18	55.0
a)[50] b) [82] c) [83] d) [84] e) [85]			

The reciprocal relation, utilized commonly in CALPHAD assessments, is used to calculate end-members that contain two defects on the first two sublattices. Due to the large amount of end-members without physical meaning, no experimental information, and to not introduce a miscibility gap, we assume the reciprocal energy is equal to zero[5] and the end-members are calculated as:

$$^{0}\mathrm{G}_{\mathrm{ijVaVaVa}} = {}^{0}\mathrm{G}_{\mathrm{iXVaVaVa}} + {}^{0}\mathrm{G}_{\mathrm{PbjVaVaVa}} - {}^{0}\mathrm{G}_{\mathrm{PbXVaVaVa}} \quad (3.18)$$

End-members with three or more defects are set equal to 0. This is a safe assumption to make, as these end-members will have very small contributions to the total Gibbs free energy, due to the small amount of site fractions of the constituents on sublattices. Therefore, the pre-factor in Equation 1 of these end-members will be near zero and therefore any reasonable number can be used.

There are only two remaining end members that require optimization, which represent the neutral defects on the first two sublattices. They are given as:

$$^{0}\mathrm{G}_{\mathrm{PbVaVaVaVa}} = {}^{0}G_{Pb}^{fcc} + \mathrm{V}_1 + \mathrm{V}_2\mathrm{T} \quad (3.19)$$

$$^{0}\mathrm{G}_{\mathrm{VaXVaVaVa}} = {}^{0}G_{X}^{SER} + \mathrm{V}_3 + \mathrm{V}_4\mathrm{T} \quad (3.20)$$

where the functions ${}^{0}G_i^{SER}$ are the Gibbs free energies in their standard elemental reference state given by Dinsdale[86]. The variables V_1 to V_4 are the optimizing parameters used to fit to the experimental data.

3.2.2 2-Sublattice Model

The 5SL model remains interesting from a scientific perspective as it contains many of the physical parameters used in semiconductors physics. The model is based on the grand-canonical approach, which is the preferred method for calculating defects in binary and ternary systems[31]. However, it has limited capability for developing a multicomponent database as the structure-based end-members are optimized from system specific information. Therefore, there is incompatibility between the end-member ${}^{0}G_{\mathrm{PbVaVaVaVa}}$ in the PbTe, PbS, and PbSe systems. To address this, a two-sublattice (2SL) model will be developed that is compatible in multi-component databases.

The 2SL model is described as (Pb,Va)(X,Va) and due to the vacancies, great care needs to go into determining the end-members and interaction parameters[31]. The PbX system can be split into two regions by the stoichiometric composition. Along the Pb-rich solidus, the site fraction of X vacancies will be orders of magnitude larger than Pb vacancies and as such can be assumed to be equivalent to the model (Pb)(X,Va). This reduces the degrees of freedom to one: the site fraction of vacancies or X atoms on the X sublattice. To determine the equilibrium concentration of X the grand potential must be minimized:

$$\mathcal{G}_m = G_m - \mu_{Pb} y_{Pb} - \mu_X y_X \quad (3.21)$$

where $\mathcal{G}_m$, μ_{Pb} and μ_{Te} are the grand potential per mole and chemical potential of Pb and Te atoms respectively. According to the CEF, G_m with only one excess term is calculated as

$$G_m = y_X \ {}^{\circ}G_{PbX} + y_{Va} \ {}^{\circ}G_{PbVa} + \mathrm{RT}\big(y_X \ln(y_X) + y_{Va} \ln(y_{Va})\big) + y_X y_{Va} L_{X,Va} \quad (3.22)$$

Taking the derivative of equation with respect to y_X and since μ_X is constant in the two-phase region, and setting the result to zero leads to

$$0 = \frac{dG_m}{dy_X} - \mu_X \quad (3.23)$$

Substituting the derivative of equation 3.22 with respect to y_X into equation 3.23 leads to

$$- \ {}^{\circ}G_{PbVa} + \ {}^{\circ}G_{PbX} + L_{X,Va}(1 - 2y_X) - \mu_X = \mathrm{RT}\ln\left(\frac{y_X}{1-y_X}\right) \quad (3.24)$$

Finally, the equilibrium concentration of vacancies can be determined by substituting $1 - y_{Va}$ for y_X and assuming a dilute concentration, where $y_{Va} \ll 1$

$$y_{Va_X}^{eq} = \exp\left(-\frac{{}^{\circ}G_{PbVa} - \ {}^{\circ}G_{PbX} + L_{X,Va} + \mu_X}{\mathrm{RT}}\right) \quad (3.25)$$

The numerator of equation 3.25 represents the formation energy of a vacancy per mole, which can be determined from first-principle calculations. The key advantage of this is that the formation energy is split into a structure specific term ${}^{\circ}G_{PbVa}$, which can be used in all PbX systems, and a system specific term $L_{X,Va}$ which can be changed to fit the first-principle or experimental data unique to the system. The chemical potential of μ_X is fixed in a two-phase region at a given temperature. Therefore, once a value for ${}^{\circ}G_{PbVa}$ is agreed upon, only the interaction parameter must be adjusted. A similar analysis for X-rich conditions determines the equilibrium site fraction of Pb vacancies as

$$y_{Va_{Pb}}^{eq} = \exp\left(-\frac{{}^{\circ}G_{VaX} - {}^{\circ}G_{PbX} + L_{Pb,Va} + \mu_{Pb}}{\mathrm{RT}}\right) \quad (3.26)$$

The modeling of end-members containing vacancies is a known issue that has been frequently discussed[31, 87, 88]. First attempts at modeling end-members containing vacancies assigned them values of zero, which can cause them to stabilize at extremely high temperatures[88]. To fix this, a positive and generally temperature dependent, value must be used for modeling vacancies. Rogal's review article suggests using a value of 2.3RT as a penalty value. This value was chosen as a method for making sure that the concentration of vacancies on a sublattice would not exceed 0.1 at which point the crystal would likely collapse. Dinsdale recently recommended a value of 30T for convenience, as it is both positive and increasing with temperature[88]. Franke analyzed the concentration of vacancies in tungsten and determined that the description needed to exceed the value of $\ln(2-1/2)\mathrm{RT}$ for there to be a unique solution for the vacancy concentration[87]. His final recommendation is a value of 0.2RT. For this study, the Gibbs free energy of Pb or X in their standard elemental reference state and the value of 2.3RT is chosen for end-members containing vacancies due to the reasonable assumption that the site fraction should not exceed 0.1 and to ensure that PbX does not become stable on the Pb or X end of the phase diagram.

The defect containing end-members for the 2SL model are then given as:

$${}^{0}\mathrm{G}_{\mathrm{PbVa}} = {}^{0}G_{Pb}^{fcc} + 2.3\mathrm{RT} \quad (3.27)$$

$${}^{0}\mathrm{G}_{\mathrm{VaX}} = {}^{0}G_{X}^{SER} + 2.3\mathrm{RT} \quad (3.28)$$

$$^{0}G_{VaVa} = 4.6RT \quad (3.29)$$

and the interaction parameters can be linked to the energy of formation through equation 3.25 and 3.26

$$L_{Pb,Va} = G^{f}_{Va_{Pb}} - {}^{\circ}G_{VaX} + {}^{\circ}G_{PbX} - \mu_{Pb} \quad (3.30)$$

$$L_{X,Va} = G^{f}_{Va_{X}} - {}^{\circ}G_{PbVa} + {}^{\circ}G_{PbX} - \mu_{X} \quad (3.31)$$

The interaction parameters are given start values based off the first-principle calculations for the energies of formation and are allowed to vary to fit the experimental data. In this model, the assumption is made that for every Pb vacancy two holes are created. Likewise, every X vacancy results in the creation of two electrons.

3.4 Results and Discussion

The PARROT[89] module in ThermoCalc[90] was used to optimize the parameters V_1 to V_4 for PbTe, PbS, and PbSe. The temperature independent terms V_1 and V_3 represent the formation energy of the neutral vacancies on the X and Pb sites, respectively. These values for PbTe and PbS were provided from the authors of[21] as they were calculated in their recent study, but are not explicitly given in the paper due to their high formation energy compared to the other defects. The values for PbSe were determined in the previous chapter. Values for these calculations are found in Table 3.2. Optimizations that converged far from these values were deemed inaccurate and not used. The experimental carrier concentrations previously discussed were then used to fit the parameters.

3.4.1 PbTe

The final optimized end-members for PbTe are given in Table 3.2 along with the initial values calculated from first-principles at 0 K. The carrier concentration of holes and electrons in PbTe along with the experimental data is given in Figure 3.4 and Figure 3.5, respectively. For comparison, the recent assessment by Bajaj, assuming that each Pb and Te vacancy creates 2 holes and electrons, respectively, is also provided. In each case, the new five-sublattice model has a much better fit to the data.

Table 3.2: Final optimization end-members for PbTe and PbS semiconductors. The first-principle calculations are used as starting values for the temperature independent term in the Gibbs free energy and are taken from a recent study[21]. All units J/mol.

End-Member	Optimized End-Member	First-principle Calculation
PbTe		
${}^{0}\mathrm{G}_{\mathrm{PbVaVaVaVa}}$	${}^{0}G_{Pb}^{fcc} + 143{,}576 + 62.8T$	127,000
${}^{0}\mathrm{G}_{\mathrm{VaTeVaVaVa}}$	${}^{0}G_{Te}^{hex} + 98{,}408 + 79.2T$	115,000
PbS		
${}^{0}\mathrm{G}_{\mathrm{PbVaVaVaVa}}$	${}^{0}G_{Pb}^{fcc} + 92{,}724 + 75.2T$	96,000
${}^{0}\mathrm{G}_{\mathrm{VaSVaVaVa}}$	${}^{0}G_{S}^{orth} + 112{,}427 + 82.7T$	83,900
PbSe		
${}^{0}\mathrm{G}_{\mathrm{PbVaVaVaVa}}$	${}^{0}G_{Pb}^{fcc} + 118{,}661 + 68.7\mathrm{T}$	105,000
${}^{0}\mathrm{G}_{\mathrm{VaSeVaVaVa}}$	${}^{0}G_{Se}^{Hex} + 98{,}482 + 84.3\mathrm{T}$	87,000

Table 3.3: Final optimized interaction parameters for the PbX system. Using equation 3.30 and 3.31, the formation energy can be calculated and compared to the DFT value. These parameters coupled with equations 3.29 are used for modeling PbX.

Interaction Parameter	Optimized Value (J/mol)	CALPHAD Determined Formation Energy at 300 K (J/mol)	DFT Predicted Formation Energy at 300 K (J/mol) [21]
$L_{Pb,Va:Te}$	38,070+2.4T	44,500	51,100
$L_{Pb:Te,Va}$	72,780-10.8T	75,300	82,900
$L_{Pb,Va:S}$	38,570+4.4T	40,400	36,600
$L_{Pb:S,Va}$	38,944+4.6T	46,100	75,100
$L_{Pb,Va:Se}$	37,954	42,000	31,000
$L_{Pb:Se,Va}$	45,585	51,000	57,000

The carrier concentration of holes and electrons (p and n) can be converted to solidus points via the equation[91, 92]:

$$X_m = 0.5 + \frac{(p-n)\mathrm{M_{PbX}}}{4Z\rho\mathrm{N_A}} \quad (3.32)$$

where M_{PbX} is the molecular weight of PbX, Z is the ionization of the defect, in this case 2, ρ is the density, and N_A Avogadro's number. Using this formula, the data has been converted to solubility limits and the off-stoichiometric nature of PbTe is shown in Figure 3.6.

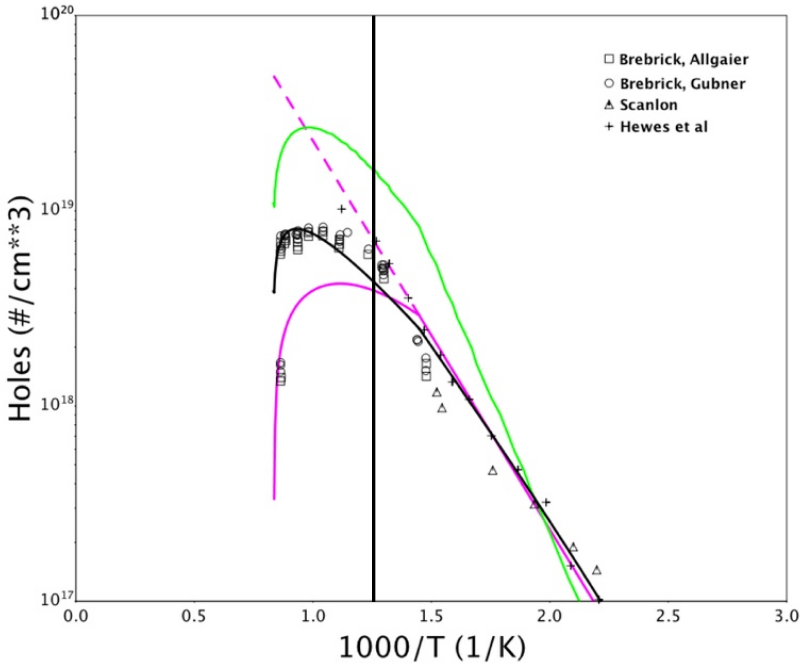

Figure 3.4: Carrier concentration of holes under Te-rich conditions and experimental data points for PbTe. Data points above 800 K were not used in this assessment indicated by the vertical black line. Bajaj's assessment shown as green line, the 5SL in black and the 2SL model shown in magenta. The dashed magenta line shows the same calculation with the liquid phase suspended and shows much better agreement with the high temperature data.

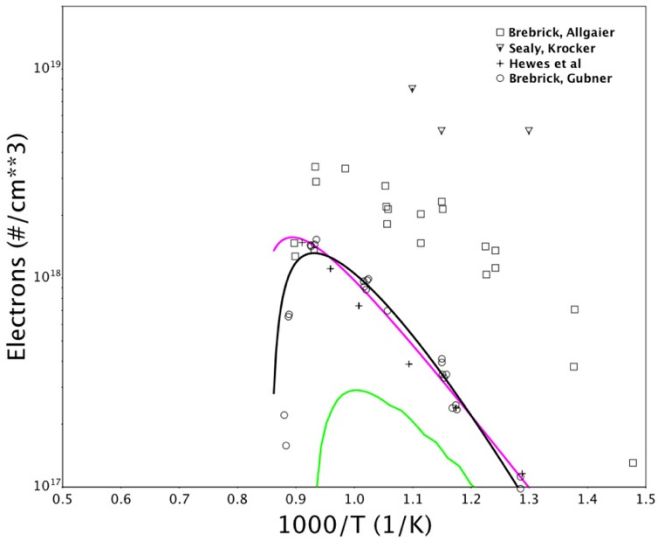

Figure 3.5: Carrier concentration of electrons under Pb-rich conditions and experimental data points for PbTe. Bajaj's assessment shown as green line, 5SL in black, and the 2SL model shown in magenta.

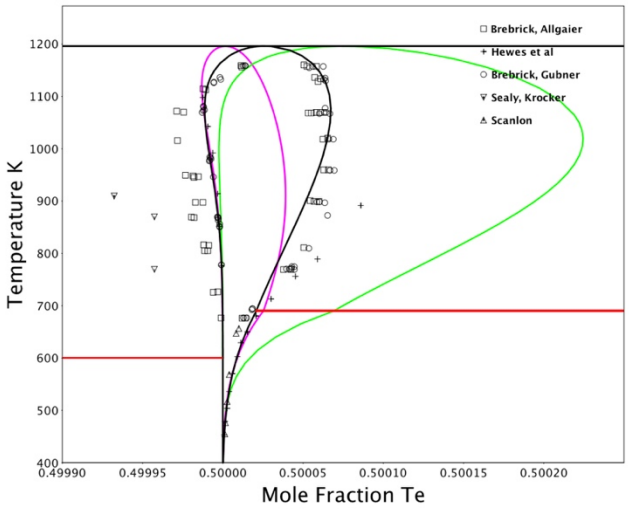

Figure 3.6: Enlarged region of Pb-Te phase diagram to show solubility of PbTe. Data points above 800 K on the Te-rich side were not used in this assessment. Bajaj assessment shown as green line, the 5SL in black, and the 2SL model shown in magenta.

A second model of PbTe was also used in this assessment that contained Te^{0} and Te^{+2} antisite defects on the Pb sublattice. This was investigated due to the formation energy of the Te^{+2} defect energy (0.90 eV/defect) being only slightly larger in the Te-rich region than the doubly charged vacancy on the Te sublattice under Pb-rich conditions (0.85 eV/defect) [21]. However,

attempts to fit this model led to unphysical end-members that did not describe the data as well. Therefore, we have decided to only include vacancies in this model. Although the enthalpies of formation at 300 K are similar for Te^{+2} and Va^{-2} on the Pb-sublattice and Te-sublattice, respectively, they are only comparable under opposing growth conditions. If the Te^{+2} antisite defects are calculated under the same equilibrium as Va_{Te}^{+2}, Pb-rich, than the enthalpy of formation rises dramatically from 0.90 eV/defect to 2.79 eV/defect. On the Te-rich side, the formation energy is 0.90 eV/defect, which is much higher than the Va_{Pb}^{-2} at 0.53 eV/defect and therefore plays a minor role. The comparison between the two defects is even greater in Bajaj's calculation where the difference is 0.35 and 0.87 eV/defect[22]. The differences in formation energy between the Va_{Pb}^{-2} and Te_{Pb}^{+2} defect in Te-rich conditions results in over an order of magnitude difference between the concentrations of the two defects at 1000 K[21]. This difference is within the experimental error of the measurements with which the parameters of the models are fit to and therefore cannot be used to reliably determine these values.

The five-sublattice model describes the experimental information quite well, but there are important assumptions made that could be improved. Mainly, recent work has shown that PbTe has a non-parabolic band structure [11] and at high temperatures could be a degenerate semiconductor[21]. This model assumes both parabolicity and non-degeneracy, which allows us to describe the density of states using Maxwell-Boltzmann statistics, thereby greatly simplifying the calculations. Other attempts to model PbTe have faced the same problem and have come to the conclusion that these assumptions are still reasonable[68]. Although these assumptions hold well for intrinsic PbTe these semiconducting materials are useful when doped with a third element, which will most certainly raise the carrier concentration and make the semiconductor degenerate.

Therefore, future work is needed to develop a semiconductor model that does not require these assumptions.

The 2SL model is shown in magenta in Figure 3.4-Figure 3.6. At low temperatures, the 2SL model describes the data quite well and closely resembles the 5SL model. At higher temperatures, particularly when the solid is in equilibrium with the liquid, it begins to deviate. This is not seen in the PbS system shown below. Attempts to reoptimize the liquid parameters with the carrier concentration did not improve the high temperature data, neither did introducing more interaction parameters. An interaction parameter that changes at the eutectic temperature would improve the description, but there is little physical justification for it. Calculations with the liquid phase suspended, shown as the dashed line, on the Te-rich side show better agreement with the experimental data at higher temperature. It is clear that the liquid phase plays a large role in determining the equilibrium carrier concentration. Despite the discrepancy in the experimental data at higher temperature, the interaction parameters agree well with the values determined from first-principle calculations at 300 K and agree well below the eutectic point. The description can be improved by introducing a $T * \ln(T)$ term in the interaction parameter on the Te-rich side. The updated 2SL and 5SL model are shown in Figure ?? as red and black lines, respectively. The agreement between the two models and experimental terms are much better; however, the CALPHAD determined formation energy changes from 44.5 kJ/mol to 40.8 kJ/mol compared to the DFT determined value of 51.1 kJ/mol. The $T * \ln(T)$ would indicate an excess contribution to the heat capacity and is rarely used in CALPHAD assessments, which might indicate that the better agreement might be a result of over fitting as opposed to representing a physical change.

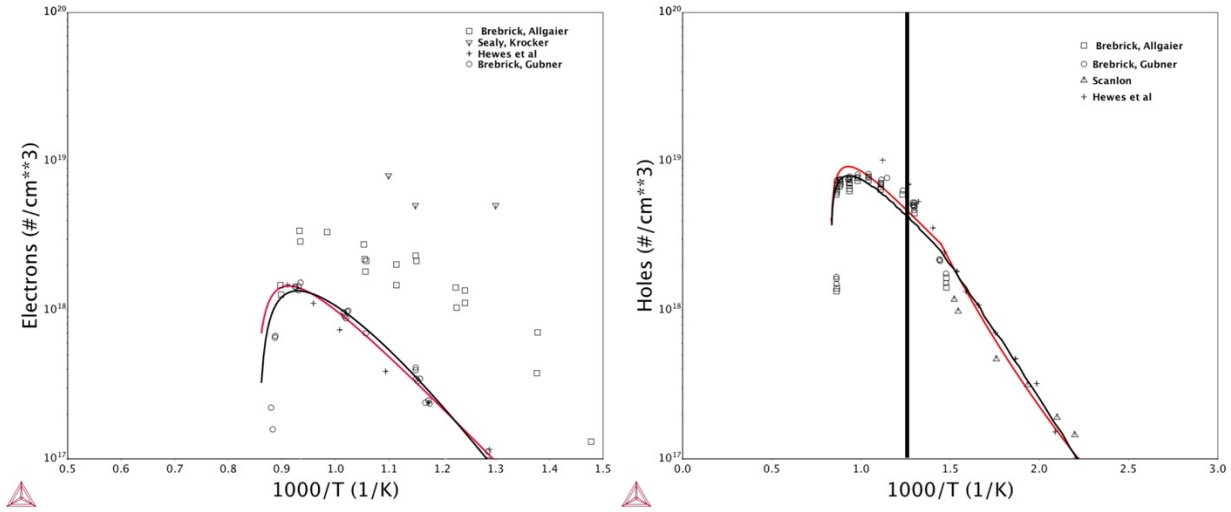

Figure 3.7: An updated 2SL model (red) and 5SL model (black) with experimental data. The updated 2SL model uses a $T * \ln(T)$ to better agree with the 5SL model; however, the formation energy of the defect converges farther from the DFT value.

3.4.2 PbS

The final optimized end-members for PbS are given in Table 3.2 as well. Similar to PbTe, the final end-members do not deviate far from the first-principle calculations. The carrier concentration of holes and electrons are given in Figure 3.8 and Figure 3.9, respectively. A satisfactory fit between the model and the experiment is shown. There are no previous CALPHAD assessments that do not treat PbS as a stoichiometric compound; therefore, no other fits are shown. Again, the carrier concentration data can be converted to solidus lines and the off-stoichiometric nature of PbS is given in Figure 3.10.

Similar to PbTe, a second model for PbS was also investigated. From the first-principle calculations, a single ionized vacancy on the S site had a slightly larger formation energy than the doubly ionized vacancy[21]. When optimizing with this model, the concentration of V_S^{+1} was sufficiently small enough that we removed it from the model without any loss of accuracy. In addition, PbS is also a non-parabolic semiconductor and will also become degenerate when doped

with a third element. Therefore, a new model will be necessary in the future to take these properties into account.

The 2SL model for PbS shows remarkable agreement with the experimental data and 5SL model. In the carrier concentration plots, the two are nearly indistinguishable and only deviate in the phase diagram at high temperatures where the concentration is linearly dependent on the carrier concentration. The formation energies based on the interaction parameters are also in qualitative agreement with the first-principle calculations in that the Pb vacancy is lower in energy than an S vacancy.

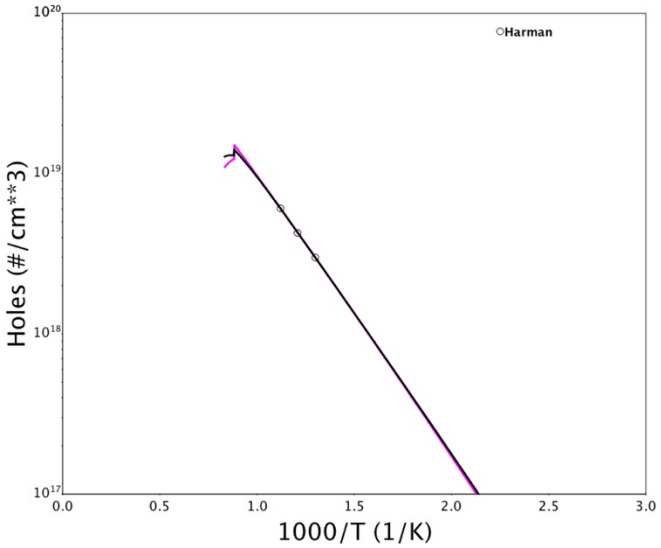

Figure 3.8: Carrier concentration of holes under S-rich conditions and experimental data points. The 5SL model is shown in black and the 2SL model is shown in magenta.

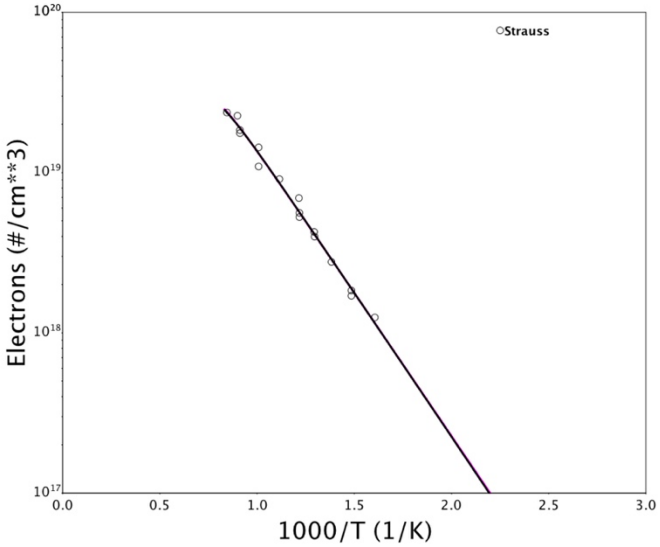

Figure 3.9: Carrier concentration of electrons under Pb-rich conditions and experimental data points. The 5SL model is shown in black and the 2SL model is shown in magenta.

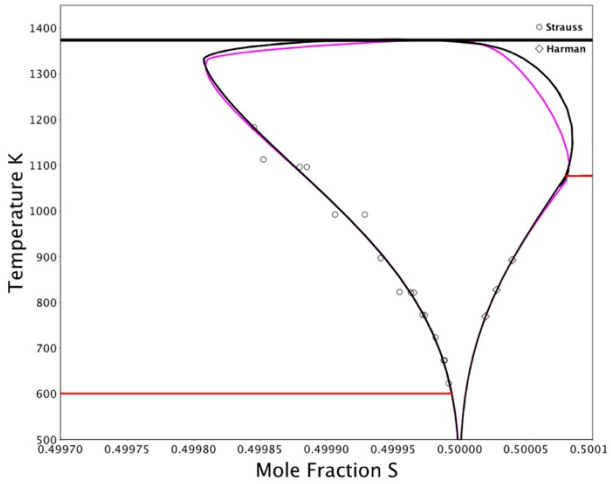

Figure 3.10: Enlarged region of Pb-S phase diagram to show solubility of PbS. The 5SL model is shown in black and the 2SL model is shown in magenta.

3.4.3 PbSe

The inaccuracies of the previously determined DFT calculations can be addressed through CALPHAD modeling. However, the assessment of this system would be extremely difficult if not for the insight provided by the first-principles calculations discussed before. The formation energies of the neutral vacancies are used as starting parameters for V_1 and V_3 and are allowed to

vary, along with a temperature dependent term to describe the experimental data. The final optimized parameters are given in Table 3.2 along with the associated first-principles calculation.

The optimized CALPHAD parameters agree qualitatively with the DFT calculations in that the formation energy of a Se vacancy is smaller than that of a Pb vacancy. In addition, the errors of the final parameters do not vary by more than 15% from the DFT predicted values. The carrier concentrations under Se-rich and Pb-rich conditions are shown in Figure 3.11 and Figure 3.12, respectively. The CALPHAD method matches experiment and DFT by describing hole and electron generation in the Se-rich and Pb-rich regime, respectively. The CALPHAD model also does an excellent job of describing the carrier concentration through the entire temperature range and shows great improvement from the DFT calculations alone evident from the previous chapter.

The phase diagram of PbSe is plotted in Figure 3.13 along with the converted experimental data points. The CALPHAD model does an excellent job of describing this data, particularly at lower temperatures. The model begins to deviate slightly at higher temperatures, which is due to the exponential growth of carriers and the linear relationship it has with solubility. No CEF model with solubility has been assessed; as such we are unable to compare it to past work. As mentioned previously, the assessment seen in Lin[75] differs by a factor of two due to an inconsistency when converting the carrier concentration to solidus data. An assessment has also been done where the solubility limits were used as experimental data in lieu of carrier concentration. This led to a better description of the high temperature phase diagram; however, the carrier concentrations at low temperatures are poorly described. In addition, the optimized end-member converged farther from the starting DFT values when fitting to the solubility limits. For these reasons, coupled with the fact that the carrier concentration is the important data for semiconductors, this procedure is not recommended here.

The 2SL model is shown as magenta in Figure 3.11, Figure 3.12 and Figure 3.13, and the 2SL model shows an agreement with experiment very similar to that of the 5SL model. The only large deviations occur at higher temperatures in the phase diagram where the discrepancy in carrier concentration is magnified. This is because the solubility limit is linearly proportional to the carrier concentration. Therefore, small deviations at high temperature where the carrier concentration is large will be much larger in the phase diagram. The final optimized parameters are given in Table 3.3 along with the formation energies determined by the CALPHAD method and DFT. The CALPHAD values agree qualitatively with the first-principles calculations in that the formation of a Pb vacancy is smaller in magnitude than a Se vacancy. They are also in close quantitative agreement, differing by no more than 16% in magnitude. This 2SL model is also fully compatible with other binaries, as the end-members have not been fit to the experimental data. Although the 2SL model is much simpler and does not contain many of the physical parameters that are found in the 5SL model its close agreement between the 5SL model, experimental data, and first-principles calculations indicate that it is physically sound.

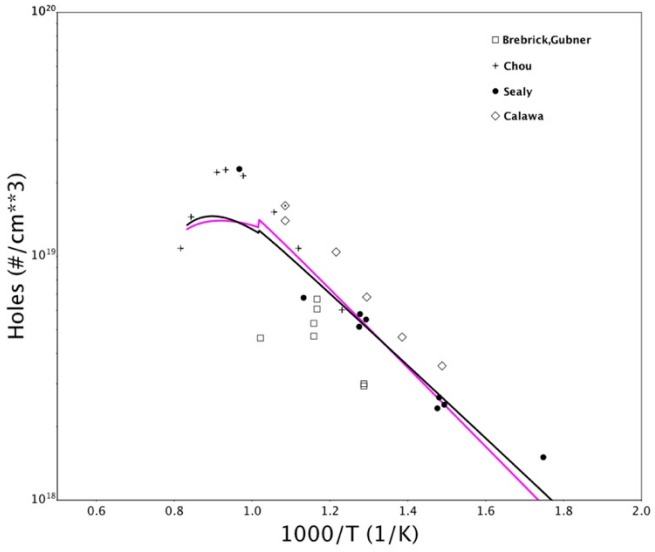

Figure 3.11: Carrier concentration of holes under Se-rich conditions and experimental data points. The 5SL model is shown in black and the 2SL model is shown in magenta.

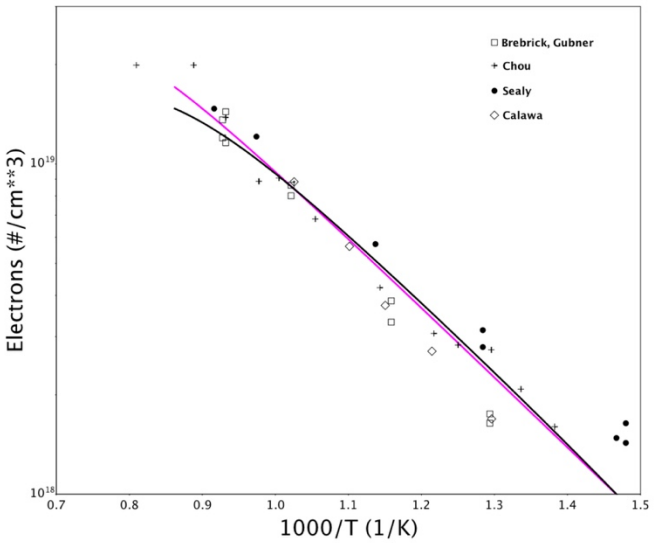

Figure 3.12: Carrier concentration of electrons under Pb-rich conditions and experimental data points. The 5SL model is shown in black and the 2SL model is shown in magenta.

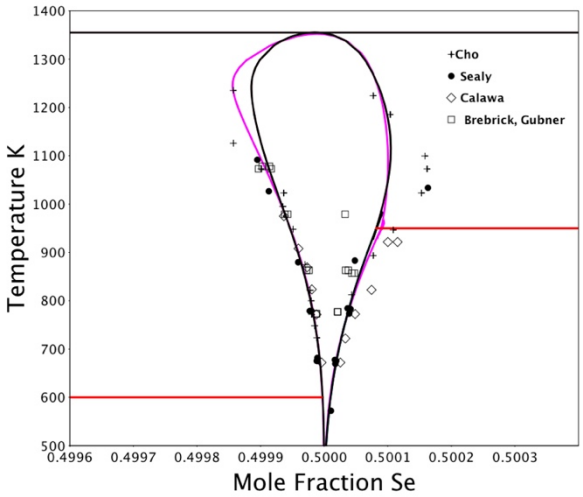

Figure 3.13: Enlarged phase region of PbSe where the carrier concentration has been converted to solubility points assuming doubly ionized vacancies. The 2SL model is shown in magenta and closely follows the 5SL model shown in black.

3.5 Experimental error in CALPHAD assessments

Quantifying uncertainty in CALPHAD assessments and phase diagrams is an important step but is often overlooked[93, 94]. The 2SL model allows us to determine how uncertainty in the experiment affects the end phase diagram as well as the physically relevant properties the model calculates; specifically, the formation energy of a defect. The PbSe phase diagram is well

established and does not require a temperature dependent interaction parameter to model, therefore it lends itself well for this investigation. The low temperature data from Sealy[52] and Calawa[51] were used to determine an average carrier concentration and standard deviation at a given temperature. The temperature, average log of the carrier concentration (#/cm^3), and standard deviation were 676 K, 18.1, and 0.21 for Pb-rich PbSe, respectively, and 674 K, 18.4, and 0.080 for Se-rich PbSe, respectively. A new assessment was conducted where the log of the carrier concentration plus or minus one standard deviation was used performed and is shown in Figure 3.14. The original 2SL assessment is shown in magenta and the assessment shown at plus one and minus one standard deviation are shown in dark blue and cyan, respectively. The uncertainty is largest on the Pb-rich side, which is reflected in a much wider range of carriers and compositions. Most of the experimental data is described within one standard deviation of the chosen experimental point. The effect of the uncertainty on the formation energy is shown in Table 3.4. Although the spread in formation energies still do not overlap with the DFT predicted values, the uncertainty in DFT calculations using GGA has been estimated to be as high as 28,000 J/mol[21], which when taken into account agrees with the CALPHAD determined values.

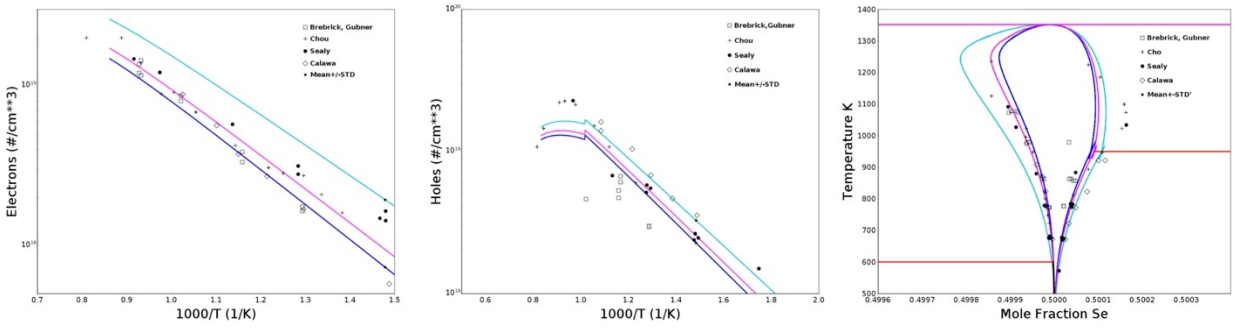

Figure 3.14: Reassessment of the PbSe binary taking into account experimental uncertainty. The original 2SL assessment is shown in magenta and assessments taken at one standard deviation above and blow are shown in cyan and dark blue, respectively.

Table 3.4: CALPHAD determined formation energies when experimental uncertainty is considered.

Defect	Equilibrium	CALPHAD Determined Formation Energy at 300 K (J/mol)	DFT Predicted Formation Energy at 300 K (J/mol) [21]
Va_{Se}	Pb-Rich	50,000 ± 2,700	57,000
Va_{Pb}	Se-Rich	41,100 ± 1,000	31,000

3.6 Conclusion

This study has developed new model descriptions for the binary PbTe, PbS, and PbSe semiconductors. The model is different from previous ones used as it explicitly has sublattices dedicated to electrons and holes. An excellent fit to the carrier and phase boundaries has been found for both systems. The PbTe free energies show a marked improvement from previous models and the PbS and PbSe are new and consistent with the experimental and first-principles data. The carrier concentration has been converted into solubility data and new phase diagrams have been developed. First-principles calculations were used to provide starting values for the assessment to make the models more physically accurate. The 5SL model could be improved by explicitly incorporating the band structure of the semiconductors, but the parabolic band assumption has been proved to be sufficient to describe the data. In addition, a 2SL model compatible in multicomponent databases has also been determined. Using a fixed value of 2.3RT for vacancy containing end-members, the model can then be fit to the experimental data. In addition, the interaction parameter can be linked to the formation energy for further physical significance. The 2SL model shows good agreement with the experimental data, particularly in the PbS and PbSe systems and qualitatively agrees with the first-principle calculations. These models can be used to optimize the properties of TE devices where phase equilibrium plays a key role in increasing their *zT* values.

4. CALPHAD Modeling of the Pseudobinaries and the Pseudoternary of the PbX (X=S,Se,Te) System with Na doping

4.1 Introduction

The thermodynamics of the constituent binaries of the PbX (X=S,Se,Te) system have been established as outlined in Chapter 3. There are limited ways of increasing the *zT* of the thermoelectrics within the binary systems alone. The intrinsic carriers of the system are too low to enhance the power factor and the number and types of defects that can be introduced to scatter phonons are ineffective. Fortunately, by alloying or doping with additional elements, the individual properties that go into determining the *zT* can be enhanced. The additional degrees of freedom allow for greater control but introduce greater complexity for determining the phase diagram. However, the flexibility of the CALPHAD method and CEF model are perfect for describing multicomponent systems and therefore lends itself well for this application.

Recent effort has identified possible methods for isolating and optimizing the properties in the PbX system [95] [96] [97] [98]. For example, alloying PbTe with PbS introduces precipitates that are able to scatter heat carrying phonons, thereby reducing the thermal conductivity without adversely affecting the electrical properties [99] [100]. Likewise, alloying PbTe with PbSe creates a solid solution that introduces point defects that scatter short wavelength phonons [101]. In addition, PbSe also increases the convergence temperature of the L and Σ bands in PbTe, allowing for increased degeneracy and high Seebeck and electrical conductivity [82]. The pseudoternary has also been investigated with promising results, as the alloying of Se increases the solubility of S in PbTe, which further lowers the thermal conductivity and has higher *zT* than any of the constituent pseudobinaries or binary systems [102] [103] [104] [105]. Another method for optimizing thermoelectrics involves tuning of the carrier concentration to optimize the power

factor, $S^2\sigma$, of the material [11]. The carrier concentration can be controlled via the composition, growth condition, and annealing temperature [106]. The solubility, creation of second phase structures, and carrier concentration can all be determined by the thermodynamics of the system. Therefore, a complete description of the thermodynamics should be a first step to optimizing these materials.

In order to be practically useful, these semiconductors need to be doped to produce sufficient carriers. One of the most effective doping elements in these systems is Na. It has been used to effectively increase the power factor as well as reduce the thermal conductivity in the binary systems[82, 107] as well as the PbTe-PbS[99], PbTe-PbSe[13], and PbTe-PbSe-PbS systems[103-105]. Each Na atom soluble in the matrix contributes one hole to the valence band for concentrations above approximately 6 x 10^{19} holes/cm^{-3}[108], therefore, if the solubility of Na is known then precise tuning of the carrier concentration can be determined via the phase diagram. In addition, point defects within the matrix caused by the Na atoms contribute to a lower thermal conductivity and when Na is doped beyond its solubility, nanoprecipitates form which further lower the thermal conductivity[107]. Lastly, it has been determined that the electronic structure is not greatly altered by Na defects in lead chalcogenides, which facilitates modeling of the transport properties[109].

The phase relationship in the Pb(S,Se,Te) system and its constituents have been studied a number of times and there is a wealth of both experimental and first-principles data in the literature. Similar studies of this system have been performed by Volykhov et al [110] and Liu [111]. This study will differ in some key areas. Most importantly, the semiconductors are treated as stoichiometric phases in the previous thermodynamic assessments. Experimental and first-principles calculations indicate that vacancies play a key role in the carriers of the system, which

lead to small stoichiometric deviations [22] [112]. In addition, Volykhov uses a four-parameter Margules series to model the excess energy terms, fails to model the PbSe-PbTe miscibility gap, and does not extend their modeling into the pseudoternary region. Liu's study uses a subregular model of mixing outlined by Ganguly and Saxena [113], which limits its applicability as this model is not compatible with the more established CEF framework. In addition, limited experimental data on the PbS-PbSe system required fitting the binary interaction parameters from the ternary system. This assessment uses non-stoichiometric models [112] for the PbX binaries when modeling the pseudobinaries and pseudoternary as well as using the most up to date experimental and first-principles data for a completely self-consistent description that can also model the intrinsic carriers of the system.

There is limited information on the solubility of Na in the PbX systems. Yamini et al determined the solubility limit of Na in PbTe at three different temperatures along the NaTe line[114] and He et al determined the room temperature solubility of Na in each system[107]. In order to gain greater insight into the role of Na in these systems, first-principles calculations will be performed using the dilute-limit approximation to determine the formation energy of Na defects in a given equilibrium condition. This method has been used in the past to calculate and plot phase diagrams for the Pb-X-Na ternary systems[21, 34]. The study done by Bajaj et al outlined the importance of only including defects that contain only the expected charge state based on valence counting when performing defect analysis[34], which explains the anomalous negative defect formation energies found in the Pb-S-Na system studied by Doak et al[21]. Defect formation energies have been determined following this advice, which have been used to build a physically sound CALPHAD model that can describe the Na doped PbX system. The CALPHAD model is also able to extrapolate from the Na-doped PbX systems into the pseudoternaries and

pseudoquaternary systems, which are computationally prohibitive to access via first-principles calculations.

4.2 Literature Review

4.2.1 PbS-PbTe System

The PbS-PbTe system was first investigated by Darrow through differential thermal analysis (DTA) [115]. The study established the presence of an asymmetric miscibility gap below 1078 K. The miscibility gap boundaries were determined by the changes in lattice parameter. Similar studies involving x-ray diffraction (XRD) measurements of the lattice parameter were done by Demin [116] and Leute [117], which agree fairly well with the previous study in the solid region. The liquidus temperatures differ between the study of Demin and Darrow by as much as 20 degrees in the PbTe rich regime. For this study, the authors give more weight to Demin's study as their melting point for PbTe has a better agreement with the previously established value of 1196 K [76] and has more detailed experimental explanations given in their report.

4.2.2 PbSe-PbTe

Initial studies of this system were performed by Elagina [118] and focused on the high temperature liquidus phase relation. In their paper, a minimum liquidus temperature was determined between PbSe and PbTe, Later studies done by Grimes [119] and Steininger [120] indicate a monotonically decreasing liquidus from PbSe to PbTe. All studies indicated a complete solid solution between PbSe and PbTe. Conversely, Liu's study investigated the low temperature region and found that an asymmetrical miscibility gap existed [111]. A recent experimental study by Kim et al [121] confirmed the presence of nanostructures below a temperature of approximately 623 K. The miscibility gap is also predicted in the first-principles calculations done by Usanmaz using a combination of high-throughput *ab initio* calculations and cluster expansion techniques to

model the binodal region [122]. Usanmaz's miscibility gap underestimates the critical point by approximately 100 K. Doak et al also investigated the PbSe-PbTe system using special quasi-random structures (SQS), which also predicted a miscibility gap in this region [123]. It is important to note that Volykhov's assessment does not model this phase separation.

4.2.3 PbS-PbSe

The data for PbS and PbSe are quite scattered and at odds with data from the binaries. The liquidus and solidus data points in Gromakov [124] and Strauss [125] are much higher than the data from Kuznetsova [126]. This is likely due to their use of DTA in determining the liquidus points, which is not as accurate as the annealing and quenching done by Kuznetsova. In addition, Strauss states in his paper that their samples were likely not at equilibrium due to inconsistencies within the liquid and solid compositions but do indicate a very slim liquid and solid region. For this reason, the present authors agree with the analysis of Volykhov, which favors the work of Kuznetsova. Quenching in these systems is extremely difficult due to their inherently low thermal conductivity and the discrepancy between the melting points in the binaries, and these studies indicate that further investigation is probably warranted. All studies confirm a continuous solid solution between PbS and PbSe. The study by Liu chose to use the pseudoternary region to determine the binary interaction parameters, from which a miscibility gap at 373 K was determined. This result has not been confirmed experimentally. Instead of fitting from the ternary system, we choose to use the first-principles data calculated by Usanmaz, which calculated a critical temperature slightly below 200 K with an asymmetrical miscibility gap. Doak's study using SQS also determined a miscibility gap at 275 K as well.

4.2.3 PbS-PbSe-PbTe

The pseudoternary was investigated by Liu at four separate temperatures 573, 773 K, 973, and 1073 K [111]. The high temperature measurements of 773 K and above were annealed from 1 to 60 days and quenched, while the low temperature measurement was performed via chloride flux for 150 days. Samples were then analyzed using X-ray power diffraction to determine if phase separation had occurred. There are also recent studies which investigated the thermoelectric properties of this pseudoternary system [103] [127] [105] [104], although only Yamini's [102] study explicitly measured the maximum solubility of PbS and PbSe in PbTe to be $(PbTe)_{0.8}(PbS)_{0.1}(PbSe)_{0.1}$ at 773 K. The study by Korkosz et al had complete solid solubility up to $(PbTe)_{0.76}(PbS)_{0.12}(PbSe)_{0.12}$ although their samples were not annealed and quenched from a higher temperature and thus do not represent thermal equilibrium [105].

4.2.3 Na-Pb-X

There are limited experimental studies on the solubility of Na in the PbX compounds. Crocker investigated Na defects in PbTe by measuring the carrier concentration in annealed samples of Na doped PbTe [108]. Crocker determined a maximum solubility of $Na_{.017}Pb_{.983}Te$ by plotting carrier concentration vs Na concentration. Yamini questioned these results as Crocker assumed a constant Hall factor of 1, which has been shown to vary with doping concentration[114]. In Yamini's study, Wavelength Dispersive Spectroscopy (WDS) in an Electron Probe Micro-Analyser (EPMA) was used to determine the Na content in annealed $Na_yPb_{(1-y)}Te$ at 513 K, 623 K, and 780 K and determined a solubility of 0.24 at%, 0.70 at%, and 0.65 at% Na, respectively. He et al investigated the microstructure of 2% Na doped PbX compounds [107]. By determining the average precipitate size and number density from Transmission Electron Microscopy (TEM) studies, He was able to estimate the solubility of $Na_yPb_{1-y}X$ as 0.005, 0.009, and 0.02 for PbTe, PbSe, and PbS, respectively. Samples were only doped up to 2 at% Na and were allowed to air

cool from 1423 K, so it is difficult to determine to what equilibrium temperature this solubility is assigned.

4.3 Computational Modeling

4.3.1 CALPHAD Modeling

The pseudoternary system only consists of two phases, the liquid and the PbX phase, which exhibits NaCl crystal structure. The binaries have already been assessed and we have taken the parameters from the associate liquid model and two-sublattice model for PbX from the binary systems [22] [57] [112] [58].

4.2.1.1 Associate Liquid Model

According to the CEF framework, the Gibbs free energy of an associate solution model is calculated as

$$G_m^{liquid} = \sum_{i=1}^{n} y_i \, {}^0G_i \; - RT \sum_{i=1}^{n} y_i \ln(y_i) + \sum_{i=1}^{n-1} \sum_{j=i+1}^{n} y_i y_j L_{ij} \quad (4.1)$$

$$L_{ij} = \sum_{v=0}^{k} (y_i - y_j)^v \, {}^vL_{ij} \quad (4.2)$$

where y_i is the site fraction of associate *i* (*i*=Pb, S, Se, Te, PbS, PbSe, PbTe), R is the gas constant, ${}^0G_i$ is the Gibbs free energy of associate *i*, T is temperature, and L_{ij} is the interaction parameter between associates *i* and *j*. Although the associate liquid model does not accurately capture the configurational entropy in higher ordered systems[128], a 1:1 stoichiometric ratio reduces to the ionic liquid and is sufficient in this example. Due to the lack of information on the ternary liquidus, no ternary interaction parameters were introduced. The binary interaction parameters, L_{ij} between PbTe, PbS, and PbSe were optimized to fit to the experimental data.

4.2.1.2 2SL Model for PbX

The 2SL model is best-suited for multicomponent database development as it retains description of the intrinsic carriers of the binary system and contains compatible end-members [112]. The phase equilibrium data collected for the pseudobinaries and pseudoternary did not investigate carrier concentration, so we must assume that these were collected at the stoichiometric composition. The PbX phase can then be modeled as (Pb,Na,Va)(S,Se,Te,Va)

$$G_m^{PbX} = \sum_i \sum_j y_i' y_j'' \ {}^0G_{i:j} + RT\left(\sum_i y_i' \ln\left(y_i'\right) + \sum_j y_j'' \ln\left(y_j''\right)\right) + {}^{bin,E}G_m + {}^{tern,E}G_m \quad (4.3)$$

where y_i' is the site fraction of component *i* on the first sublattice, y_j'' is the site fraction of component *j* on the second sublattice, ${}^0G_{i:j}$ is the end-member taken from the binaries and ${}^EG_m$ the excess Gibbs free energy. Similar to the associate liquid model, the binary excess Gibbs free energy is modeled using the Redlich-Kister polynomials where the components on the second sublattice are allowed to mix

$${}^{bin,E}G_m = \sum_{i=1}^{n-1} \sum_{j=i+1}^{n} y_i'' y_j'' L_{Pb:i,j} \quad (4.4)$$

$$L_{Pb:i,j} = \sum_{v=0}^{k} \left(y_i' - y_j''\right)^v \ {}^vL_{Pb:ij} \quad (4.5)$$

The interaction parameters ${}^vL_{Pb:ij}$ are fit to the experimental data in the binary systems. Likewise, the ternary excess model is described as

$${}^{tern,E}G_m = \sum_{i=1}^{n-2} \sum_{j=i+1}^{n-1} \sum_{k=j+1}^{n} y_i'' y_j'' y_k'' \ L_{Pb:ijk} \quad (4.6)$$

$$L_{Pb:ijk} = v_i \ {}^iL_{Pb:ijk} + v_j \ {}^jL_{Pb:ijk} + v_k \ {}^kL_{Pb:ijk} \quad (4.7)$$

$$v_i = y_i'' + (1 - y_i'' - y_j'' - y_k'')/3 \quad (4.8)$$

$$v_j = y_j'' + (1 - y_i'' - y_j'' - y_k'')/3 \quad (4.9)$$

$$v_k = y_k'' + (1 - y_i'' - y_j'' - y_k'')/3 \quad (4.10)$$

where the ternary interaction parameters ${}^{i}L_{Pb:ijk}$ are fit to describe the experimental data. The Gibbs free energy functions of the pure elements in their standard elemental reference (SER) state and liquid phase are taken from Dinsdale [86].

The 2SL model can also be used in order to determine the formation energy of defects in dilute concentrations as has been done previously in the binary systems[112]. Na substitutes for Pb on the Pb sublattice so the 2SL model can be described as (Pb,Na,Va)(X,Va) in the ternary system. When heavily doped with Na, the concentration of Na defects is orders of magnitude higher than the intrinsic defects at lower temperatures and therefore the model can be assumed to be equivalent to (Pb,Na)X. A similar derivation to the one in Chapter 3 is done here for Na defects. In order to determine the equilibrium site fraction of Na on the Pb sublattice, the grand potential must be minimized

$$\mathcal{G}_m = G_m - \mu_{Pb} y_{Pb} - \mu_{Na} y_{Na} \quad (4.11)$$

where $\mathcal{G}_m$, μ_{Pb}, and μ_{Na} are the grand potential per mole and chemical potential of Pb and Na atoms, respectively. The molar Gibbs free energy, G_m, is calculated according to CEF as

$$G_m = y_{Na}\ {}^{\circ}G_{NaX} + y_{Pb}\ {}^{\circ}G_{PbX} + RT\big(y_{Na}\ln(y_{Na}) + y_{Pb}\ln(y_{Pb})\big) + y_{Na}y_{Pb}L_{Na,Pb:X} \quad (4.12)$$

Taking the derivative of equation 4.11 with respect to y_{Na} leads to

$$0 = \frac{dG_m}{dy_{Na}} - \mu_{Na} + \mu_{Pb} \quad (4.13)$$

Substituting the derivative of equation 4.12 with respect to y_{Na} into equation 4.13 leads to

$$- {}^{\circ}G_{NaX} + {}^{\circ}G_{PbX} + L_{Na,Pb:X}(1 - 2y_{Pb}) + \mu_{Na} - \mu_{Pb} = \mathrm{RTln}\left(\frac{y_{Na}}{1-y_{Na}}\right) \quad (4.14)$$

Under the dilute limit where y_{Na}<< 1 the equilibrium site fraction of Na can be calculated as

$$y_{Na_{Pb}}^{eq} = \exp\left(-\frac{{}^{\circ}G_{NaX} - {}^{\circ}G_{PbX} + L_{Na,Pb:X} - \mu_{Na} + \mu_{Pb}}{\mathrm{RT}}\right) \quad (4.15)$$

Where the numerator can be linked to the formation energy of a Na defect on the Pb sublattice. The term ${}^{\circ}G_{NaX}$ is the Gibbs free energy of a compound with every Pb atom replaced with a Na atom and can be fixed to first-principles calculations. The end-member ${}^{\circ}G_{PbX}$ is determined from the binary assessment and the chemical potentials of Na and Pb are fixed in a three phase equilibria. This leaves the interaction parameter $L_{Na,Pb:X}$ free to be optimized to experimental data or first-principles calculations. The fact that this interaction parameter is system specific allows it to be compatible in multicomponent databases as well. The interaction parameter will be fit to the experimental data in the Pb-Te-Na system and first-principles calculations in the Pb-S-Na and Pb-Se-Na systems.

4.3.2 First-Principles Modeling

An analogous approach to that found in Chapter 2 is used here with the addition of Na^{-1} defects on the Pb site and only the doubly ionized vacancies on either sublattice considered. The total energies of the supercells were determined by DFT[35] calculations performed with the

Vienna Ab-initio Simulation Package[37] (VASP) [38] with projector-augmented wave[39] potentials utilizing the generalized gradient approximation (GGA) exchange-correlation functional of Perdew, Burke, and Ernzerhof[40]. The calculations treat the $6s^2 6p^2$, $3s^2 3p^4$, $4s^2 4p^4$, $5s^2 5p^4$, and $3s^1$ as valence electrons for the Pb, S, Se, Te, and Na atoms respectively. The NaCl crystal structure for the PbX crystal structure was taken from the Inorganic Crystal Structure Database[41] (ICSD). Supercells were constructed using a 3 x 3 x 3 array of the unit cell for 216 total atoms. Structures were allowed to relax with a maximum cutoff energy of 350 eV and a Monkhorst-Pack 4 x 4 x 4 k-point meshes [42]. Lattice parameters and atomic positions were allowed to relax until energy convergence reached 0.1 meV and a final static calculation was performed.

4.4 Results and Discussion

The optimization of the CALPHAD parameters was done in the PARROT [89] module of ThermoCalc [90]. The interaction parameters for the binary and ternary system are listed in Table 4.1.

Table 4.1 Thermodynamic parameters for the liquid and PbX phase. All units J/mol.

Phase	Model	Parameter
Liquid	$(Pb,S,Se,Te,PbS,PbSe,PbS)_1$	${}^0L^{liq}_{PbS,PbTe} = -7{,}0395$
		${}^1L^{liq}_{PbS,PbTe} = -12{,}686$
		${}^0L^{liq}_{PbS,PbSe} = -17{,}214 + 13.5T$
		${}^0L^{liq}_{PbSe,PbTe} = 9{,}099$
PbX	$(Pb,Na,Va)_1(S,Se,Te,Va)_1$	${}^0L^{PbX}_{Pb:S,Te} = 38{,}224 - 20.9T$
		${}^1L^{PbX}_{Pb:S,Te} = 4{,}372$
		${}^0L^{PbX}_{Pb:S,Se} = 3{,}206$
		${}^1L^{PbX}_{Pb:S,Se} = 590$
		${}^0L^{PbX}_{Pb:Se,Te} = 10{,}251$
		${}^1L^{PbX}_{Pb:Se,Te} = 1{,}349$
		${}^0L^{PbX}_{Pb:S,Se,Te} = -4{,}525$
		${}^1L^{PbX}_{Pb:S,Se,Te} = 30{,}770$

		${}^{2}L^{PbX}_{Pb:S,Se,Te} = -23{,}661$
		${}^{\circ}G_{Na:S} = -61{,}729 + {}^{0}G^{Bcc}_{Na} + {}^{0}G^{Ort}_{S}$
		${}^{0}L^{PbX}_{Na,Pb:S} = -131{,}927$
		${}^{\circ}G_{Na:Se} = -82{,}803 + {}^{0}G^{Bcc}_{Na} + {}^{0}G^{Hex}_{Se}$
		${}^{0}L^{PbX}_{Na,Pb:Se} = -78{,}416$
		${}^{\circ}G_{Na:Te} = -74{,}873\ {}^{0}G^{Bcc}_{Na} + {}^{0}G^{Hex}_{Te}$
		${}^{0}L^{PbX}_{Na,Pb:Te} = -82{,}091 + 31T$

4.4.1 PbS-PbTe

The PbS-PbTe phase diagram is shown in Figure 4.1. The asymmetric nature of the miscibility gap required a sub-regular solution parameter in the Pb(S,Te) system. The miscibility gap describes the experimental data quite well. The spinodal region also agrees very well with several studies investigating the spinodal effects on the Pb(S,Te) system. He et al confirmed that the composition of $PbTe_{0.7}S_{0.3}$ annealed at 773 K exhibits spinodal decomposition [100]. According to our model, any material at this composition annealed at 810 K or lower should spinodally decompose. This is also confirmed in Girard's study, which annealed two compositions, $PbTe_{0.7}S_{0.3}$ and $PbTe_{0.92}S_{0.08}$, at 773 K and found spinodal decomposition and nucleation and growth, respectively [99]. Androulakis's study found spinodal decomposition at compositions higher than $PbTe_{0.84}S_{0.16}$ annealed at 773 K, which is outside of the spinodal region in our model [129]. The 2.5 at% Sn that was added to aid with the processing could explain this, or more likely, the sample decomposed after annealing at a lower temperature once it entered the spinodal regime. The spontaneous nature at which spinodal decomposition occurs makes retaining high temperature equilibrium states extremely difficult. It is important to note that the spinodal line depicted here is only the chemical spinodal. A study performed by Doak et al [123], which explored the coherency spinodal, is likely suppressed due to the lattice mismatch in this compound such that the spinodal

decomposition microstructure depicted in these studies may not actually be spinodal but instead caused by discontinuous precipitation as seen in the (Pb,Sn,Ge)-Te system [130]. This will be discussed in greater detail later in Chapter 7. The liquidus data is well explained by two parameters between the PbS and PbTe associates.

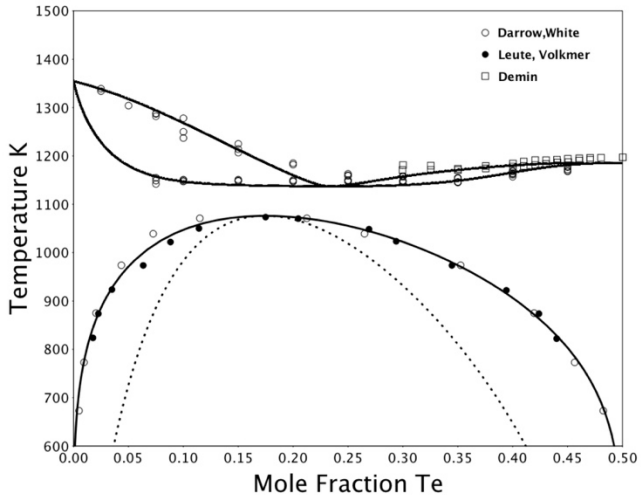

Figure 4.1 PbS-PbTe phase diagram. Experimental data taken from Darrow[115], Leute [117], and Demin [116].

4.4.2 PbSe-PbTe

The PbSe-PbTe phase diagram is shown in Figure 4.2. The tie-line determined by Liu [111] was used to establish the miscibility gap below 650 K. The asymmetry of the miscibility gap is also predicted by first-principle calculations by Usanmaz [122] and confirmed in Kim's study [121] where nanostructures dissolved above 623 K. The established spinodal region can also be used to guide material design similar to the PbS-PbTe studies. The larger degree of mutual solubility of PbTe and PbSe also provides greater flexibility in introducing point defects as discussed earlier. Similar to the PbS-PbSe system, the PbSe-PbTe liquidus data is scattered; however, a reasonable fit to the experimental data is seen. Volykhov [110] used the solid

interaction parameters to fit to the experimental liquidus data, which failed to produce a miscibility gap at lower temperatures and created a minimum in their liquidus curve, which is at odds with previous studies as discussed before. This assessment used the interaction between the PbSe and PbTe liquid associates to fit the data, which results in a monotonically decreasing liquidus as is shown in the data and therefore is likely more physically accurate.

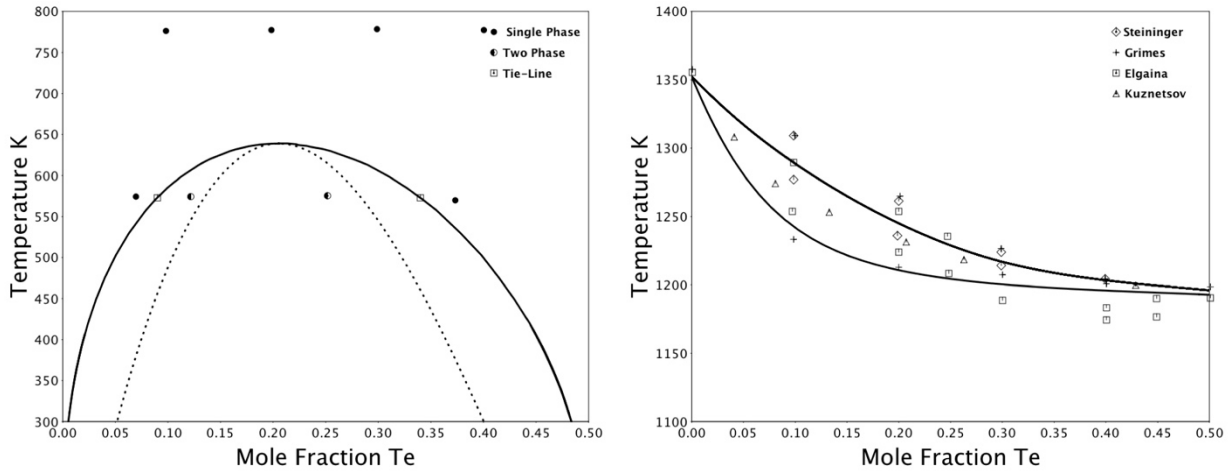

Figure 4.2: PbSe-PbTe phase diagram solid phase equilibria (left) and solid-liquid equilibria (right). The two phase data is taken from Liu and the liquidus is taken from Steininger [120], Grimes [119], Elagina [118], and Kuznetsova [126].

4.4.3 PbS-PbSe

The liquidus of the PbS-PbSe phase diagram is shown in

Figure 4.3. The interaction parameters predicted by Usanmaz [122] create a miscibility gap below 300 K, which is beyond the applicability of the Gibbs free energy functions established in the CALHAD framework established by SGTE and therefore not shown here[86]. A solid solution of Pb(S,Se) exists until the liquidus, which exhibits a minimum at 1333 K. Similar to PbSe-PbTe, the solid interaction parameters are left fixed and only the parameters of the PbS and PbSe liquid associates are allowed to vary to describe the data. An extremely thin solid and liquid region is also shown with reasonable agreement from the data of Kuznetsova. Agreements largely differ

due to the disagreement in melting temperature for PbS, which varies in the literature by as much as 90 K.

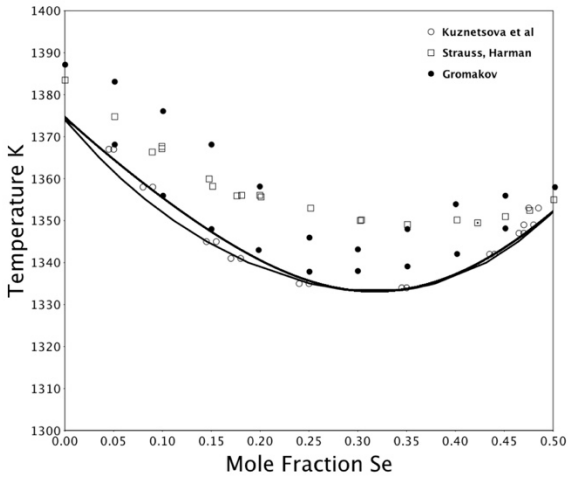

Figure 4.3: PbS-PbSe liquidus phase diagram with experimental data from Kuznetsova [126], Strauss [125], and Gromakov [124]. The data is scattered due to various experimental techniques. The data from Kuznetsova was used in determining the liquid interaction parameters.

4.4.4 PbS-PbSe-PbTe

The pseudoternary phase diagram at various temperatures is shown in Figure 4.4. Liu's study [111] was used to determine the interaction parameters and a 2nd order ternary parameter was necessary to fully describe the data in the entire composition range. Nearly all experimental data points are correctly described as single or two phase. The presence of PbSe increases the mutual solubility of PbS in PbTe as noted by Yamini [102]. This model can be used to better understand the results reported by Korkosv [105], which reported a solid solution in $PbTe_{0.86}Se_{0.07}S_{0.07}$. First-principles calculations in that study indicate alloys annealed up to 900 K should still exhibit nanostructures. Although not specifically annealed at a certain temperature, the phase diagram at 773 K in Figure 4.4 indicates that these compositions are still in the single phase region. Meanwhile, the composition $PbTe_{0.76}Se_{0.12}S_{0.12}$, which did exhibit nanostructures, is within the two-phase region. Yamini investigated the Pb(S,Se,Te) system as well and determined the

solubility limit at 773 K to be $PbTe_{0.8}Se_{0.1}S_{0.1}$, which is in very close agreement with our model [102].

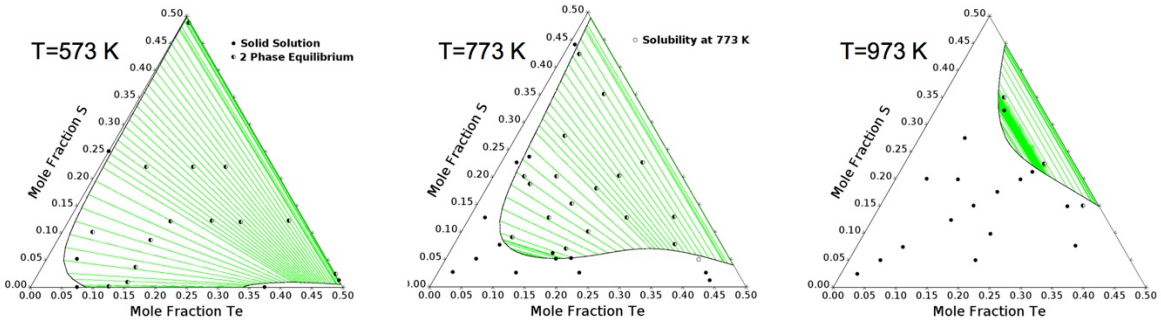

Figure 4.4: Pseudoternary phase diagrams of the Pb(S,Se,Te) system at given temperature. Single and two phase experimental data from Liu [111]. The solubility limit of $PbTe_{1-2x}Se_xS_x$ was determined to be $PbTe_{0.8}Se_{0.1}Se_{0.1}$ [102].

4.3.5 Na-Pb-X

The experimental solubility information from Yamini et al[114] was used to optimize the interaction parameter in the Na-Pb-Te system. The defect formation energy of Na on the Pb site under PbS-NaS-Na_2S and PbSe-NaSe-Na_2Se conditions was used to fit the interaction parameter for the Na-Pb-S and Na-Pb-Se systems, respectively. The final optimized parameters are listed in Table 4.1 and the Na solubility along the NaX tieline is shown in Figure 4.8 for each compound.

The defect formation energies determined by DFT and the CALPHAD model for the Na-Pb-S system are given in Table 4.2. By including only the expected charge states of the defects there are no negative formation energies for the Na defects as reported before[21]. The CALPHAD model is consistent with the first-principles calculations, which indicate that the PbS-NaS-Na_2S and PbS-NaS-NaS_2 equilibrium should have the lowest and similar formation energies. However, the formation energies diverge far from these Na-rich equilibria. In these Pb and S-rich conditions, the concentration of Na and Va defects are of the same order of magnitude, which violates one of the assumptions made when deriving equation 4.15 to calculate the formation energy of the Na

defect. This assumption is still valid in the Na-rich regions to which the interaction parameter is fit. Therefore, the constructed phase diagram should still be consistent but the calculated formation energies in the other regions less accurate. The ternary phase diagram at 780 K is shown in Figure 4.5(a) and the enlarged region in Figure 4.5(b). The region of greatest solubility of Na lies along the NaS tieline and the width increases for Na-poor conditions where the intrinsic vacancies play a larger role.

Table 4.2: Defect formation energies at 300 K calculated by DFT and CALPHAD model for the Na-Pb-S system. The CALPHAD interaction parameter was fixed in order to match the DFT value in the PbS-NaS-Na_2S equilibria.

Equilibria	DFT Determined Formation Energy at 300 K (kJ/mol)	CALPHAD Determined Formation Energy at 300 K (kJ/mol)
PbS-Pb-Na_2S	10.6	34.5
PbS-NaS-Na_2S	6.07	6.07
PbS-NaS-NaS_2	6.07	6.07
PbS-S-NaS_2	7.23	42.3

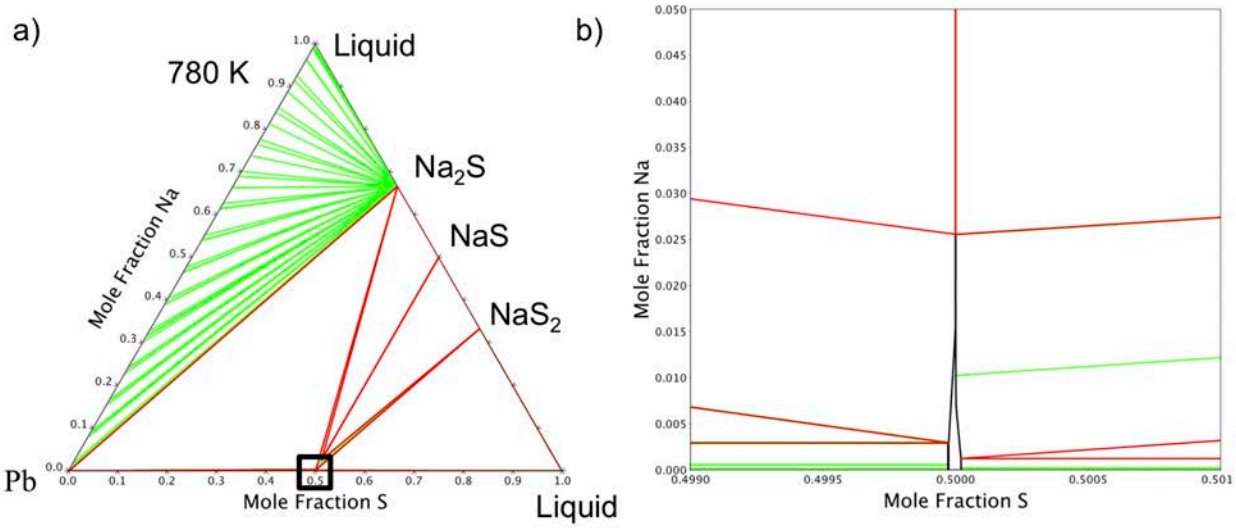

Figure 4.5: a) Na-Pb-S ternary at 780 K b) Enlarged region around PbS

The defect formation energies determined by DFT and the CALPHAD model for the Na-Pb-Se system are given in Table 4.3 and similar trends to those found in the Pb-Na-S system are

found here. The lowest formation energies are in the Na-rich regions of PbSe-NaSe-$NaSe_2$ and PbSe-NaSe-Na_2Se, which are also matching. The formation energies diverge farther away from these equilibria where the intrinsic carriers become more prominent. The ternary phase diagram at 780 K is shown in Figure 4.6(a) and the enlarged region in Figure 4.6(b). PbSe shows a greater width than PbS and the point of highest Na solubility lies along the NaSe line as well as slightly Se-rich.

Table 4.3: Defect formation energies at 300 K calculated by DFT and CALPAHD model for the Na-Pb-Se system. The CALPHAD interaction parameter was fixed in order to match the DFT value in the PbS-NaSe-Na_2Se equilibria.

Equilibria	DFT Determined Formation Energy at 300 K (kJ/mol)	CALPHAD Determined Formation Energy at 300 K (kJ/mol)
PbSe-Pb-Na_2Se	22.2	51.3
PbSe-NaSe-Na_2Se	10.3	10.3
PbSe-NaSe-$NaSe_2$	10.3	10.3
PbSe-Se-$NaSe_2$	11.5	16.5

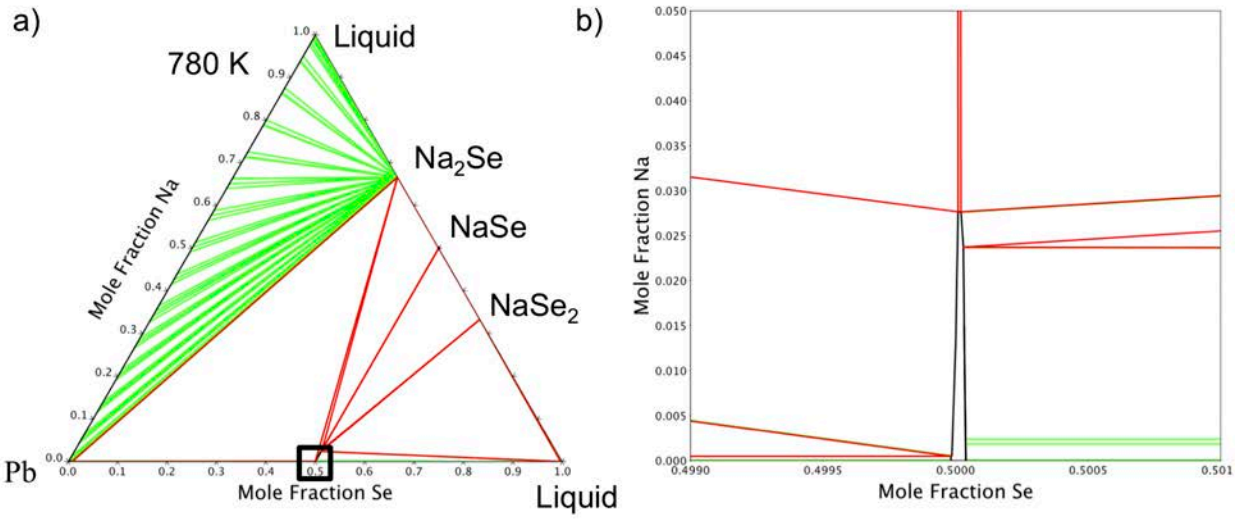

Figure 4.6: a) Na-Pb-Se ternary at 780 K b) Enlarged region around PbSe

The solubility data of Na in PbTe is well described as depicted in Figure 4.7 and within the experimental error for all data points. The maximum solubility occurs at approximately 660 K and a composition of $Na_{0.014}Pb_{0.986}Te$ after which it decreases. In He's study on Na doped PbX

compounds, they assumed a constant Na solubility for their Debeye-Callaway model and noted discrepancies for temperatures greater than 550 K, where their model underestimates the lattice thermal conductivity. Although the peak does not occur until 660 K, we would expect the excess Na to begin to precipitate out of the matrix as the solubility decreases. This increases the amount of precipitates, while decreasing the amount of point defects in the matrix, both of which play key roles in the scatter of heat carrying phonons [107]. The CALPHAD and first-principles calculated formation energies are compared in Table 4.4. The formation energy of the NaTe compound lies just above the DFT determined convex hull and is not stable at 0 K; however, experimental studies have shown this to be stable at 300 K. We have included equilibria with and without this phase for a complete comparison of the DFT and CALPHAD determined energies. Despite the DFT calculations not being used in adjusting the interaction parameter, there is a close agreement between the two values, which supports our use of the 2SL model. Similar to before, the only region where the two models diverge is in the Pb-rich region where vacancies on the Te site are more prevalent.

Table 4.4: Defect formation energies at 300 K calculated by DFT and CALPAHD model for the Na-Pb-Te system. The CALPHAD interaction parameter was optimized to experimental data and agrees reasonably well with the first-principles calculations.

Equilibria	DFT Determined Formation Energy at 300 K (kJ/mol)	CALPHAD Determined Formation Energy at 300 K (kJ/mol)
PbTe-Pb-Na_2Te	37.2	55.9
PbTe-$NaTe_3$-Na_2Te	20.8	15.1
PbTe- $NaTe_3$-Te	26.5	30.0
PbTe-NaTe-Na_2Te	20.2	19.7
PbTe-NaTe-$NaTe_3$	20.2	19.7

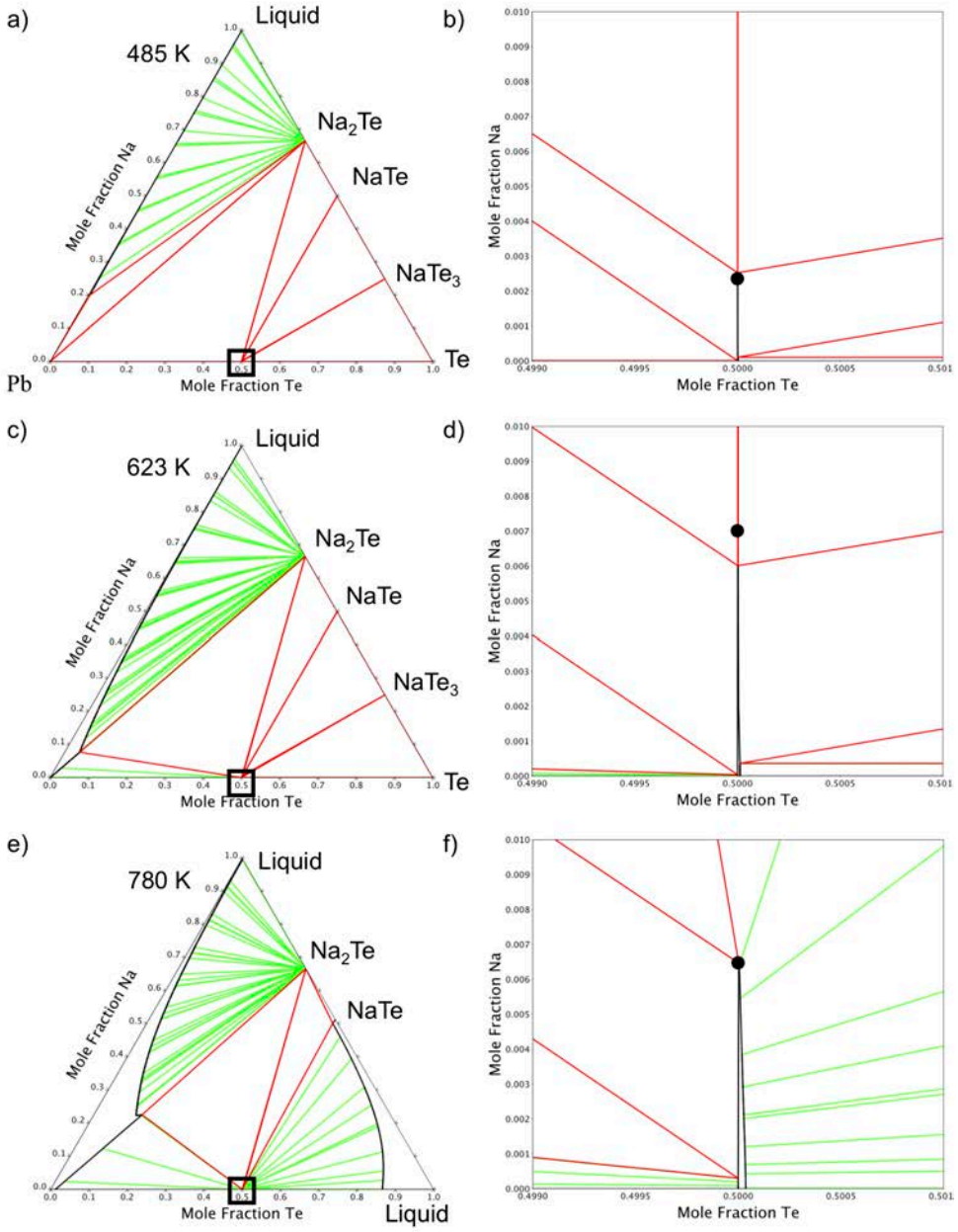

Figure 4.7: Na-Pb-Te ternary plots at (a-b) 485 K, (c-d) 623 K, (e-f) 780 K and enlarged regions for PbTe. Experimental data used in optimization from Yamini et al[114] are shown as black circles and agree well with calculations.

The solubilities of Na in PbX were found to comparatively vary in PbTe, PbSe, and PbS in increasing order [107]. The maximum solubility of Na for each compound along the NaX line is given in Figure 4.8 along with the reported solubility of each at room temperature. It is important

to note that although the study reported the solubilities as room temperature values, the experimental compounds were allowed to air cool from 1423 K. Therefore, the values they report likely indicate some higher temperature equilibrium value that was then frozen due to slower kinetics at lower temperatures. For this reason, these values were not used in the optimization and are given only for comparison. At lower temperatures, our model is consistent with the results found previously. Above 620 K, the Na solubility in PbSe overtakes PbS. PbSe experiences a decrease in Na at higher temperatures and the Na solubility of PbS becomes higher at 1260 K.

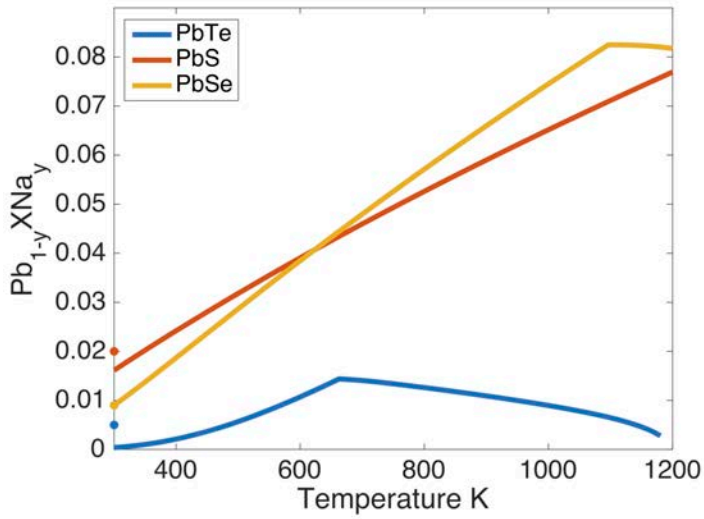

Figure 4.8: Calculated solubility of Na in PbX along NaX tie-line. The concentration of Na at low temperatures increases from increases from PbTe to PbSe and PbS, in agreement with experimental data[107], which is shown as solid circles at 300 K.

One of the benefits of the CALPHAD method is its ability to extrapolate into higher order systems. In this study, we have assessed the Pb(S,Se,Te) system as well as the solubility of Na in PbX. This allows for extrapolation into how the Na solubility changes when these compounds are alloyed together. Often, PbTe is alloyed with PbSe to take advantage of band engineering and point defects and PbS for introducing precipitates; however, they both effect the Na solubility and thus carriers of the PbTe matrix. Figure 4.9 shows the maximum carrier concentration under the assumption that each Na atom in the matrix donates one hole to the valence band for different

PbTe based systems. Our model predicts that alloying PbTe with PbS decreases the possible carriers of the system. This result is consistent with Girard's study, which found that the room temperature carrier concentration decreased from approximately 2 x 10^{20} to less than 1 x 10^{20} holes/cm^3 when PbS was introduced [99]. Conversely, alloying PbTe with PbSe increases the possible carriers, which is consistent with a study by Pei, which found a monotonic increase in carriers from 1.27 x 10^{20} to 1.65 x 10^{20} holes/cm^3 when increasing from 0% PbSe to 25% PbSe in incremental steps [82]. Simultaneous alloying of PbTe with PbSe and PbS was found to increase the carrier concentration of the PbTe matrix [103]. This result is consistent with our model at higher temperatures, which might indicate some long-term stability issues with these alloys.

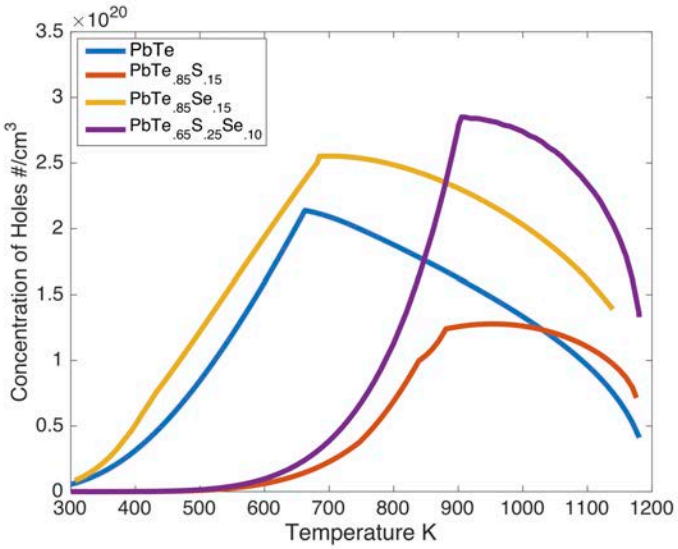

Figure 4.9: Calculated maximum number density of holes in different Pb(S,Se,Te) systems assuming that every Na atom in the matrix phase contributes one hole to the valence band. Alloying PbTe with PbSe increases the maximum carrier concentration, while alloying with PbS decreases it overall.

4.5 Conclusion

The Pb(S,Se,Te) system has been thermodynamically assessed. The literature has been critically reviewed and preference to the most reliable data has been used when the data is scattered such as in the PbS-PbSe liquidus. The liquidus data have been used to determine the interaction

parameters from the binary associates and a multicomponent compatible 2SL model has been used to describe the PbX phase, which also retains the carrier concentration from the constituent binaries. First-principles calculations are used to determine the interaction in the Pb(S,Se) solid as a miscibility gap has not been experimentally observed, due to the low temperatures, and experimental data has been used in the Pb(S,Te) and Pb(Te,Se) systems. Ternary interaction parameters were used to fully describe the Pb(S,Se,Te) ternary solid, and agrees well with the published literature data.

First-principles calculations have been performed using the dilute-limit approximation to determine the formation energies of Na on the Pb sublattice. The 2SL CALPHAD model described here can also be used to determine formation energies, which can either be compared to the DFT determined ones as in the Na-Pb-Te system or used to fix parameters in the model as in the Na-Pb-(S,Se) systems. The ternary phase diagrams around the PbX compounds have been calculated and there is good agreement between the limited experimental information and constructed models. The CALPHAD model has been used to determine the effect of alloying PbTe with PbS and PbSe and is consistent with previous publications. This thermodynamic database can be used in the optimization of lead-based chalcogenides, where solid solution, nanostructuring, and carrier concentration play key roles in optimizing the figure of merit.

5. Kinetic modeling of the PbS-PbTe system

5.1 Introduction

The work presented here has thus far been limited to the thermodynamics of various systems, which only illustrates the final equilibrium state. Often times, thermodynamic equilibrium is difficult or even impossible to obtain for reasonable timescales. Therefore, it is necessary to understand the process for which systems achieve equilibrium, which is dictated by the system's kinetics. Armed with knowledge of a system's kinetics, one can determine appropriate times and temperatures for homogenization to occur[131], annealing times to achieve a desired microstructure[132], or processing routes to avoid carburization at high temperatures for steels[133].

The process to model the kinetics is analogous to the one used in modeling the thermodynamics[134]. Once an appropriate model has been chosen for the phases of interest, adjustable parameters are then used to fit to data determined from experiment or first-principles calculations. Similar to how the Gibbs free energy is the fundamental property to model in terms of the thermodynamics, the kinetic property of interest are the mobilities of the elements in the phase. Mobilities are chosen over diffusion coefficients as there are less mobilities in a multicomponent system and interdiffusion coefficients can always be determined from the mobilities if the thermodynamics of the system are known[135]. Direct evaluation of the mobilities are difficult and instead, the diffusion coefficients, determined from diffusion couple experiments, are used as the experimental fitting data. The end goal is to build multicomponent kinetic databases that can be used in conjunction with the thermodynamic database to model diffusion-controlled phase transformation processes. If binary and ternary subsystems are properly assessed, then extrapolation to higher ordered systems is then possible.

The non-equilibrium character of kinetic processes makes the study of these parameters much more difficult than their thermodynamic counterpart. Although much work has gone into developing methods for high throughput diffusion couples, determination of diffusion coefficients is a much more complicated process both experimentally and computationally[136]. Due to these limitations, there is very limited data in the literature from which to draw on and there has yet to be an established unary database as there exists for thermodynamics. Therefore, this study must develop its own experimental information.

The previous chapter determined the thermodynamics of the PbX (X=S,Se,Te) system for which any of the pseudobinaries may be chosen. The PbS-PbTe system has been chosen as the thermodynamics of this system are well established and the miscibility gap at high temperatures allows for precipitates to form[129]. These precipitates scatter heat carrying phonons resulting in a lower lattice thermal conductivity and higher overall zT [100]. Therefore, determining the kinetics of the PbS-PbTe system would allow for greater control of the microstructure and improved thermoelectric performance. We have previously established that vacancies are the dominant defects in this system and therefore the models that use vacancy mediated diffusion processes are appropriate. In addition, the lack of antisite defects allows us to simplify the diffusion process as we can assume it only occurs on the S and Te sublattice.

This chapter will provide background on the model used for determining the kinetics of the PbS-PbTe system, the experimental conditions that were used in determining the diffusion coefficients, and the assessment of the mobilities for S and Te in the PbTe/PbS phase.

5.2 Kinetic Model

The flux of species k, J_k, in the z direction is based on Fick's first law and was generalized by Onsager[137] for a multicomponent system as

$$J_k = -\sum_{i=1}^{n} L'_{ki} \frac{\partial \mu_i}{\partial z} \quad (5.1)$$

where μ_i is the chemical potential of species *i* and L'_{ki} are proportionality factors dependent on the mobilities of the individual species. If this is rewritten in terms of concentration gradients instead of chemical potentials equation 5.1 becomes

$$J_k = -\sum_{i=1}^{n} L'_{ki} \sum_{j=1}^{n} \frac{\partial \mu_i}{\partial c_i} \frac{\partial c_i}{\partial z} \quad (5.2)$$

The unreduced diffusivities can be defined as

$$D_{kj} = \sum_{i=1}^{n} L'_{ki} \frac{\partial \mu_i}{\partial c_j} \quad (5.3)$$

and equation 5.2 can be rewritten as

$$J_k = -\sum_{j=1}^{n} D_{kj} \frac{\partial c_j}{\partial z} \quad (5.4)$$

According to equation 5.3 the diffusivities depend on the thermodynamic factor, $\partial \mu_i / \partial c_j$, and a kinetic factor L'_{ki}. The concentration gradients in equation 5.4 are not independent and in the volume-fixed frame of reference, equation 5.4 becomes

$$J_k = -\sum_{j=1}^{n-1} D_{kj}^{n} \frac{\partial c_j}{\partial z} \quad (5.5)$$

The continuity equation defined as

$$\frac{\partial c_k}{\partial z} = \frac{\partial}{\partial z}(-J_k) \quad (5.6)$$

can be combined with equation 5.5 to create a system of partial differential equations to determine the change in composition with respect to time.

The kinetic property of interest is the mobility of species *i*, M_i, and can be related to the kinetic proportionality factor by

$$L'_{kj} = \sum_{i=1}^{n}(\delta_{ik} - c_k V_i)\, c_i y_{Va} M_i \quad (5.7)$$

where δ_{ik} is the Kronecker delta function, c_k and c_i are the amounts of *k* and *i* per unit volume, V_i is the partial molar volume of element *i*, and y_{Va} is the site fraction of vacancies. From equation 5.7 and equation 5.3 it is evident that the diffusivities can be determined if the mobilities and thermodynamics of the system are known.

The method for modeling the mobilities must now be addressed. A similar model to the CEF presented earlier would lend itself well for use in multicomponent databases[134, 138]. Physically, the mobility of an element depends on the temperature, composition, pressure, frequency factor, and activation enthalpy. The mobility of element B, M_{B}, at constant pressure, temperature, and composition can be defined as

$$M_{\mathrm{B}} = \frac{M_{\mathrm{B}}^{\circ}}{RT} e^{\left(\frac{-Q_{\mathrm{B}}}{RT}\right)} \quad (5.8)$$

Where R is the gas constant, T temperature, and M_{B}° and Q_{B} are the frequency factor and activation enthalpy, respectively.

In order to describe the composition dependence, an equation similar to equations 3.6 and 3.8 are used for both M_{B}° and Q_{B}

$$\Phi_{\mathrm{B}} = \sum_i x_i \Phi_B^i + \sum_i \sum_{j>1} x_i x_j \left[\sum_{r=0}^{m} {}^{r}\Phi_{\mathrm{B}}^{i,j} \left(x_i - x_j\right)^r\right] \quad (5.9)$$

where Φ_B can be either M_B° or Q_B, x_i is the mole fraction of compoenent *i*, and ${}^r\Phi_B^{i,j}$ are the interaction parameters between components *i* and *j* of order *r*. The parameters Φ_B^i and ${}^r\Phi_B^{i,j}$ can then be adjusted in order to describe the data. For this study, only Q_B will be used to describe the data.

5.3 Determining Interdiffusion Coefficients from Diffusion Couple Experiments

Collaborators at The Ohio State University developed and analyzed diffusion couples of the PbS-PbTe system at 973 K and 1083 K for 100 hours and 24 hours, respectively. Although technically a ternary system, the analysis can be performed as a binary system as mixing only occurs on the S and Te sublattice. The two temperatures were chosen such that one was below the critical temperature of the miscibility gap, representative of a two-phase alloy, and one just above it where a solid solution should exist. The interdiffusion coefficients were determined via a forward-simulation method described below[139].

First, preliminary interdiffusion coefficients are determined using Boltzmann-Matano (B-M) analysis. A moving average method is used to smooth the experimental data and the interdiffusion coefficients, $\widetilde{D}$, as a function of composition can be determined from

$$\widetilde{D}(C') = \left(-\frac{1}{2t}\frac{dx}{dC}\right)_{C'} \int_{C_L}^{C'} (x - x_M) dC \quad (5.10)$$

where *x* is the distance coordinate, *t* is time, and C' is a specific composition at x'. The Matano plane x_M is determined by mass balance as

$$\int_{-\infty}^{x_M} [C(x) - C_L] dx = \int_{x_M}^{+\infty} [C_R - C(x)] dx \quad (5.11)$$

Where C_L and C_R are the composition at the far left and right of the composition profile, respectively. The determined interdiffusion coefficients are then fit to a constant, linear, or quadratic function. Fick's law of diffusion is then used to simulate the initial concentration profile step by step using a Boltzmann transformation. Fick's second law of diffusion states

$$\frac{\partial c}{\partial t} = \frac{\partial}{\partial x}\left(\widetilde{D}\frac{\partial c}{\partial x}\right) \quad (5.12)$$

Implementing a Boltzmann transformation where

$$\xi \equiv \frac{x}{\sqrt{t}} \quad (5.13)$$

Equation 5.12 becomes

$$-\frac{\xi}{2}\frac{dc}{d\xi} = \frac{d}{d\xi}\left(\widetilde{D}(c)\frac{dc}{d\xi}\right) \quad (5.14)$$

which greatly reduces the computation time as the concentration is only a function of ξ.

The initial composition profile is forward simulated in MATLAB using equation 5.14 for the annealing time and temperature of the experiment. The simulated composition profile is then compared to the final experimental profile and the sum of the square of the differences is computed. The diffusion coefficients are adjusted, and the initial composition is simulated again using the updated interdiffusion coefficients. This process is repeated until the sum of the square of the difference between simulated and experimental profiles is less than or equal to 0.1%.

Local equilibrium at the interface is maintained throughout the simulation. In order to determine the movement of the interface between two phases α and β, the mass balance equation is used

$$\widetilde{D}_{\alpha}\frac{\partial C}{\partial x}\Big|_{x_i}^{\alpha} - \widetilde{D}_{\beta}\frac{\partial C}{\partial x}\Big|_{x_i}^{\beta} = \left[C^{\beta}(x_i,t) - C^{\alpha}(x_i,t)\right]\frac{\partial x_i}{\partial t} \quad (5.15)$$

Two parameters are used to update the diffusion coefficients, the concentration gradient and phase thickness. The concentration gradient is inversely proportional to the diffusion coefficient at that location, as such, for a simulated and experimentally determined composition gradient, k_1 and k_2, respectively, the updated diffusion coefficient $\widetilde{D}'$ to be used in the next iteration can be calculated as

$$\widetilde{D}' = \widetilde{D}\frac{k_1}{k_2} \quad (5.16)$$

If an intermediate phase, γ, exists between the two phases α and β, then the length of the γ phase should be proportional to the diffusion coefficient due to the fact that the diffusion length is proportional to $\sqrt{\widetilde{D}t}$. Therefore, the updated diffusion coefficient can be determined as

$$\widetilde{D}' = \widetilde{D}\left(\frac{L_2^{\gamma}}{L_1^{\gamma}}\right)^2 \quad (5.17)$$

Where L_1^{γ} and L_2^{γ} are the simulated and experimentally determined length of the γ phase, respectively. The diffusion coefficients are updated and concentration profiles simulated until the experimental and simulated profiles differ by less than 0.1%.

5.4 Results and Discussion

Images of the annealed diffusion couples are shown in Figure 5.1(a) and (b) for the couple annealed at 973 K for 100 hours and 1083 K for 24 hours, respectively. The experimentally determined composition profiles are given in Figure 5.1(c) and (d). Figure 5.1(c) shows the concentration profile for the couple held at 973 K for 100 hours and Figure 5.1(d) shows the

concentration profile for the couple held at 1083 K for 24 hours. Pores evident in the image explain some of the noise seen in the composition profile, especially for the PbTe side annealed at 1083 K. These can be smoothed using the moving average method at the cost of introducing errors into the diffusion coefficient. The equilibrium composition determined at 973 K, which is below the critical temperature, was determined to be 12.5 at% S on the PbTe rich side and 44 at% S on the PbS rich side, in close agreement to 15 at% S and 45 at% S from our previously determined thermodynamic assessment.

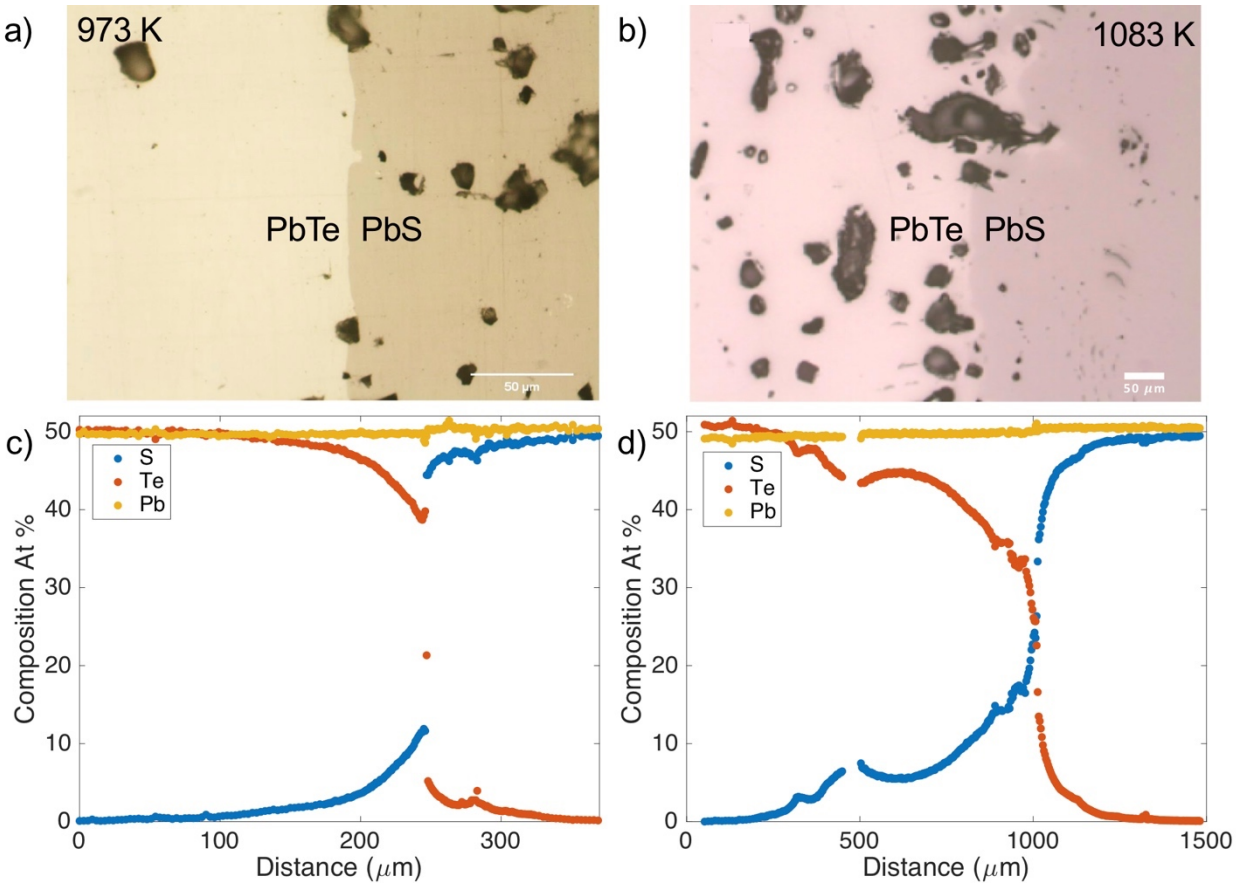

Figure 5.1: Experimental images of diffusion couples annealed at a) 973 K for 100 hours and b) 1083 K for 24 hours. The composition profiles for the annealed samples are given in c) and d) for 973 K and 1083 K, respectively.

The diffusion coefficients using the forward simulation method outlined in Section 5.3 were used to extract interdiffusion coefficients as a function of composition at the two

temperatures and are given as discrete points in Figure 5.2. The discontinuity 973 K is caused by the miscibility gap between PbTe and PbS. The full composition range can be modeled for 1083 K as it is above the critical temperature. According to equation 5.7 and 5.3, the interdiffusion coefficient is determined by the mobility M_i and the thermodynamic factor $\partial\mu_i/\partial x_S$. The minimum in the interdiffusion coefficient corresponds to the minimum of the thermodynamic factor, which is calculated from the previously determined thermodynamic assessment. Therefore, an accurate description of the kinetics involves incorporating the thermodynamics assessed earlier. A full optimization of the phase diagram along with the kinetics was thus performed.

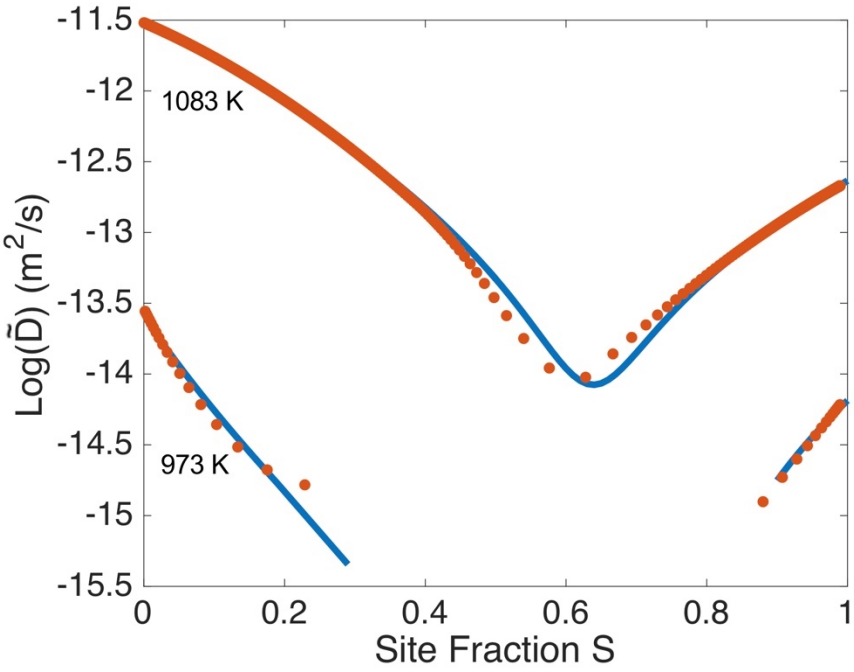

Figure 5.2: The simulated interdiffusion coefficients are shown as red points and the modeled interdiffusivities are shown as solid blue line. The interdiffusivities are shown for two temperatures, 973 K (bottom) and 1083 K (top).

The modeled diffusion coefficients are shown as a solid line in Figure 5.2 and the optimized parameters are given in Table 5.1. There is close agreement between the data and model near the PbTe and PbS end-members that begin to deviate further away from the pure components. Errors

can be magnified when the composition gradient is unclear, which occurs at the interface and therefore we would expect greater uncertainty at those locations. The kinetic and thermodynamic parameters were used to perform a diffusion couple simulation in the DICTRA software. Initial composition profiles were created to represent blocks of PbTe and PbS forced together and annealed at the experimental temperature and time. The simulated profiles along with the experimental data, shown in green, are given in Figure 5.3. Despite the slight discrepancy between the interdiffusion coefficients, the simulated and experimental concentration profiles agree very well with each other. Lastly, the miscibility gap and experimental data is shown in Figure 5.4 with the original assessment shown in red and the updated assessment including the kinetic information, shown in black. The miscibility gap is largely unchanged with the kinetic information; however, a temperature dependent term in the sub-regular solution model was added in order to better describe the data. The addition of this term is justified as there is more experimental information to fit to and the updated interaction parameters are given in Table 5.2 along with the previous values.

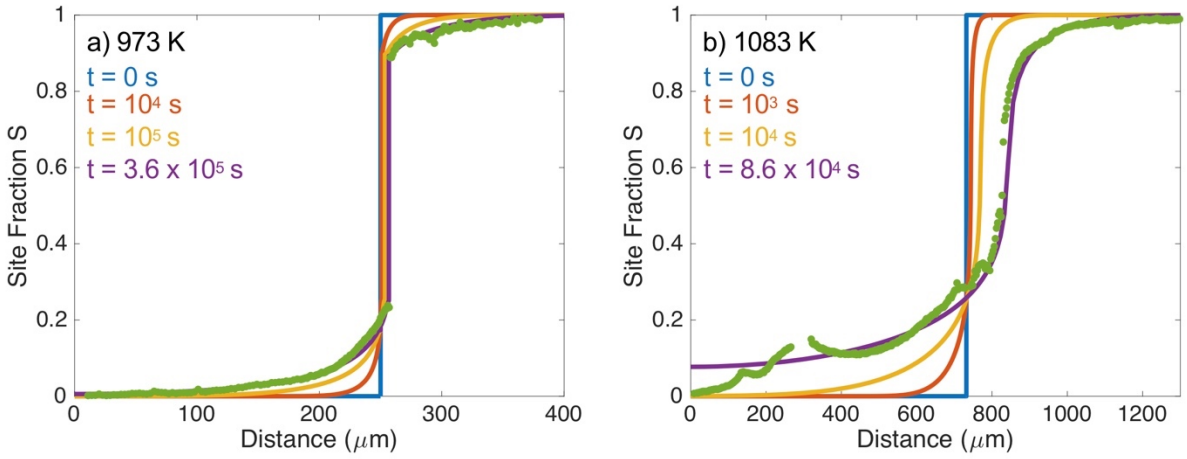

Figure 5.3: Simulated diffusion profiles and experimental data shown for a) 973 K at 100 hours and b) 1083 K at 24 hours using the updated kinetic and thermodynamic assessments.

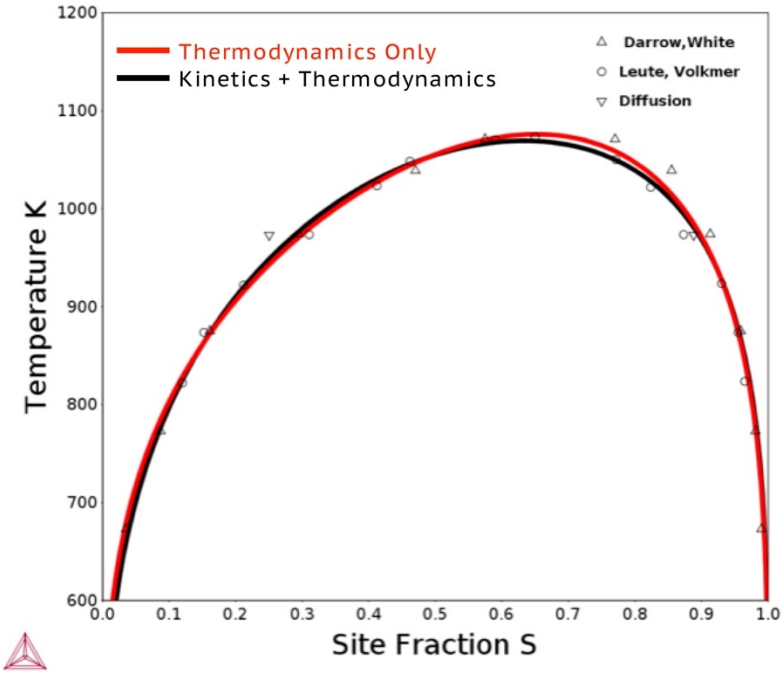

Figure 5.4: Comparison of the calculated phase diagram for the assessment containing thermodynamic information only (red) and the assessment using kinetic and thermodynamic information (black).

Table 5.1: Final optimized kinetic parameters for Pb(S,Te)

Parameter	Optimized Value (J/mol)
$Q_X^{Pb:Te}$	-384,100+134.6T
$Q_X^{Pb:S}$	-286,300+22.5T
${}^0Q_X^{Pb:S,Te}$	-504,000+440.7T
${}^1Q_X^{Pb:S,Te}$	461,200-430.5T

Table 5.2: Updated thermodynamic parameters after performing full assessment of thermodynamic and kinetic information in comparison to previous assessment.

Interaction Parameter	Thermodynamic Assessment (J/mol)	Thermodynamic and Kinetic Assessment (J/mol)
${}^0L_{Pb:S,Te}^{PbX}$	$38{,}224 - 20.9T$	$37{,}228 - 19.7T$
${}^1L_{Pb:S,Te}^{PbX}$	4,372	$8{,}062 - 4.1T$

One method for validating the derived diffusion data is to compare the interdiffusion coefficients to the impurity diffusion coefficients of the pure compounds, PbTe and PbS. According to Darken's equation, the interdiffusion coefficient is equal to[140]

$$\widetilde{D} = x_B D_A + x_A D_B \quad (5.18)$$

where D_A and D_B are the intrinsic diffusivities of components A and B. Therefore, at the end-member compositions, the interdiffusion coefficient should reduce to the intrinsic diffusivity or impurity diffusivity in PbTe and PbS. Unfortunately, there are no literature values for the impurity diffusivity of Te and Se in PbS and PbTe, respectively. In addition, most of the impurity diffusivities in the literature, such as Ag, Sb, or Bi, are not substitutional defects on the X sublattice and therefore not a fair comparison. The best literature values are the self-diffusion coefficients of Te and S in their respective compounds. The self-diffusion coefficient is highly dependent on the growth conditions of the material and can vary by an order of magnitude if grown on either the Pb-rich or X-rich side[141, 142]. The self-diffusion coefficients of S[142] and Te[141] from the literature and the modeled interdiffusivities at either end-member are given in Table 5.3. The data is most aligned for the low temperature 973 K, and the modeled diffusivities are much larger at the higher temperature. The higher temperature was chosen to be above the critical point, which was previously determined to be a temperature of 1076 K. There is only a 7 K difference between the critical point and the 1083 K annealing temperature. Modeling diffusion near the critical point is notoriously difficult as classical nucleation theory does not apply[143]. Therefore, we would expect this region to be particularly difficult to model and this explains some of the discrepancy near the minimum. However, this issue should be mitigated near the end-members where the composition is farther from the critical point. It is also important to note that the self-diffusion coefficients are extrapolated from a lower temperature and therefore cannot be guaranteed to describe the diffusion at higher temperatures. Nevertheless, the activation energy of 380 kJ/mole and 290 kJ/mole for PbTe and PbS, respectively, compare reasonably well to those found in other

kinetically assessed systems such as the Ni-Nb-Mo, which range from 280 kJ/mole to 315 kJ/mole[144] or the Al-Cr-Ni found to range between 142 kJ/mole to 287 kJ/mole[138].

Table 5.3: Comparison of experimentally determined self-diffusion coefficients and the modeled interdiffusion coefficients at either end-member.

Temperature (K)	Self-Diffusion of S (m^2/s) [142]	Interdiffusion of S (m^2/s)	Self-Diffusion of Te (m^2/s) [141]	Interdiffusion of Te (m^2/s)
973	2.2×10^{-15}	6.5×10^{-15}	1.1×10^{-15}	2.5×10^{-14}
1083	9.6×10^{-15}	2.3×10^{-13}	3.8×10^{-15}	3.0×10^{-12}

5.5 Conclusions

Diffusion couples of the PbTe-PbS system were created and annealed at two temperature 973 K and 1083 K for 100 and 24 hours, respectively. The composition profiles of the annealed samples were used to determine the interdiffusion coefficients using a forward simulation method. The equilibrium composition determined from the diffusion couple is in close agreement with our previous thermodynamic assessment. The simulated diffusion coefficients were used to model the mobilities of the PbX phase. In order to get a satisfactory agreement with the diffusion coefficients, a combined assessment of the thermodynamic and kinetic data was necessary. The updated thermodynamic and new kinetic parameters have been reported and reasonable agreement with the data is shown. The mobility and thermodynamic databases were used to simulate the experimental diffusion couples and excellent agreement between the simulated and experimental profiles is shown. Discrepancies are seen in the interdiffusivity coefficients of the data annealed at 1083 K, which could be explained by the proximity of the critical point at this temperature. Comparison of the interdiffusivities and the self-diffusion coefficients show better agreement at the lower temperature, which further indicates that the higher temperature data may not be as reliable and should require further study. The assessed parameters are consistent with previously determined kinetic parameters for other systems.

6. Thermodynamic modeling of the semiconductor compounds and homologous series in the Bi-Te, Bi-Se, and Sb-Te binary systems

6.1 Introduction

This work has so far focused on the modeling of the PbX (X=S,Se,Te) compounds and alloys within the system. The 5SL model and 2SL model have been used to effectively model the defects of the semiconductors as well as construct the system phase diagrams. Not all thermoelectric compounds follow a simple AB stoichiometric formula; however, the methodology used in developing the 2SL model is quite flexible and can be used in numerous applications. One of the most promising low to mid temperature range thermoelectric materials is Bi_2Te_3, which is often alloyed with Bi_2Se_3 and Sb_2Te_3[145]. The optimized carrier concentration has been shown to be on the order of 10^{19} carriers/cm^3 for Bi_2Te_3[146], which can have intrinsic carriers ranging from 10^{18} to 10^{19} carriers/cm^3[147]. Therefore, the intrinsic carriers, and consequently the processing conditions, must be taken into account when developing a fully optimized material. In addition to their thermoelectric applications, these materials are also intriguing as topological insulators and Sb_2Te_3 is a phase change material, which can play an important role in random access memory devices [148] [149].

The three systems also each contain an infinitely adaptive series of homologous compounds between the compositions of A and A_2Q_3 (A=Bi, Sb; Q=Te, Se) [150] [151, 152]. The compounds consist of layers of $(A_2)_n(A_2Q_3)_m$, where n and m can take any positive integer. This has been seen experimentally and verified through first-principles calculations via cluster expansion methods [153]. Theoretically, all compositions between 0 and 60 at% Q have a stable compound, which is not seen experimentally[154-156]. In all three systems, the compound with highest composition Q appears to be A_4Q_5. Beyond this, a two-phase equilibria exists between

A_4Q_5 and A_2Q_3, which then becomes in equilibrium with pure Q. The homologous compound that is most A-rich is dependent on the system. For Bi-Te and Sb-Te, a compound at A_7Q_3 is stable, whereas in Bi-Se the series begins at A_3Q_2. The intermediary compounds are often consolidated into one or more phase that exhibit large regions of homogeneity[157-159]. In turn, these phases were then thermodynamically modeled as solution phases with random mixing. However, experiments and first-principles calculations now indicate a very clear ordered compound consisting of layers of A_2 and A_2Q_3; thus indicating that solution phases are an inappropriate model for describing the system.

Homologous compounds are not unique to the A-B systems nor CALPHAD assessments. Oxides in the M_nO_{2n-m} (M = Pr, Ce, or Tb) where n and m are any positive integer and n > m form an infinite series as well. In a recent assessment of the Pr-O system, these phases were treated as stoichiometric functions with individual descriptions of the Gibbs free energy. The heat capacity was modeled using the Neumann-Kopp rule and the enthalpies of formation were fit to interpolated data between the Pr_2O_3 and Pr_6O_{11}. This method is physically accurate; however, the fact that the functions are able to vary individually mean that their enthalpies of formation will likely not fall on the linear interpolation, therefore a better method should be adopted.

In this study, the experimental and first-principles calculations available in the literature will be reviewed and critically assessed. The defects in A_2Q_3, which have been previously modeled as line compounds, will be taken into account and their off-stoichiometry calculated and parameters linked to the formation energy of the defects to ensure physical accuracy. The homologous series in each system will be bounded by line compounds that indicate their stability from experiments and a metastable region will be shown between them due to lack of information on the infinite compounds' melting point. To ensure that enthalpies of formation lie on a linear

convex hull between A and A_2Q_3, the homologous compounds will be modeled by a linear combination of A and A_2Q_3 based on the stoichiometric composition. This method forces the enthalpies of formation to reproduce what is seen in the first-principles calculations.

6.2 Literature Review

6.2.1 Bi-Te

There is limited experimental information on the phase equilibria in the Bi-Te system as compared to both Bi-Se and Sb-Te. The first published phase diagrams were established by Hansen and Abrikosov[160, 161]. The phase diagram published by Hansen exhibits one intermetallic compound, Bi_2Te_3, with a large degree of homogeneity, while the phase digram in Abrkosov establishes the compounds BiTe, Bi_2Te, and Bi_7Te_3 with varying degrees of homogeneity. This study was primarily used for the thermodynamic modeling performed by Chizhevskaya[154]. The phase diagram by Okamoto is the first one to show a series of infinite compounds between Bi_7Te_3 and Bi_2Te_3[162]. Brebrick established the nonstoichiometric nature of the Bi_2Te_3 phase using partial pressure measurements and established the congruent melting point of the compound to be slightly Bi-rich[147], in agreement with the results of Offergeld[163]. Brebrick also determined that Bi-rich samples were dominated by Bi substituting on the Te site and acting as acceptors, and Te substituting on Bi acting as donors on the Te-rich side. This was confirmed using first-principles calculations in the dilute limit taking into account spin-orbit interactions[164, 165]. In a recent experimental and thermodynamic study by Mao, the homogeneity limits of the infinite series was found to be between approximately 27 and 55 atomic % Te[157]. In addition, two phases were found to be particularity stable in the melt at compositions Bi_2Te and Bi_4Te_3.

The activity of Bi-Te melts were studied by Predel[166] and Feutelais[167] and used in this study. The enthalpy of mixing was determined by Maekawa[168] and Morgant[169] and both

exhibit minimum near the Bi_2Te_3 composition. The heat capacity for Bi_2Te_3 was studied by Feng[170] and Zurhelle[171] and modeled by Mao[157], who's values are used in this study as no further information has been published.

Bos experimentally determined that the separate intermetallic phases in the Bi-Te phase diagram actually consisted of an infinitely adaptive series of $(Bi_2)_m(Bi_2Te_3)_n$ blocks where m and n are any positive integer[150]. Therefore, the regions of large homogeneity shown in phase diagrams actually consists of distinct line compounds that exist at every composition if annealed long enough. This was later confirmed by Govaerts using cluster expansion methods based on first-principles calculations that found that these structures all lie on the convex hull between Bi and Bi_2Te_3[153].

There are limited thermodynamic assessments on this system. The one performed by Chizhevskaya models Bi_2Te_3 and Bi_7Te_3 as line compounds and Bi_2Te and BiTe as solution phases without presenting any thermochemical information on the liquid[154]. The most recent one performed by Mao uses a solution phase, β, to represent the homologous compounds and two line compounds, Bi_2Te and Bi_4Te_3, they found to be stable in the melt[157]. In addition, Bi_2Te_3 is modeled as a line compound.

6.2.2 Bi-Se

The phase equilibria in the Bi-Se system has been extensively studied and similar in nature to Bi-Te except for a miscibility gap in the liquid on the Se rich side. The liquidus was investigated by Parravano[172], Tomoshige[173], Abrikosov[174], Ohashi[175], Gather[176], Bros[177], and Sher[178]. Three intermetallics are generally shown in the phase diagram at Bi_2Se_3, BiSe, and Bi_3Se_2. The BiSe is generally modeled as a solution phase and Bi_3Se_2 and Bi_2Se_3 modeled as line compounds. Bi_2Se_3 melts congruently, while BiSe and Bi_3Se_2 both melt incongruently. Offergeld

determined the congruent melting temperature of Bi_2Se_3 to slightly Bi-rich, showing similar nonstoichiometry as Bi_2Te_3[163], and Huang measured the carrier concentration of Bi-rich and Se-rich Bi_2Se_3 annealed at 300° C[179]. First-principles and experimental information agree that the dominant defects are Se vacancies and Se antisites for Bi-rich and Se-rich growth conditions, respectively[164, 180, 181].

The thermochemical information of the system is also well established. The activity of Bi-Se melts is studied by Predel[182]. The enthalpy of mixing is established by Maekawa[183] and Bros[177], both of which show strong ordering at the Bi_2Se_3 composition. The heat capacity of Bi_2Se_3 determined by Pashinkin [184], Rasulov [185], Blachnik [186], and Gol'tsman [187] are all in good agreement. In addition, the recorded enthalpies of formation of Bi_2Se_3 are also all in agreement at around -28 kJ/mol.

Similar to Bi-Te, Bi-Se also exhibit homologous compounds of layered stacking $(Bi_2)_m(Bi_2Se_3)_n$ between the compositions of Bi_3Se_2 and Bi_4Se_5. Again, this observations is confirmed via first-principles by Govaerts [153]. Experimentally, these compounds are observed between 40 and 55 at% Se [155].

The thermodynamic assessments by Antipov[188] and Chen[158] are qualitatively quite similar. BiSe is a solution phase, while Bi_3Se_2 and Bi_2Se_3 are line compounds. Neither study contains information on the nonstoichiometric nature of Bi_2Se_3 nor the heat capacity of the phase, both of which are addressed in this study.

6.2.3 Sb-Te

There are numerous studies on the phase equilibria of the Sb-Te system. The first phase diagrams consist of only one intermetallic compound, Sb_2Te_3, with a wide range of homogeneity [189]. A study done by Abrikosov identified two other solution phases, δ and γ, between 20 and

40 and 45 to 55 atomic percent Te, respectively [190]. The phase diagram with three intermetallics is now widely accepted and used in the literature [191] [159]. The γ phase forms via a peritectic reaction with liquid and Sb_2Te_3. The δ phase has a minimum in its liquidus where it melts congruently near a composition of 30 at% Te and has peritectic reactions on either side of the minimum. Sb_2Te_3 forms a eutectic with Te near 92 at% Te. The solid solubility of Te in Sb was studied by Abrikosov[190] and Poretskaya[192] and Offergeld[163] as well as the non-stoichiometry of Sb_2Te_3, which melts congruently on the Sb-rich side of the stoichiometric composition. The dominant defects in Sb_2Te_3 have been determined by experiment in agreement with first-principles calculations as Sb vacancies and Sb substituting for Te on the Te site for Te-rich and Sb-rich growth conditions, respectively [164, 193].

There are numerous thermochemical studies done on the Sb-Te system as well. The enthalpy of mixing of Sb-Te melts was determined by Feutelais[194] and Maekawa[195] at different temperatures and are in agreement. Both indicate a minimum in the enthalpy at a compostion near 60 at% Te. The activity of Sb-Te melts was recorded by Onderka[196] and Feutelais[194] and show deviations from ideality as well. The heat capacity of Sb_2Te_3 has several studies all in close agreement. The parameters from Guo[159] for the heat capacity of Sb_2Te_3 are adopted in this work as no updated information is available. The experimental enthalpy of formation of Sb_2Te_3 has also been investigated and ranges from -12 to -15 kJ/mole of atoms [197-199].

Identical to the Bi-Te and Bi-Se systems, Sb-Te also exhibit homologous compounds of $(Sb_2)_m(Sb_2Te_3)_n$. This has been proven experimentally and confirmed via first-principles calculations[151, 164, 200]. The bounds of the homologous series have been observed between 20 and 55 at% Te.

Ghosh[191] and Guo[159] have both thermodynamically assessed the Sb-Te and are qualitatively very similar. Ghosh's assessment came before an agreed upon unary database, which was used in Guo's updated assessment. Guo modeled the δ and γ phases as solution phases and the Sb_2Te_3 as a stoichiometric line compound. Guo developed two assessments using an ionic and associate model for the liquid, with only slight differences in the two assessments.

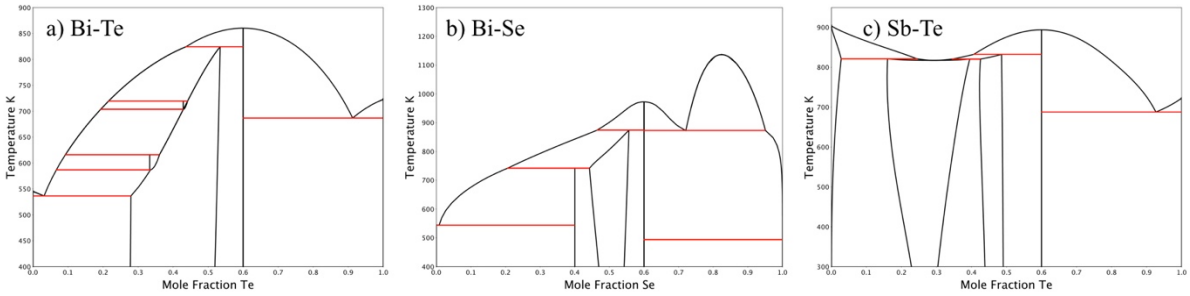

Figure 6.1: Phase Diagrams from previous thermodynamic assessments a) Bi-Te [157] b)Bi-Se [158] c) Sb-Te [159]. Each assessment uses a solution model to model the infinite series of homologous compounds in each binary.

6.3 Computational Modeling

6.3.1 CALPHAD models for Bi-Te

The liquid was modeled using a single sublattice substitutional model expressed as

$$G^l = x_{Bi}G^l_{Bi} + x_{Te}G^l_{Te} + RT(x_{Bi}\ln x_{Bi} + x_{Te}\ln x_{Te}) + x_{Bi}x_{Te}\sum_{i=0}^{n} {}^iL^l_{Bi,Te}(x_{Bi} - x_{Te})^i \quad (6.1)$$

where x_j, G^l_j, ${}^iL^l_{Bi,Te}$, R and T are the mole fraction and Gibbs energy of element j in the liquid phase, Redlich-Kister coefficient, gas constant, and temperature, respectively. The parameters ${}^iL^l_{Bi,Te}$ are temperature dependent parameters determined as

$$ {}^iL^l_{Bi,Te} = A_i + B_iT \quad (6.2)$$

where A_i and B_i are fitting parameters optimized to describe the data.

The compound Bi_2Te_3 was modeled using a three sublattice (3SL) model that represents each of the three nonequivalent sites. Based on the experimental work and reinforced by first-principles calculations, the primary defects in Bi_2Te_3 are anti-sites. Therefore, the model is described as (**Bi**,Te)$_2$(**Te**,Bi)$_1$(**Te**)$_2$ where the bolded element is the dominant element on each site. According to the Compound Energy Formalism (CEF), the Gibbs free energy of Bi_2Te_3 is calculated as

$$G^{m}_{Bi_2Te_3} = \sum_i \sum_j y'_i y''_j G_{i:j:Te} + RT\left(2\sum_i y'_i ln y'_i + \sum_j y''_j ln y''_j\right) + {}^{E}G_m \quad (6.3)$$

where y'_i, y''_i, $G_{i:j:Te}$, and ${}^{E}G_m$ are the site fraction of component i on the first sublattice, the site fraction of component j on the second sublattice, the Gibbs free energy of a compound with sublattices completely filled with i and j, and the excess Gibbs free energy. The excess Gibbs free energy is dictated by the defects on the system and modeled as

$${}^{E}G_m = y'_i y'_j\left(y''_i L_{i,j:i} + y''_j L_{i,j:j}\right) + y''_i y''_j\left(y''_i L_{i:i,j} + y''_j L_{j:i,j}\right) + y'_i y'_j y''_i y''_j L_{i,j:i,j} \quad (6.4)$$

Since there are only two dominant defects in this system, only the parameters $L_{i,j:i}$ and $L_{i,:i,j}$ are necessary to describe the data, which represent the mixing of the antisites on the Bi and Te sublattice, respectively.

The stoichiometric end-member $G_{Bi_2Te_3}$ is modeled using a power series in temperature

$$G^{Bi_2Te_3}_{Bi:Te:Te} = a + bT + cTln(T) + dT^2 + eT^3 + fT^{-1} \quad (6.5)$$

where a, b, c, d, e, and f are fitting parameters. The coefficients c, d, e, and f are related to the heat capacity of Bi_2Te_3 and are taken from Mao[157]. Coefficients a and b are optimized in this work.

The end-members $G_{Bi:Bi:Te}$, $G_{Te:Te:Te}$, and $G_{Te:Bi:Te}$ are fixed using formation energies determined via first-principles calculations of structures with fully occupied elements in their respective sites.

This sublattice model can be used to link the fitting parameters to the formation energies of defects that can be determined either through experiments or first-principles calculations [112]. The measured carrier concentrations are made through equilibrating Bi_2Te_3 in either Bi-rich or Te-rich conditions where the dominant defects are Bi antisites and Te antisites, respectively. Due to the change in chemical potentials in the different growth conditions, the formation energy of the minor defect drastically increases and can be considered negligible, which allows us to approximate the 3SL model as $(Bi)_2(Bi,Te)_1(Te)_2$ and $(Bi,Te)_2(Te)(Te)_2$ under Bi-rich and Te-rich growth conditions, respectively. To determine the equilibrium concentration of Bi antisites under Bi-rich growth conditions we can minimize the grand potential, described as:

$$\mathcal{G}_m = G^m_{Bi_2Te_3} - \mu_{Bi} y''_{Bi} - \mu_{Te} y''_{Te} \quad (6.6)$$

Where $\mathcal{G}_m$, μ_{Bi}, and μ_{Te} are the grand potential per mole and chemical potential of Bi and Te atoms respectively and $G^m_{Bi_2Te_3}$ is determined using a simplified version of equation 6.3:

$$G^m_{Bi_2Te_3} = \sum_j y^{"}_j G_{Bi:j:Te} + RT\left(\sum_j y^{"}_j ln y^{"}_j\right) + y''_{Te} y''_{Bi} L_{Bi:Bi,Te:Te} \quad (6.7)$$

The derivative of equation 6.6 with respect to y_{Te} is set equal to zero and then becomes

$$0 = \frac{dG^m_{Bi_2Te_3}}{dy_{Te}} - \mu_{Te} + \mu_{Bi} \quad (6.8)$$

Substituting the derivative of equation 6.7 with respect to y_{Te} and substituting that into equation 6.8 then leads to

$$-\ {}^{\circ}G_{Bi:Bi:Te} + {}^{\circ}G_{Bi:Te:te} + L_{Bi:Bi,Te:Te}(1-2y_{Te}) - \mu_{Te} + \mu_{Bi} = -RTln\left(\frac{y_{Te}}{1-y_{Te}}\right) \quad (6.9)$$

Lastly, we substitute1-y_{Bi} for y_{Te} and treat 1-y_{Bi} as equal to one under the dilute limit where $y_{Bi} \ll 1$. Solving for y_{Bi}:

$$y_{Bi_{Te}}^{eq} = \exp\left(-\frac{{}^{\circ}G_{Bi:Bi:Te} - {}^{\circ}G_{Bi:Te:Te} + L_{Bi:Bi,Te:Te} + \mu_{Te} - \mu_{Bi}}{RT}\right) \quad (6.10)$$

The numerator is equivalent to the formation energy of a Bi antisite defect. The Gibbs free energy of the end-member ${}^{\circ}G_{Bi:Bi:Te}$ can be fixed and determined by first-principles calculations while the end-member ${}^{\circ}G_{Bi:Te:Te}$ is the defect free crystal and determined through experimental information. The chemical potentials are constant as the Bi-rich region is in a two-phase equilibrium of either Bi_2Te_3 and Bi_4Te_5 or Bi_2Te_3 and the liquid phase. This leaves the interaction parameter, $L_{Bi:Bi,Te:Te}$, free to be optimized in order to describe the experimental data or fit to first-principles derived calculations. An analogous derivation can be used for the site fraction of Te on the Bi sublattice under Te-rich conditions with the end result being:

$$y_{Bi_{Te}}^{eq} = \exp\left(-\frac{{}^{\circ}G_{Te:Te:Te} - {}^{\circ}G_{Bi:Te:Te} + L_{Bi,Te:Te:Te} + 2\mu_{Bi} - 2\mu_{Te}}{2RT}\right) \quad (6.11)$$

Here the factor of 2 appears as there are two sites in the Bi sublattice.

The intermetallic compounds Bi_7Te_3 and Bi_4Te_5 represent different stacking sequences of the infinitely adaptive structures of Bi_2 and Bi_2Te_3. Therefore, these compounds have been modeled as a mixture of $G_{Bi_2Te_3}$ and G_{Bi} and a temperature dependent fitting coefficient. This

procedure forces their formation energies to lie on the convex hull between rhombohedral Bi and Bi_2Te_3 as predicted by first-principles calculations. They are given as

$$G^{Bi_4Te_5} = \frac{5}{3}G^{Bi_2Te_3} + \frac{2}{3}G^{Bi} + B^{Bi_4Te_5}T \quad (6.12)$$

$$G^{Bi_7Te_3} = G^{Bi_2Te_3} + 5G^{Bi} + B^{Bi_7Te_3}T \quad (6.13)$$

6.3.2 CALPHAD models for Bi-Se

Due to the strong enthalpy of mixing in the liquid phase around the composition 60 at% Se, an associate model (Bi, Se, Bi_2Se_3) was used for the liquid. The molar Gibbs energy is expressed as:

$$G^{l} = x_{Bi}G^{l}_{Bi} + x_{Se}G^{l}_{Se} + x_{Bi_2Se_3}G^{l}_{Bi_2Se_3} + RT\left(x_{Bi}\ln x_{Bi} + x_{Se}\ln x_{Se} + x_{Bi_2Se_3}\ln x_{Bi_2Se_3}\right) + {}^{E}G_{m} \quad (6.14)$$

Similar to Bi_2Se_3, a three sublattice model for Bi_2Se_3 was used. However, the dominant defects are Se on the Bi site and vacancies on the Se site. Therefore, the model is described as (**Bi**,Se)$_2$(**Se**,Va)$_1$(**Se**)$_2$. In order for this model to be compatible with the Bi-Te system, a ${}^{\circ}G_{Bi:Va:Te}$ and ${}^{\circ}G_{Te:Va:Te}$ end-member will need to be defined. These can be set similar to the method outlined in section 3.2.2 and will have negligible effect in the Bi-Te binary as the defects are insignificant in that system. Similar derivations can be done on this and the site fraction for the dominant defects on Bi-rich and Se-rich side, respectively, are:

$$y^{eq}_{Va_{Se}} = \exp\left(-\frac{{}^{\circ}G_{Bi:Va:Se} - {}^{\circ}G_{Bi:Se:Se} + L_{Bi:Se,Va:Se} + \mu_{Se}}{RT}\right) \quad (6.15)$$

$$y^{eq}_{Se_{Bi}} = \exp\left(-\frac{{}^{\circ}G_{Se:Se:Se} - {}^{\circ}G_{Bi:Se:Se} + L_{Bi,Se:Se:Se} + 2\mu_{Bi} - 2\mu_{Se}}{2RT}\right) \quad (6.16)$$

Here the chemical potential of vacancies is set to zero. The end-member ${}^{\circ}G_{Se:Se:Se}$ can again be fixed to first-principles calculations. The end-member ${}^{\circ}G_{Bi:Va:Se}$ requires special care due to the introduction of vacancies. Modeling vacancies has been a difficult task in the CALPHAD community and there have been a number of recent publications that attempt to address this issue [31, 87] [88]. Previously, these end-members were simply given a value of zero; however, this would imply that they become stable at some high temperature and can cause issues with extrapolations. Rogal suggests using a function of 2.3RT to serve as a penalty function for creating vacancies [31], while other publications use 30T [88]. Franke established that a value greater than $\ln(2-1/2)$RT was necessary in order for their to be a unique solution to determining the vacancy concentration and recommended the value of 0.2RT [87]. For this work, we have adopted the value of 2.3RT as suggested by Rogal and used by Peters et al [112] to be consistent with other thermoelectric semiconductors.

The intermetallics Bi_4Se_5 and Bi_3Se_2 are modeled here as stoichiometric mixtures of Bi_2Se_3 and Bi. Their Gibbs free energy is expressed as:

$$G^{Bi_4Se_5} = \frac{5}{3}G^{Bi_2Se_3} + \frac{2}{3}G^{Bi} + B^{Bi_4Se_5}T \quad (6.17)$$

$$G^{Bi_3Se_2} = \frac{2}{3}G^{Bi_3Se_2} + \frac{3}{2}G^{Bi} + B^{Bi_3Se_2}T \quad (6.18)$$

6.3.3 CALPHAD models for Sb-Te

Past assessments have used both an associate or ionic liquid model in describing the Sb-Te melt. This study determined that a substitutional model was sufficient to describe the experimental data. In addition, the enthalpy of mixing is not nearly as strong as in the Bi-Se system, further

indicating that a more complicated model is unnecessary. Therefore, the liquid was described using an equation analogous to equation 6.1.

According to Abrikosov et al[190], the rhombohedral phase of Sb exhibits solubility of approximately 1 at% Te. Therefore, a substitutional model of (Sb,Te) will be used to describe this phase similar to equation 6.1. The end-member G_{Sb}^{Rhom} is already definited in the SGTE database and the end-member G_{Te}^{Rhom} can be fixed to first-principles calculations of the formation energy of Te in the rhombohedral crystal structure. The interaction parameter, ${}^{0}L_{Sb,Te}^{Rhom}$, will be fit to the solubility data of Abrikosov.

The dominant defects in Sb_2Te_3 are Sb antisites and Sb vacancies. Therefore the three sublattice model is described as (**Sb**,Va)$_2$(**Te**,Sb)$_1$(**Te**)$_2$. The equations used to determine the site fraction of defects on their respective sublattices for Sb-rich and Te-rich growth conditions, respectively, are:

$$y_{Sb_{Te}}^{eq} = exp\left(-\frac{{}^{\circ}G_{Sb:Sb:Te} - {}^{\circ}G_{Sb:Te:Te} + L_{Sb:Sb,Te:Te} + \mu_{Te} - \mu_{Sb}}{RT}\right) \quad (6.19)$$

$$y_{Va_{Sb}}^{eq} = exp\left(-\frac{{}^{\circ}G_{Va:Te:Te} - {}^{\circ}G_{Sb:Te:Te} + L_{Sb,Va:Te:Te} + 2\mu_{Sb}}{2RT}\right) \quad (6.20)$$

The end-member ${}^{\circ}G_{Sb:Sb:Te}$ is determined via first-principles calculations and the end-member ${}^{\circ}G_{Va:Te:Te}$ uses 2.3RT as a penalty function for the creation of vacancies.

The Sb-Te system behaves similarly to the Bi-Te in that the homologous compounds are bound by Sb_7Te_3 and Sb_4Te_5. The intermetallics are described as

$$G^{Sb_4Te_5} = \frac{5}{3}G^{Sb_2Te_3} + \frac{2}{3}G^{Sb} + B^{Sb_4Te_5}T \quad (6.21)$$

$$G^{Sb_7Te_3} = G^{Sb_2Te_3} + 5G^{Sb} + B^{Sb_7Te_3}T \quad (6.22)$$

6.3.4 First-principles calculations

The end-members of A_2Q_3 containing non-vacancy defects were modeled using the enthalpy of formation determined using first-principles calculations. The total energies of the stoichiometric and fictitious compounds were determined by DFT [35] performed with the Vienna Ab-initio Simulation Package (VASP) [37, 201] with projector-augmented wave [39] (PAW) potentials utilizing the generalized gradient approximation (GGA) exchange correlation functional of Perdew, Burke, and Ernzerhof[40] (PBE). These calculations treat the $s^2d^{10}p^3$, s^2p^3, s^2p^4, and s^2p^4 electrons as valence for Bi, Sb, Te, and Se atoms, respectively. Crystal structures were taken from the Inorganic Crystal Structure Database (ICSD) [41]. The 15 atom unit cell was used and allowed to relax with a maximum cutoff energy of 520 eV and a 13x13x13 gamma k-point mesh[42]. Lattice parameters and atomic positions were allowed to relax until energy convergence reached 0.1 meV and a final static calculation was performed to determine the total energy.

6.3.5 Assessment Procedure

The optimization is performed through the PARROT module of ThermoCalc [90]. The Gibbs free energies of the elements in their SER and liquid states are taken from the SGTE database [86]. The parameters for the liquid were first determined using enthalpy of mixing measurements and the activity of the components in the melt. Initially, the A_2Q_3 compounds were modeled as line compounds. In the case of the Bi_2Se_3, the coefficients *c*, *d*, *e*, and *f* from equation 6.5 were fit to the heat capacity data. The coefficients for Bi_2Te_3 and Sb_2Te_3 were taken from Mao[157] and Guo[159]. The coefficient a from equation 6.5 was fit to the enthalpy of formation and the coefficient b was fit to the melting point. The temperature dependent term in the other

intermetallic compounds of the system were then optimized to describe their melting points and no other fitting parameters were used to ensure their formation energies stayed on the convex hull. After a satisfactory fit was accomplished to all the phase and thermochemical information, the compounds A_2Q_3 were changed to their respective 3SL models and the interaction parameters were optimized to describe either the phase boundary that had either been determined experimentally or through first-principles calculations.

6.4 Results and Discussion

6.4.1 Bi-Te

The final optimized parameters for the Bi-Te system are summarized in Table 6.1. The enthalpies of mixing and activity of Bi-Te melts and experimental information are shown in Figure 6.4 and Figure 6.5, respectively. Despite the minimum near 60 at% Te, agreement with the experimental data was achieved without the use of an associate or ionic liquid model. The limited experimental information on the phase diagram is shown in Figure 6.2, in good agreement, along with an enlarged region of Bi_2Te_3 in Figure 6.3. The gray shaded region is considered metastable and represents the infinite series of homologous compounds between Bi_2Te_3 and Bi_7Te_3. The experimental information from Mao [157] is shown for completeness and not expected to match in the gray region. Compounds that are of particular interest in the gray shaded region can be modeled using the equations analogous to 6.12 and 6.13. The temperature dependent term can be used to describe its melting point once they have been determined. Modeling the homologous series this way is a much more physically accurate description than the solid solution description used in previous models. This should lead to more accurate extrapolation into the ternaries at the cost of a cleaner looking binary.

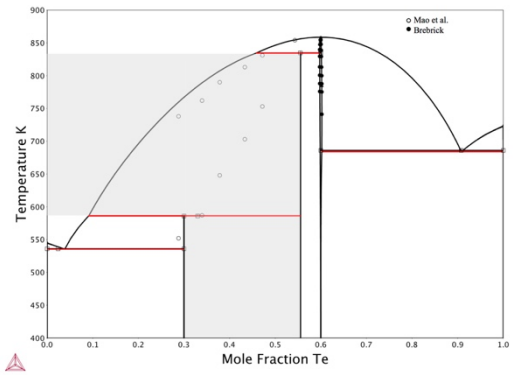

Figure 6.2: Calculated Bi-Te phase diagram and experimental information[147, 157]. The gray shaded regions is considered metastable.

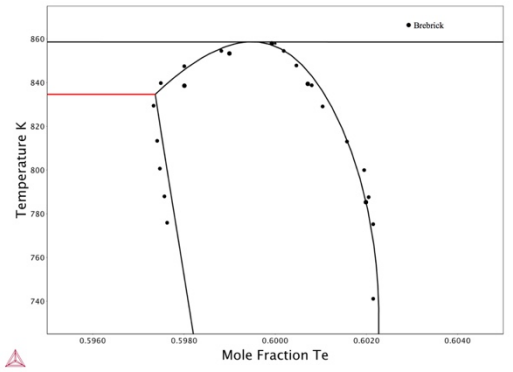

Figure 6.3: Enlarged region of homogeneity for Bi_2Te_3 and experimental data [147]

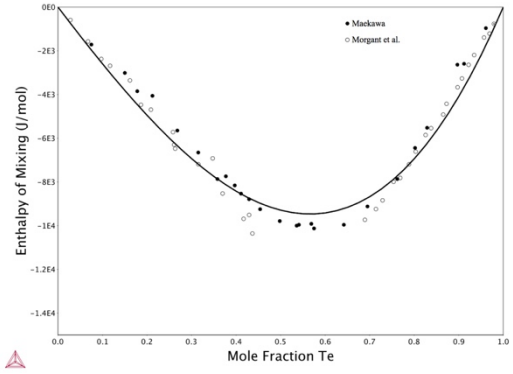

Figure 6.4: Enthalpy of mixing for Bi-Te liquid and experimental information [168] [169]

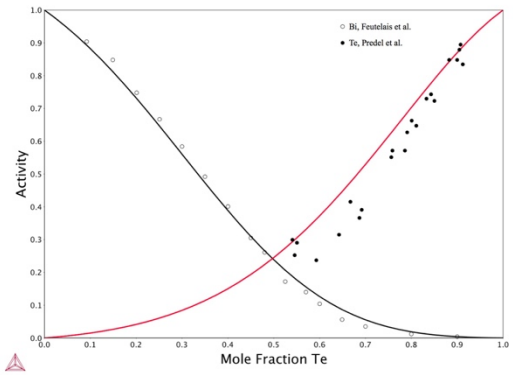

Figure 6.5: The activity of Bi and Te at 863 K and 1081 K, respectively. Experimental information [166, 167].

Table 6.1: Optimized parameters for the Bi-Te system

Phase	Optimized Parameter (J/mol)
Liquid (Bi,Te)	${}^{0}L^{l}_{Bi,Te} = -37{,}165 + 13.36T$ ${}^{1}L^{l}_{Bi,Te} = 10{,}379 - 6.93T$
Bi_2Te_3 $(Bi,Te)_2(Te,Bi)_1(Te)_2$	$G^{Bi_2Te_3}_{Bi:Te:Te} = -143{,}157 + 534.35T - 111.65T\ln(T) - .0249T^2 + 2.626\times10^{-10}\times T^3 + 85{,}400T^{-1}$ $G^{Bi_2Te_3}_{Te:Te:Te} = 20{,}008 + 5\ {}^{0}G^{Hex}_{Te}$ $G^{Bi_2Te_3}_{Bi:Bi:Te} = -12{,}967 + 3\ {}^{0}G^{Rhom}_{Bi} + 2\ {}^{0}G^{Hex}_{Te}$ $G^{Bi_2Te_3}_{Te:Bi:Te} = -20{,}925 + {}^{0}G^{Rhom}_{Bi} + 4\ {}^{0}G^{Hex}_{Te}$ ${}^{0}L^{Bi_2Te_3}_{Bi,Te:Te:Te} = 113{,}269 - 107.6T$ ${}^{0}L^{Bi_2Te_3}_{Bi:Bi,Te:Te} = -36{,}389$
Bi_4Te_5 $(Bi)_4(Te)_5$	$G^{Bi_4Te_5}_{Bi:Te} = \frac{5}{3}G^{Bi_2Te_3} + \frac{2}{3}\ {}^{0}G^{Rhom}_{Bi} - 12.01T$
Bi_7Te_3 $(Bi)_7(Te)_3$	$G^{Bi_7Te_3}_{Bi:Te} = G^{Bi_2Te_3} + 5\ {}^{0}G^{Rhom}_{Bi} - 17.58T$

6.4.2 Bi-Se

The final optimized parameters for the Bi-Se system are summarized in Table 6.2. The enthalpies of mixing and activity of Bi-Se melts and experimental information are shown in Figure 6.8 and Figure 6.9, respectively. The sharp enthalpy of mixing at 60 at% Se necessitates an associate model with Bi_2Se_3 associates. A reasonable agreement between the experimental

information and model are shown. The calculated and experimental heat capacity of Bi_2Se_3 is shown in Figure 6.10. In previous assessments, this compound was modeled using the Neumann-Kopp approximation, which uses a stoichiometric combination of the constituents, in this case rhombohedral Bi and hexagonal Se, to describe the heat capacity. This approximation is unnecessary as the coefficients c through f in equation 6.5 can be fit to experimental data. The final phase diagram and experimental information are shown in Figure 6.6. Despite the gray region being metastable, there is still reasonable agreement with the experimental phase diagram. This implies that the experimental data may not be at actual equilibrium, which is difficult to obtain in these systems [154].

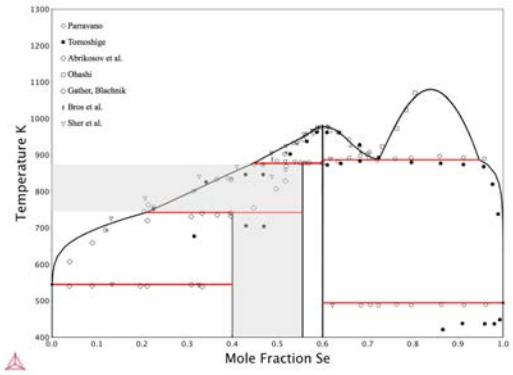

Figure 6.6: Calculated Bi-Se phase diagram and experimental information [172] [173] [174] [175] [176] [177] [178] . The gray shaded regions is considered metastable.

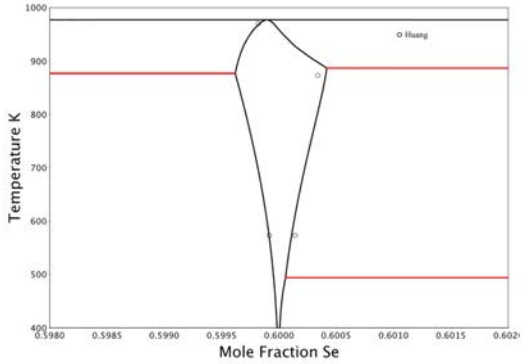

Figure 6.7: Enlarged region of homogeneity for Bi_2Se_3 and experimental data [179]

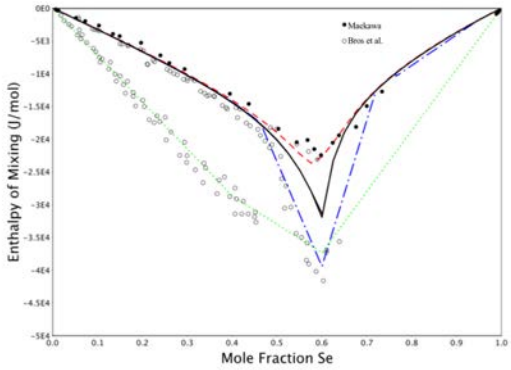

Figure 6.8: Enthalpy of mixing for Bi-Se liquid and experimental information [183] [177]. Four temperatures are shown at 560 K (green), 828 K (black), 888 K (blue), and 998 K (red).

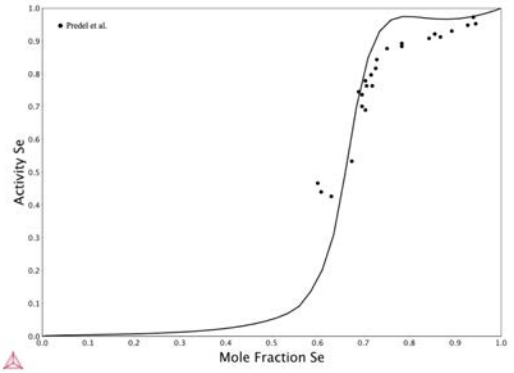

Figure 6.9: Activity of Se at 860 K and experimental information [182]

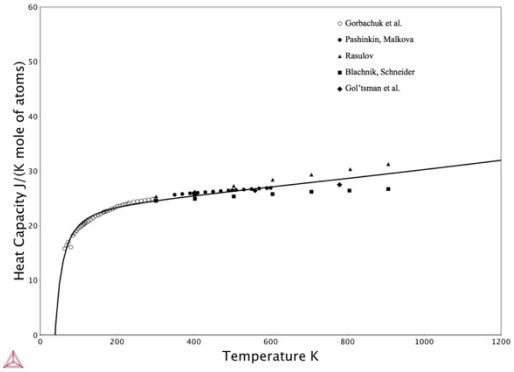

Figure 6.10: Heat capacity of Bi2Se3 and experimental information [202] [184] [185] [186] [187].

Table 6.2: Optimized parameters for the Bi-Se system

Phase	Optimized Parameter (J/mol)
Liquid (Bi,Bi_2Se_3,Se)	$G^{l}_{Bi_2Se_3} = -159{,}856 + 70.93T + 2\ {}^{0}G^{l}_{Bi} + 3\ {}^{0}G^{l}_{Se}$

	${}^{0}L^{l}_{Bi,Bi_2Se_3} = 77{,}519 - 89.11T$ ${}^{1}L^{l}_{Bi,Bi_2Se_3} = -10{,}735$ ${}^{2}L^{l}_{Bi,Bi_2Se_3} = -4{,}674$ ${}^{0}L^{l}_{Bi_2Se_3,Se} = 115{,}914 - 115.90T$ ${}^{1}L^{l}_{Bi_2Se_3,Se} = 43{,}134 - 44.93T$ ${}^{2}L^{l}_{Bi_2Se_3,Se} = 16{,}257$
Bi_2Se_3 $(Bi,Se)_2(Se,Va)_1(Se)_2$	$G^{Bi_2Se_3}_{Bi:Se:Se} = -175{,}9893 + 533.34T - 113.171T\ln(T) - .0189T^2 + 84{,}813T^{-1}$ $G^{Bi_2Se_3}_{Se:Se:Se} = 82{,}293 + 5\ {}^{0}G^{Hex}_{Se}$ $G^{Bi_2Se_3}_{Se:Va:Se} = 82{,}293 + 4\ {}^{0}G^{Hex}_{Se} + 2.3RT$ $G^{Bi_2Se_3}_{Bi:Va:Se} = 2.3RT + 2\ {}^{0}G^{Rhom}_{Bi} + 2\ {}^{0}G^{Hex}_{Se}$ ${}^{0}L^{Bi_2Se_3}_{Bi,Se:Se:Se} = -9{,}569$ ${}^{0}L^{Bi_2Se_3}_{Bi:Se,Va:Se} = -75{,}915$
Bi_4Se_5 $(Bi)_4(Se)_5$	$G^{Bi_4Se_5}_{Bi:Se} = \frac{5}{3}G^{Bi_2Se_3} + \frac{2}{3}\ {}^{0}G^{Rhom}_{Bi} - 19.39T$
Bi_3Se_2 $(Bi)_3(Se)_2$	$G^{Bi_3Se_2}_{Bi:Se} = \frac{2}{3}G^{Bi_2Se_3} + \frac{5}{3}\ {}^{0}G^{Rhom}_{Bi} - 13.55T$

6.4.3 Sb-Te

The final optimized parameters for the Sb-Te system are summarized in Table 6.3. The enthalpies of mixing and activity of Sb-Te melts and experimental information are shown in Figure 6.13 and Figure 6.14. In contrast to previous assessments [191] [159], which used either an associate or ionic liquid model, a satisfactory agreement with the experimental data is achieved with a simple substitutional model. Although the system exhibits a minimum near 60 at% Te, the enthalpy of mixing is not nearly as sharp as Bi-Se and is similar in shape to Bi-Te, which also did not necessitate a more complicated model. In order to accurately describe the liquid, a third order Redlich-Kister polynomial was necessary; however the number of fitting parameters is reduced from 10 in previous assessments[159] to 8 in this work. The phase diagram and experimental information are shown in Figure 6.11. Similar to the Bi-Se system, there is reasonable agreement

even in the metastable region, again implying that full equilibrium may not have been achieved in the experimental studies.

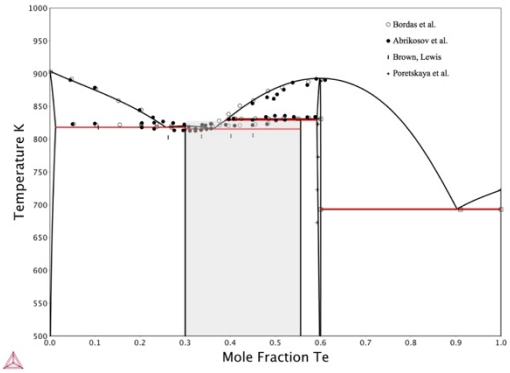

Figure 6.11: Calculated Sb-Te phase diagram and experimental information [203] [190] [204] [192]

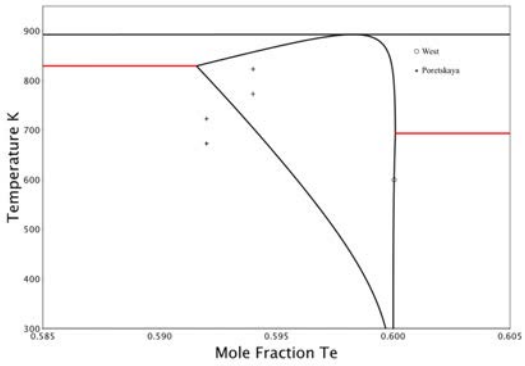

Figure 6.12: Enlarged region of homogeneity for Sb_2Te_3 and experimental data [192] [164]

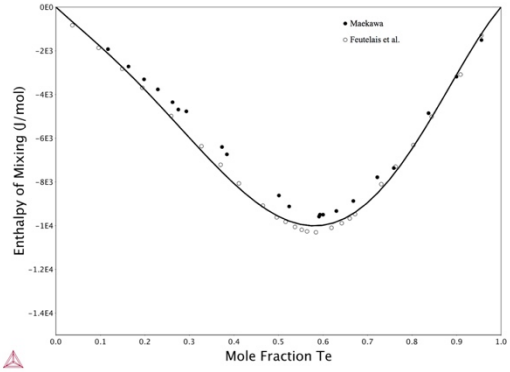

Figure 6.13: Enthalpy of mixing for Sb-Te liquid and experimental information [194] [195]

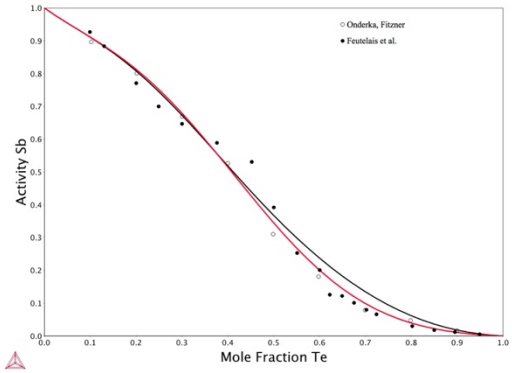

Figure 6.14: Activity of Sb at 1023 K (black) and 911 K (red) and experimental information [196] [194]

Table 6.3: Optimized parameters for the Sb-Te system

Phase	Optimized Parameter (J/mol)
Liquid (Sb,Te)	${}^{0}L^{l}_{Sb,Te} = -38{,}309 + 22.61T$ ${}^{1}L^{l}_{Sb,Te} = 20{,}580 - 15.52T$ ${}^{2}L^{l}_{Sb,Te} = 17{,}284 - 16.10T$ ${}^{3}L^{l}_{Sb,Te} = -18{,}182 + 20.33T$
Rhombohedral A7 (Sb,Te)	$G^{Rhom}_{Sb} = {}^{0}G^{Rhom}_{Sb}$ $G^{Rhom}_{Te} = 4073 + {}^{0}G^{Hex}_{Te}$ ${}^{0}L^{Rhomb}_{Sb,Te} = 2{,}682$
Sb_2Te_3 $(Sb,Va)_2(Te,Sb)_1(Te)_2$	$G^{Sb_2Te_3}_{Sb:Te:Te} = -94{,}087 + 529.11T - 112.8765T\ln(T) - .02436T^2 + 1.81228\times10^{-6}\times T^3 + 64{,}655T^{-1}$ $G^{Sb_2Te_3}_{Sb:Sb:Te} = 1185 + 3\ {}^{0}G^{Rhom}_{Sb} + 2\ {}^{0}G^{Hex}_{Te}$ $G^{Sb_2Te_3}_{Va:Sb:Te} = 1185 + {}^{0}G^{Rhom}_{Sb} + 2\ {}^{0}G^{Hex}_{Te} + 4.6RT$ $G^{Sb_2Te_3}_{Va:Te:Te} = 4.6RT + 3\ {}^{0}G^{Hex}_{Te}$ ${}^{0}L^{Sb_2Te_3}_{Sb,Va:Te:Te} = 64{,}287$ ${}^{0}L^{Sb_2Te_3}_{Sb:Sb,Te:Te} = -26{,}629$
Sb_4Te_5 $(Sb)_4(Te)_5$	$G^{Sb_4Te_5}_{Sb:Te} = \frac{5}{3}G^{Sb_2Te_3} + \frac{2}{3}\ {}^{0}G^{Rhom}_{Sb} - 2.91T$
Sb_7Te_3 $(Sb)_7(Te)_3$	$G^{Sb_7Te_3}_{Sb:Te} = G^{Sb_2Te_3} + 5\ {}^{0}G^{Rhom}_{Sb} - 11.56T$

6.4.4 Homologous Compounds and Defect Modeling

The enthalpies of formation of the intermetallics are shown in Figure 6.15 along with the reported values in the literature. The experimental information and calculated data are in good agreement for the compound A_2Q_3. Only data on the A_2Q_3 compound have been reported, but as stated earlier, the other intermetallics should lie on the convex hull between A and A_2Q_3. Only introducing a temperature dependent fitting term and describing the other compounds as a stoichiometric mixture of A and A_2Q_3 forces their enthalpies of formation on the convex hull as depicted by the closed circles in Figure 6.15.

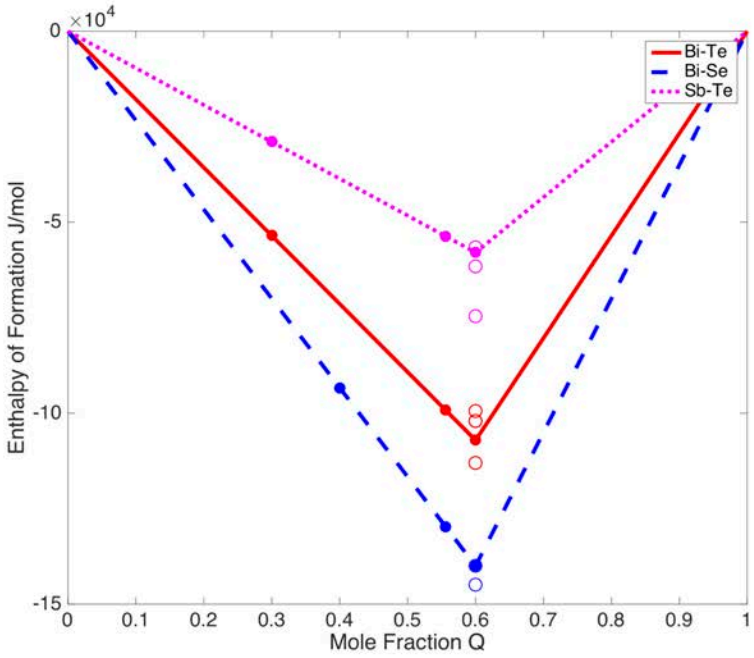

Figure 6.15: Formation energies of the intermetallics in Bi-Te (solid red), Bi-Se (dashed blue), and Sb-Te (dotted magenta). Closed circles represent the calculated formation energy and open circles are published values for Bi_2Te_3[153, 198, 205],Bi_2Se_3[155, 205], and Sb_2Te_3[197, 199, 206].

The 3SL model used to describe the A_2Q_3 compounds enables the determination of formation energies at a given temperature and equilibrium. The calculated formation energies and dominant defects are shown in Table 6.4. The interaction parameters for Bi_2Te_3 were fit using the solubility data from Brebrick[147], the parameters for Bi_2Se_3 were fit using the carrier

concentration reported by Hunag et al. [179], and the parameters for Sb_2Te_3 were determined using the data from Poretskaya[192]and West[164]. In each case only the dominant defects are modeled. This is done as it is very difficult to differentiate the defects when carrier concentrations are measured. In addition, first-principles calculations show differences in formation energies that result in orders of magnitude differences in the concentration of defects[164], which further strengthen this assumption. According to the electronegativity and covalent radius model, we would expect the formation energy of A antisite defects in A-rich growth conditions to increase from Sb-Te, to Bi-Te, then Bi-Se[146]. According to Table 6.4 this trend is adhered to. Even though Bi_{Se} is not modeled, the defect formation energy has to be higher than the dominant defect, Va_{Se}, which is already greater than Bi_{Te} therefore guaranteeing the trend holds. Alternatively, increasing this difference will increase the likelihood of a Q vacancy and we would expect the formation energy to increase from Bi-Se to Bi-Te, then Sb-Te[146]. The only Q vacancy modeled is in the Bi-Se system, as the other Q vacancies were dominated by other defects, so our model is in qualitative agreement with this observation again.

Table 6.4: Calculated defect formation energies in various growth conditions determined by the 3SL model

	A-Rich		Q-Rich	
Compound	Defect	Formation Energy (kJ/mol)	Defect	Formation Energy (kJ/mol)
Bi_2Te_3	Bi_{Te}^{-1}	23.8	Te_{Bi}^{+1}	48.7
Bi_2Se_3	Va_{Se}^{2+}	25.5	Se_{Bi}^{+1}	36.3
Sb_2Te_3	Sb_{Te}^{-1}	15.9	Va_{Sb}^{-1}	37.9

In all three compounds, the congruent melting point near the A_2Q_3 composition is displaced towards the A-rich side as is shown in Table 6.5 along with the experimental data[207]. This

ensures that a material formed from a melt of nominal A_2Q_3 composition will vary from A-rich to Q-rich along the solidification direction. This can have dramatic consequences for the carrier concentrations which are affected by the native defects. The challenge of maintaining a controlled composition in these materials is further compounded by the relatively high vapor pressures of selenium and tellurium[208] that can lead to unintended chalcogen losses. Producing uniform solid compositions from a melt requires maintaining a constant composition in the liquid phase at the growth interface. Methods used to achieve this include zone leveling[209] and the traveling heater method[210].

The stoichiometry of A_2Q_3 solids can be manipulated by annealing samples under conditions slightly outside the solidus and rich in either the A or Q species [211]. This fixes the equilibrium composition at the solidus for a given temperature providing more consistent and predictable carrier concentrations. For example, solid samples can be annealed along with either A-rich or Q-rich powder of the compound at a temperature corresponding to the desired solidus composition. Another example would be pressing and sintering powders having an excess of one element [212]. In both of these cases, the stoichiometry of the material, and thus the carrier concentration, is controlled by the temperature of the anneal. If the native defect concentrations can be made predictable, further manipulation of the carrier concentration can be accomplished via extrinsic doping [213].

Table 6.5: Calculated congruent melting point compositions for compounds A_2Q_3 compared to experiments

Compound	Calculated Composition for Congruent Melting Point Atomic Percent Q	Experimentally Determined Composition for Congruent Atomic Percent Q [207]
Bi_2Te_3	59.95	59.935
Bi_2Se_3	59.99	59.98
Sb_2Te_3	59.83	59.6

Since precise carrier concentration tuning, which is dictated by the annealing temperature, is imperative to fully optimize these materials, it is important to understand the changes in the solidus with respect to temperature. Fluctuations or imprecision in furnace temperatures could cause the equilibrium carrier concentration to drastically vary. Annealing the material at a temperature where the slope of the solidus is near a minimum would mitigate this issue as temperature changes would not affect the carrier concentration as much. Figure 6.16 through Figure 6.18 show the magnitude of the solidus slope with temperature on the a) A-rich and b) Q-rich side. The drastic changes in slope occur invariant points and should therefore should be avoided as processing temepratures.

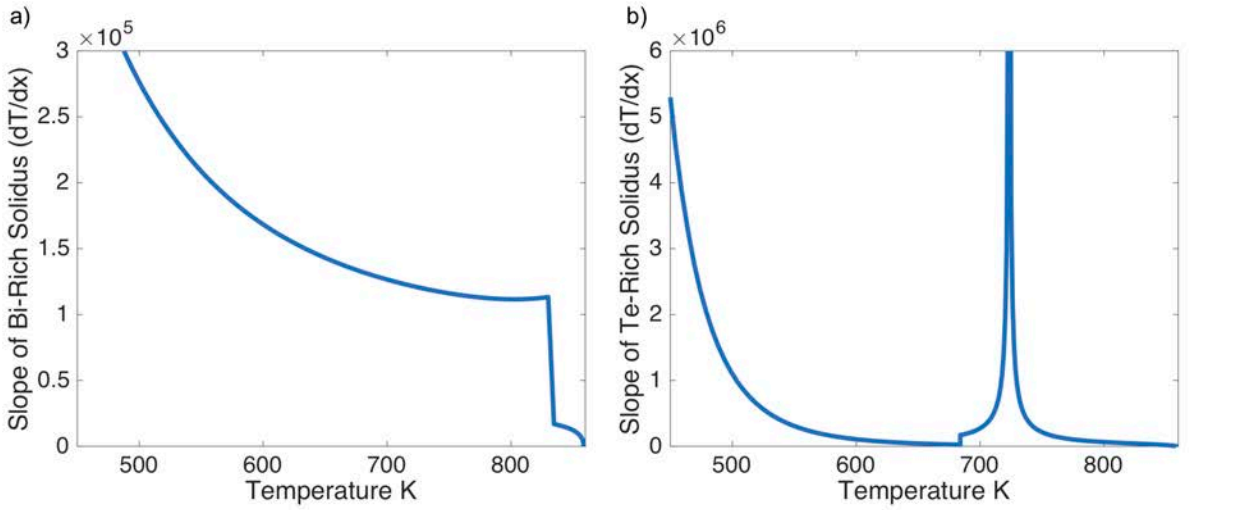

Figure 6.16: Slope of Bi_2Te_3 solidus line a) Bi-rich and b) Te-rich regions

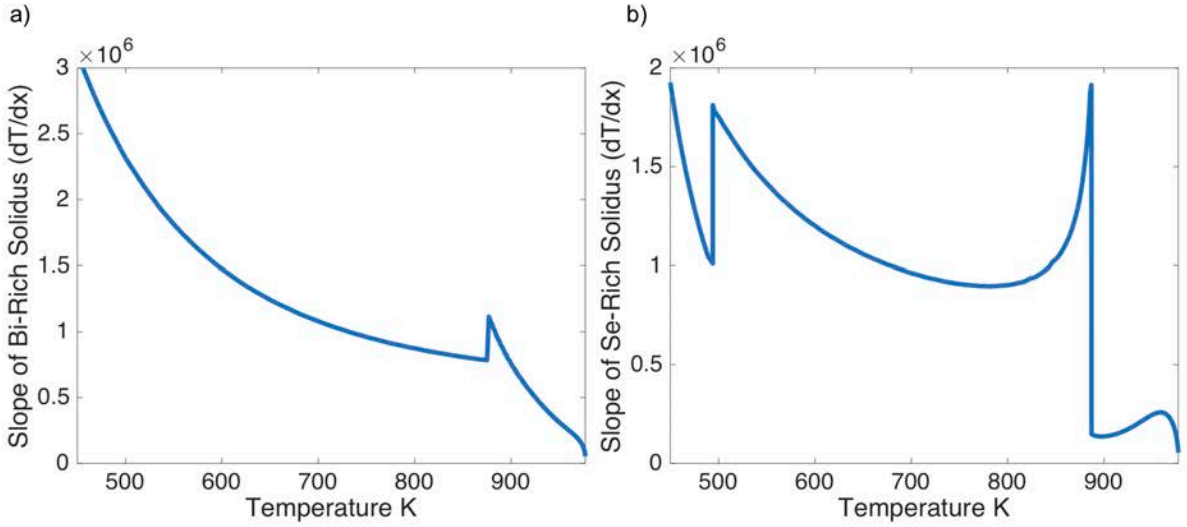

Figure 6.17: Slope of Bi_2Se_3 solidus line a) Bi-rich and b) Se-rich regions

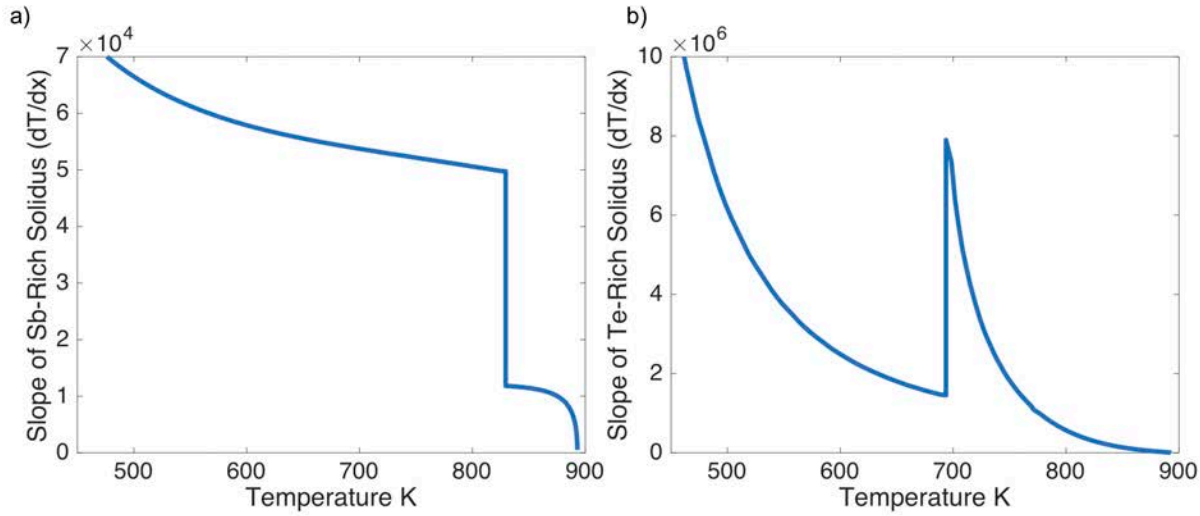

Figure 6.18: Slope of Sb_2Te_3 solidus line a) Sb-rich and b) Te-rich regions

6.5 Conclusions

Thermodynamic assessments of the Bi-Te, Bi-Se, and Sb-Te systems have been performed. Each system contains an infinite series of homologous compounds between the compounds A and A_2Q_3. Previous assessments have chosen to model these compounds as a solution phase with random mixing. First-principles calculations have shown this to be physically

inaccurate. This work assumes a metastable region between the experimentally found homologous compounds and models the compounds as stoichiometric mixtures of A and A_2Q_3. In addition, the defects in A_2Q_3 have been modeled based on experimental and first-principles calculations. The formation energy of the defects can be determined by the careful consideration of 3SL end-members and interaction parameters. The calculated formation energies agree with the electronegativity and covalent radius model for comparing the antisite and vacancy formation energies of the different systems.

7. Future Work for Designing Thermoelectrics

7.1 Introduction

The models presented thus far have numerous applications for designing thermoelectric materials. The thermodynamic phase diagrams allow for determining the equilibrium solubility of elements in a given a matrix as well as the equilibrium volume fraction of precipitates. The soluble elements can either contribute as point defects for scattering phonons[214], create *p* or *n-type* charge carriers[108], or alter the band structure of the host material for enhanced transport properties[82]. The precipitates primary function is to lower the thermal conductivity by scattering phonons of wavelengths between those affected by the smaller point defects and larger grain boundaries. However, careful consideration should be made for determining the second phase to ensure transport properties are not adversely affected as well, which can be achieved through band alignment of the primary and secondary phases[12].

The kinetic descriptions, coupled with the thermodynamics, can be used to determine the processing time and temperature necessary to achieve a desired microstructure. Therefore, it is important to first determine a target microstructure that optimizes the thermoelectric properties. The Debye-Callaway model, which uses microstructural inputs to determine the lattice thermal conductivity, will be used to calculate the optimal radius for a given volume fraction of precipitates. The transport properties can be modeled through a single parabolic band (SPB) model, and lastly, PrecipiCalc can be used to model the nucleation and growth of the second phase precipitates.

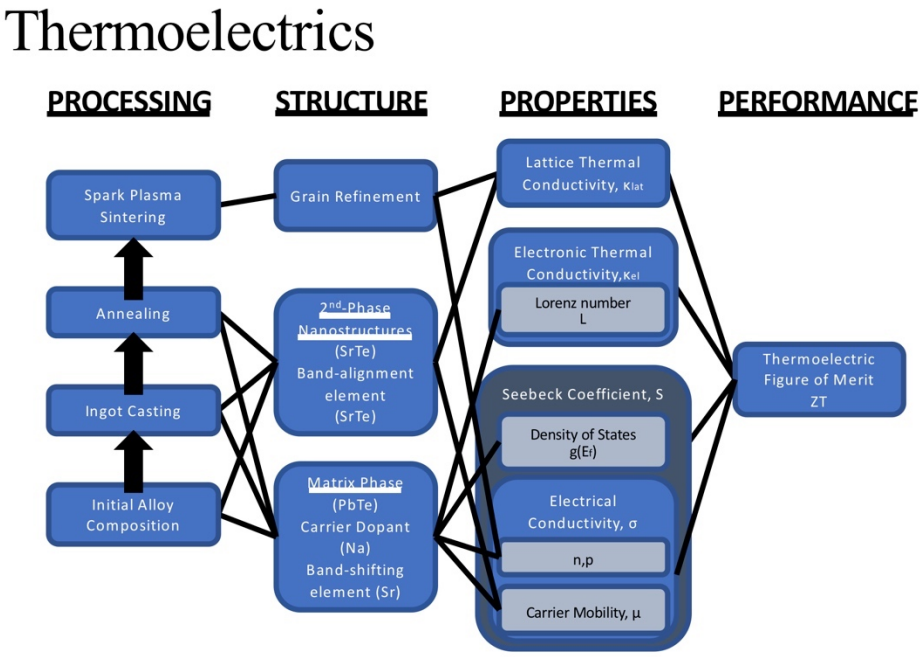

Figure 7.1: System Design chart for a (Pb,Na,Sr)(Te,Se) thermoelectric material used in MAT-SCI 390 class.

This optimization process has been used as a 390 project for three quarters and a representative system design chart is shown in Figure 7.1 for a (Pb,Na,Sr)(Te,Se) system. The system design chart shows the relationship between the initial alloy composition and annealing temperature dictating the second phase nanostructure and matrix phase composition. These in turn dictate the Seebeck coefficient, electrical conductivity, and thermal conductivity, which are used for calculating *zT*. An overview of the models, adjustable parameters, and tools used in this project along with the work flow is shown in the flow chart in Figure 7.2 for the (Pb,Na,Sr)(Te,Se) system. For this chapter, a PbTe matrix phase alloyed with PbS to produce precipitates and Na to introduce holes into the system will be used. Although there exists better performing thermoelectric systems [12, 215], such as the one studied in 390, the Na-doped PbTe-PbS system has extensive literature

data as well as experimental data that was outlined in previous chapters which can be used to calibrate the models. This outlined methodology can be applied for other systems.

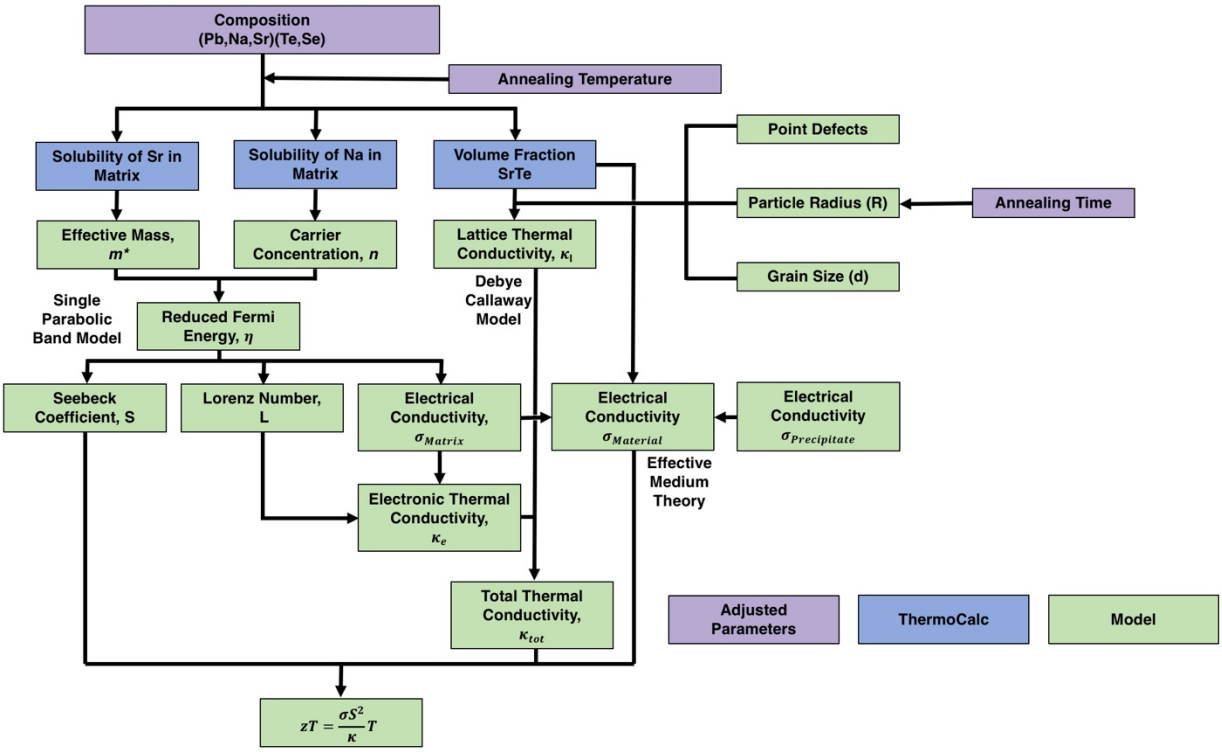

Figure 7.2: Flow chart of adjustable parameters and models used for designing a thermoelectric material. This flow chart is representative for a (Pb,Na,Sr)(Te,Se) material but can be generalized to other systems.

7.2 Lattice Thermal Conductivity

The Debye-Callaway model for thermal conductivity is extensively used in the field to study the thermal conductivity of Pb-chalcogenide thermoelectrics[100, 107] [12, 214, 216]. The thermal conductivity is calculated as[217]

$$\kappa_l = \frac{k_B}{2\pi^2 v}\left(\frac{k_B T}{\hbar}\right)^3 \int_0^{\theta_D/T} \tau_c(x) \frac{x^4 e^x}{(e^x-1)^2} dx \quad (7.1)$$

where v is the average phonon-group velocity, θ_D the Debye temperature, τ_c the relaxation time, and x is a function of the phonon frequency ω, $\hbar\omega/k_B T$. The relaxation time is determined via

Matthiessen's rule where the total relaxation time is determined by the sum of the inverse of individual scattering processes:

$$\frac{1}{\tau_c} = \frac{1}{\tau_U} + \frac{1}{\tau_N} + \frac{1}{\tau_{ss}} + \frac{1}{\tau_{np}} + \frac{1}{\tau_{gb}} \quad (7.2)$$

where τ_U, τ_N, τ_{ss}, τ_{np}, and τ_{gb} are the scattering processes from Umklapp processes, normal processes, solid solution defects, nanoprecipitates, and grain boundaries, respectively. The normal and Umklapp processes are intrinsic to the material. Conversely, the scattering due to solid solution, nanoprecipitates, and grain boundaries can be tuned and optimized to lower the thermal conductivity.

The scattering due to precipitates is split into short and long wavelength scattering regimes defined as[218]

$$\tau_{np}^{-1} = v(\sigma_s^{-1} + \sigma_l^{-1})^{-1} V_p \quad (7.3)$$

$$\sigma_s = 2\pi R^2 \quad (7.4)$$

$$\sigma_l = \pi R^2 \frac{4}{9} \left(\frac{\Delta D}{D}\right)^2 \left(\frac{\omega R}{v}\right)^4 (7.5)$$

where R, V_p, ΔD, and D are the radius of the nanoprecipitate, number density of the nanoparticle, the difference in density between the matrix and nanoparticle, and the matrix density. For a fixed volume fraction, the nanoprecipitate radius and number density are inversely related and there exists a fixed radius that minimizes the thermal conductivity. A calculation of the lattice thermal conductivity of $PbTe_{0.88}S_{0.12}$ at 300 K for various radii is shown in Figure 7.3. A minimum of the thermal conductivity is evident for a radius of average size 2.5 nm.

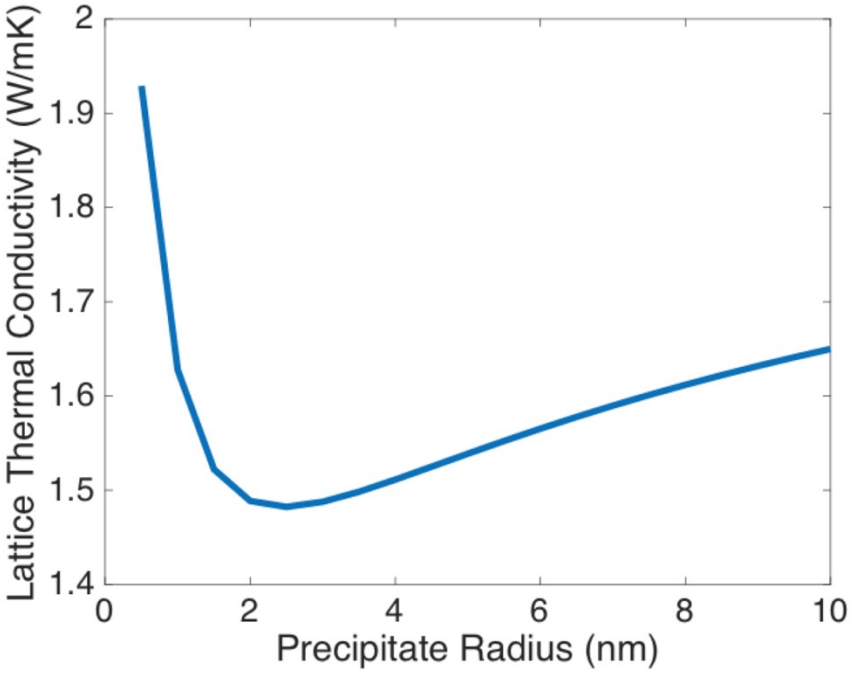

Figure 7.3: Thermal conductivity of PbTe with 0.12 volume fraction PbS at 300 K. According to the Debye-Callaway model there is an optimal particle radius, which correlates to a minimum in the lattice thermal conductivity.

The scattering due to point defects is dictated by strain (Γ_S) and mass fluctuations (Γ_M) and is given as[219]

$$\tau_{ss}^{-1} = \frac{\omega^4 \delta^3}{4\pi v^3}(\Gamma_M + \Gamma_S) \quad (7.6)$$

where δ is the radius of the defect atom. The mass fluctuations are calculated as a sum over the sublattices *i* the defects occupy:

$$\Gamma_M = \frac{\Sigma_{i=1}^{n} c_i \left(\frac{\langle M_i \rangle}{M^*}\right)^2 f_i^1 f_i^2 \left(\frac{M_i^1 - M_i^2}{\langle M_i \rangle}\right)^2}{\Sigma_{i=1}^{n} c_i} \quad (7.7)$$

where c_i is the degeneracy of the sublattice *i*, f_i^j are the fractional occupation for component *j*, M_i^j the atomic mass of component *j*, $\langle M_i \rangle$ the average atomic mass of components on the sublattice,

and M^* is the average atomic mass of the compound. An analogous description for the fluctuations due to strain is given as:

$$\Gamma_S = \frac{\sum_{i=1}^{n} c_i \left(\frac{\langle M_i \rangle}{M^*}\right)^2 f_i^1 f_i^2 \varepsilon \left(\frac{r_i^1 - r_i^2}{\langle r_i \rangle}\right)^2}{\sum_{i=1}^{n} c_i} \quad (7.8)$$

where r_i^j is the radius of component j, and ε is a phenomenological parameter of PbTe. The fractional occupancies are determined from the equilibrium phase diagram and the rest of the parameters are element constants.

The scattering due to grain boundaries is frequency independent and simply a function of the average grain size. It is determined as[220]

$$\tau_{gb}^{-1} = \frac{v}{d} \quad (7.9)$$

where d is the average grain size. Grain boundaries play a particularly dominant role in scattering wavelengths of very small frequency, or large wavelength, that are not accessible by other scattering mechanisms. Typical grain boundaries in PbTe based systems in the literature are approximately 2 μm in size[12, 216, 221]; however, grain sizes of 0.7 μm were achievable in PbTe by decreasing the sintering time and temperature to 613 K and 1 min, although at the expense of lowering the relative density of 95.8% from 99.7% seen at more conventional processing routes[222].

The scattering time for the various processes as a function of phonon frequency is shown in Figure 7.4 at 300 K. The model material consists of .06 volume fraction PbS with a .05 site occupancy of S on the PbTe site. As discussed earlier, the grain boundary scattering is effective at the low frequency range and the other processes take over at larger frequencies. Precipitate and

solid solution scattering are not as effective in this system due to the small density different in PbTe and PbS.

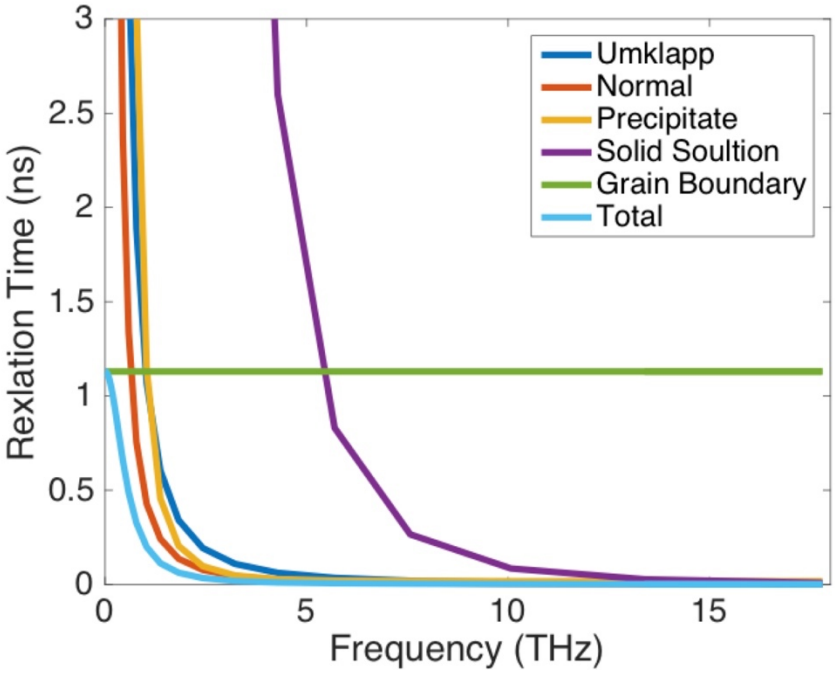

Figure 7.4: Relaxation time as a function of phonon frequency for various scattering mechanisms discussed at 300 K.

The Debye-Callaway model has been used to model the thermal conductivity of a $Pb_{.98}Te_{.88}S_{.12}$-$Na_{.02}$ as a function of temperature to compare with the literature and is shown in Figure 7.5. Due to the lack of processing details, such as annealing temperature or quench rate, it is difficult to compare the results. The calculations have assumed that the equilibrium state at 823 K, a typical annealing temperature for these materials[12], has been retained to determine the volume fraction of precipitates and site fraction of alloying elements, and a precipitate radius of 2 nm was assumed. The results agree fairly well with the data taken from Yin[216] and Girard[99], with deviations at higher temperature likely arising from bipolar diffusion[223], which is not currently taken into account in the model. Another calculation with a more refined grain structure of 0.7 μm is also shown to illustrate the effect of grain refinement, which is possible as mentioned

before. Other scattering mechanisms, such as strain contributions, could also further decrease the lattice thermal conductivity[214].

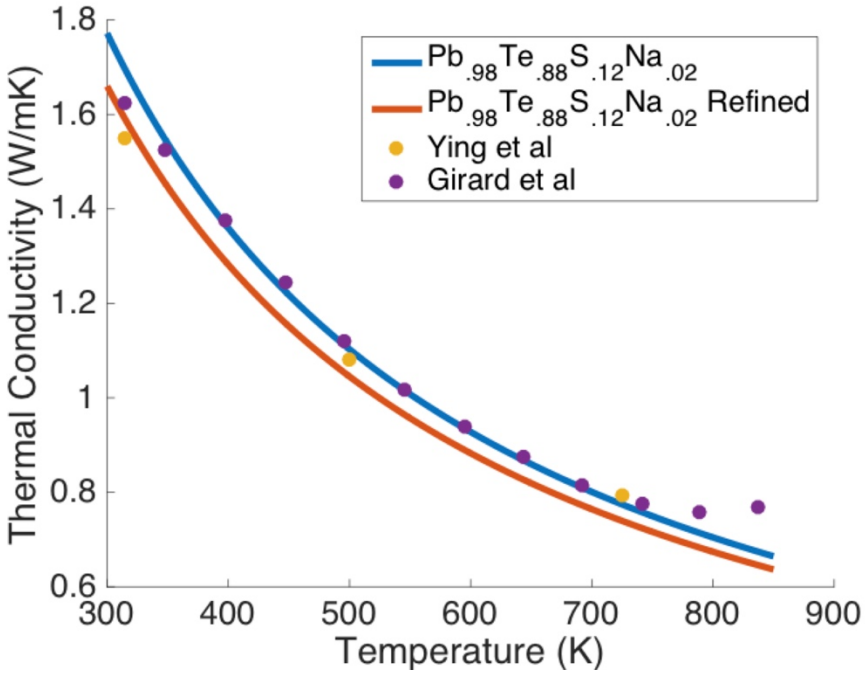

Figure 7.5: Thermal conductivity of $Pb_{.98}Te_{.88}S_{.12}$-$Na_{.02}$ compared with the literature[99, 216]. The effect of grain refinement to a size of 0.7 μm is also shown as a possible way to lower the thermal conductivity.

7.3 Transport Properties

The Seebeck coefficient and electrical conductivity can be modeled through the single parabolic band (SPB) model. Although it is known that PbTe exhibits two valence bands, known as the L and Σ bands, that contribute holes, the SPB model has been used extensively for modeling this material[103, 215]. For more accurate modelling a single Kane band (SKB) or two Kane band model, can be used[11, 82].

In the SPB model, the Hall carrier concentration is defined as[224]

$$n_H = 4\pi \left(\frac{2m^* k_B T}{h^2}\right)^{\frac{3}{2}} F_{1/2} \quad (7.10)$$

Where m^* is equal to the effective mass and F_j is a Fermi integral using the conventional definition[225]:

$$F_j(\eta) = \int_0^\infty \frac{x^j dx}{1+\exp(x-\eta)} \quad (7.11)$$

where η is the reduced chemical potential. Under the assumption that acoustic phonon scattering is the dominant scattering mechanism, the Seebeck coefficient is calculated as

$$S = \frac{k}{e}\left(\frac{2F_1(\eta)}{F_0(\eta)} - \eta\right) \quad (7.12)$$

Generally, the effective mass in the carrier concentration is used as a fitting parameter to fit the change in Seebeck coefficient as a function of carrier concentration. A reduced fermi energy is determined that correlates to a specific carrier concentration. With a known reduced fermi energy an electrical conductivity can be determined by

$$\sigma = \frac{8\pi e^2}{3m^* h^3}(2m^* kT)^{\frac{3}{2}}\tau_0 F_0(\eta) \quad (7.13)$$

where τ_0 is an energy independent term of the relaxation time. The electronic component of the thermal conductivity can be determined from the Weidemann-Franz relation

$$\kappa_e = L\sigma T \quad (7.14)$$

where L is the Lorenz number calculated as

$$L = \left(\frac{k}{e}\right)^2 \frac{3F_0(\eta)F_2(\eta) - 4F_1(\eta)^2}{F_0(\eta)^2} \quad (7.15)$$

The electronic component of the thermal conductivity can be added to the lattice component calculated in Section 7.2 to determine the total thermal conductivity.

The reduced Fermi energy, η, appears in all the transport equations and therefore can be used to determine what the optimal carrier concentration is in order to increase thermoelectric efficiency. The Seebeck coefficient and electrical conductivity are shown in Figure 7.6(a) for a PbTe-2%Na doped material with an effective mass of $0.82m_0$ based off of experimental data at 300 K[12]. The power factor is given in Figure 7.6(b) where a peak is shown at 2.5 x 10^{19} holes/cm^3, which is above the solubility limit of Na in PbTe at this temperature, but is achievable at higher temperatures as evident in Section 4.3.5. It has been found that carrier concentrations on the order of 1 x 10^{20} holes/cm^3 are necessary in order to optimize the transport properties[114], which is reflected by a shifting peak in the power factor at higher temperatures. This can be modeled through a temperature dependence on the effective mass[11]. This model can therefore be used to determine the doping level necessary for peak zT performance as well as determining the doping level for a specific operating temperature.

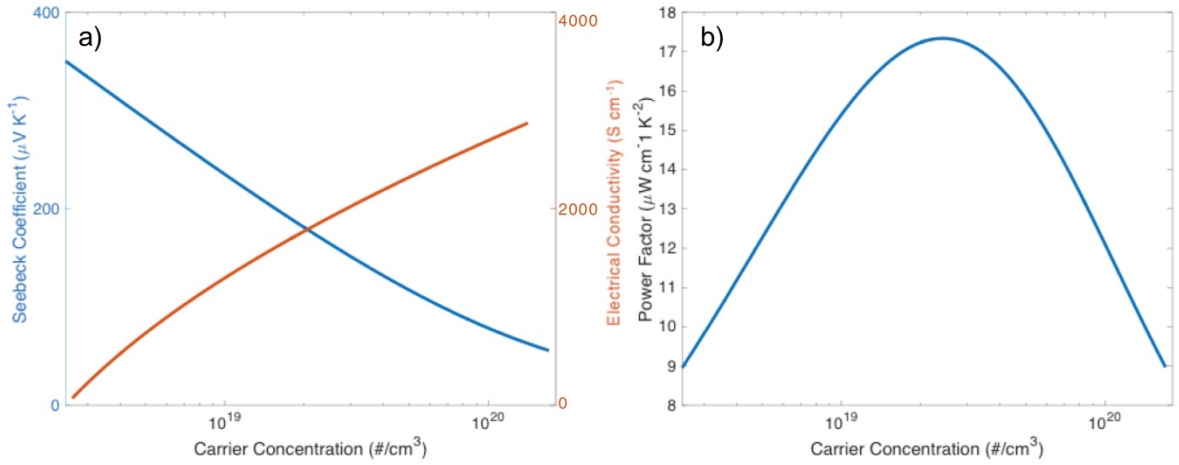

Figure 7.6: a) Seebeck Coefficient (blue) and electrical conductivity (red) at 300 K as a function of carrier concentration according to the single parabolic band model and b) power factor as a function of carrier concentration. According to the single parabolic band model there is an optimal carrier concentration that maximizes power factor.

7.4 PrecipiCalc Modeling

In order to get the desired microstructure an annealing time needs to be determined. The nucleation and growth process involves many inputs from the thermodynamics and kinetics, which have been previously assessed, as well as the interfacial energy, which is difficult to experimentally obtain. In addition, more complex nucleation processes such as those formed via heterogenous nucleation can further complicate the modeling. The PrecipiCalc modeling software is a flexible tool that is able to use such inputs to model the nucleation in complex alloys[226]. PrecipiCalc is based on the Kampann-Wagner solution to the Langer-Schwartz algorithm for nucleation and growth and has proven successful in modeling nickel-base superalloys[227, 228]. The major assumptions involved in PrecipiCalc modeling are that the precipitation is diffusion-controlled, the precipitates interact through a mean field composition, the particles are spherical, and that no hard impingement occurs between the particles[226].

Unfortunately, there are limited studies on the exact nucleation and growth process in PbTe-PbS systems. Often times, the electrical or thermal properties are of interest and the processing conditions for which the material has gone through is not tightly controlled. This makes calibration of the PrecipiCalc software quite difficult for which physical parameters such as particle size, number density, and volume fraction are necessary. A recent paper studied the microstructural changes of the PbTe-PbS system as a function of PbS composition [216]. The material was synthesized by mixing stoichiometric starting amounts of the base element, heating it to 1100 °C for several hours and then allowed to in-furnace cool down to room temperature. To estimate the cooling profile, a linear thermal profile from 1100 °C to 25 °C over the course of 10 hours was used. The study found two distinct types of precipitates, one with a size of approximately 100 nm and number density of 1×10^{20} precipitates/m^3 and another much smaller distribution with

an average size of 4 nm and number density of 2 x 10^{22} precipitates/m^3 for a material with composition $PbTe_{.88}S_{.12}$.

The measurements of the larger precipitate were used to calibrate the PrecipiCalc simulation. Due to the limited information, a simple homogenous nucleation process was used with a constant surface energy term. The surface energy was allowed to vary until the number density of the large precipitates matched that found in experiment and was determined to be 0.005 J/m^2. This value is indicative of a coherent interface[229] as opposed to the experimentally determined semi-coherent interface[99]. This is likely due to the fact that a homogenous nucleation process was used for the simulation, whereas the actual nucleation process is much more complex and has a smaller barrier than homogenous nucleation. Often times, the surface energy can be adjusted to compensate to allow for heterogeneity[226]. The simulation results are shown in Figure 7.7(a) and (b) for the nucleation density and radius, respectively. The PrecipiCalc results also predict a two-particle distribution. The larger particle shows good agreement with the experimental data as the number density was used for calibration; however, the nanometer sized particle is within an order of magnitude for the radius size and one order of magnitude off for the number density. The discrepancy could be attributed to many factors including the not well described cooling curve, which probably has a much lower cooling rate as the furnace reaches room temperature, and would imply less time spent at higher temperatures. In addition, the assumption of a constant surface energy is also likely incorrect as the precipitates morphology can change from irregular to truncated cuboids depending on composition[229].

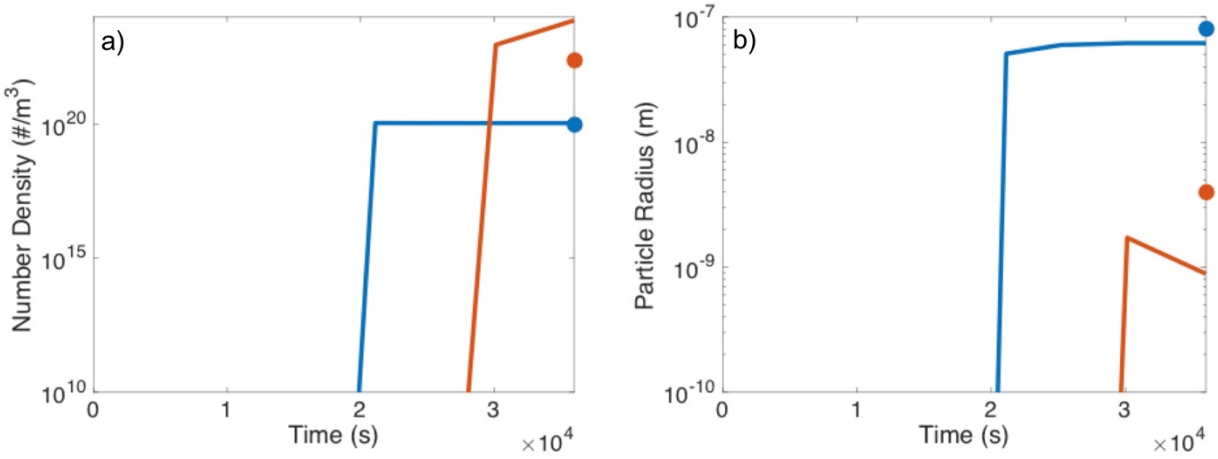

Figure 7.7: a) The number density as a function of time for two precipitate distributions and b) the average particle radius for the two distributions. Homogenous nucleation was assumed and the surface energy was assumed to be constant and fit to the number density data of the larger precipitate. Data from Yin et al. is shown as single points [216].

7.5 PbTe-PbS Microstructure

Due to the lack of literature data necessary to accurately calibrate the PrecipiCalc simulations, a controlled annealing experiment was performed to analyze the microstructural evolution of a sample with composition $PbTe_{.90}S_{.10}$. The sample was melted and held for solution treatment at 1100 °C for two days, which corresponds to an approximate diffusion distance of 1.4 mm to homogenize the sample. The sample was then cooled to 500 °C, which is inside the miscibility gap with an expected equilibrium of 0.023 mole fraction PbS. Samples were held there for 2, 3, 5, and 7 days and then quenched in ice water to freeze the kinetic process. Images were taken using a Scanning Electron Microscope (SEM) and Energy Dispersive X-ray Spectroscopy (EDS) was used for compositional analysis.

All of the samples studied contained four distinct microstructural morphologies that are shown in Figure 7.8 from a sample annealed for two days. The morphologies include small spherical precipitates with radii on the order of 200 nm, larger spherical precipitates with radii on the order of 1 μm, large irregular shaped precipitates the size of several micrometers, and large

stripes of various micrometer length, which are shown in Figure 7.8 (a), (b), (c), and (d), respectively. The previous study reported a bimodal distribution, but did not mention the irregularity of the other shapes [216]. The growth of the individual morphologies was tracked with time, but a statistically significant trend for growth was not seen, although there is evidence that the microstructural growth process is not one dictated by nucleation and growth.

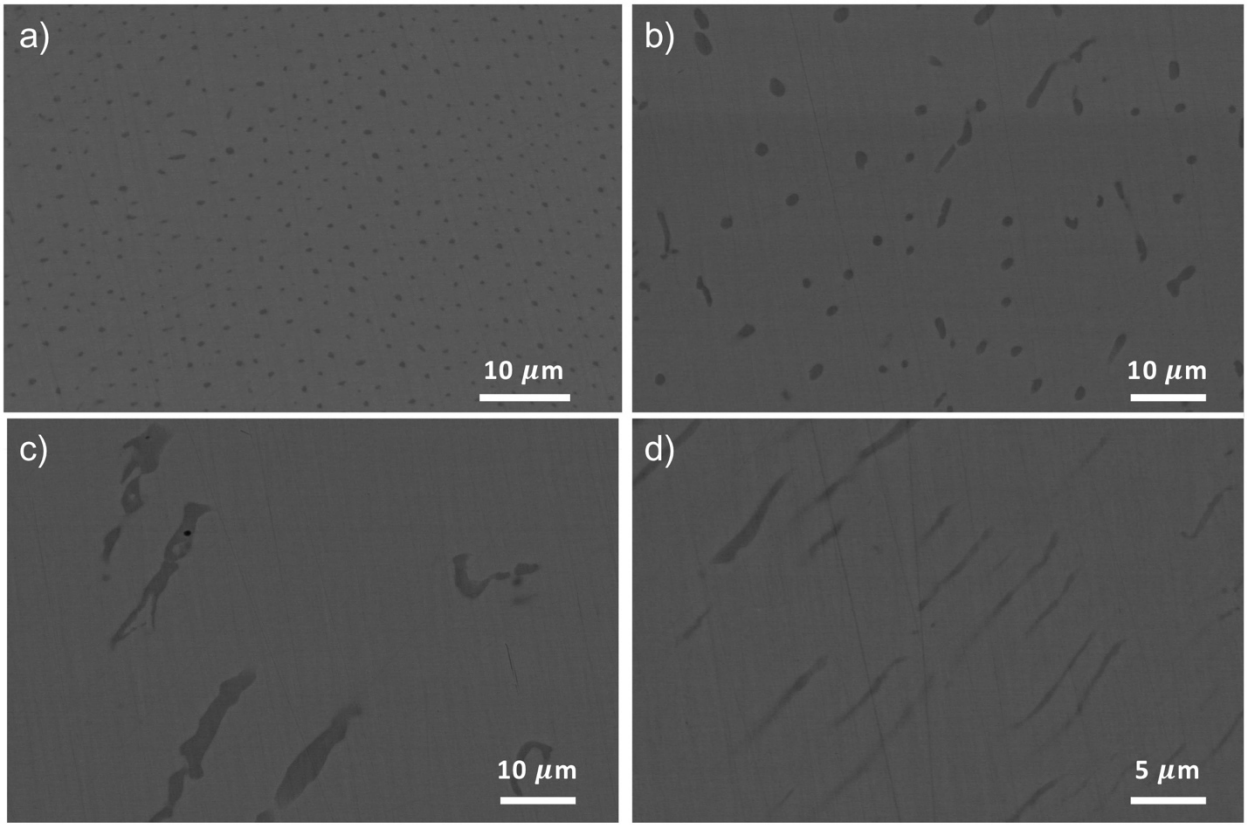

Figure 7.8: Typical microstructure morphology from $PbTe_{.90}S_{.10}$ annealed at 500 °C for two days. The microstructure consists of a) uniform spheres of size 200 nm, b) larger spheres approximately 1 μm, c) large irregular shapes, and d) large stripes

Many of the previously mentioned microstructural morphologies can be seen in **Error! Reference source not found.** that appear to be contained in grains. The precipitates near the boundaries take on the long-striped morphology but then become more spheroidal and smaller near the center of the grain. The enlarged regions of the small nanoprecipitates show a very ordered arrangement that is not indicative of the random placement one would expect from a homogenous

nucleation process. Instead, these microstructural features are more representative of a discontinuous precipitation (DP) process. DP appears when nucleation occurs preferentially at the grain boundaries, which also happen to be moving [230]. The simultaneous precipitation and moving grain boundary can then create a lamellar or rod-like structure. The DP process has been modeled using phase field methods as well[231, 232]. These studies have determined the necessity of having a high grain boundary mobility and atomic mobility in order to create the DP microstructure. Therefore, a firmer understanding of the grain boundary velocity will be necessary in order to model these microstructures.

The lamellar structure has been seen in previous studies of higher PbS concentration, which identified the microstructure as spinodal decomposition and shown in Figure 7.10 from Girard et al[233]. The case for DP instead of spinodal decomposition is strengthened as there is an 8% difference in lattice parameter between the PbTe and PbS phase, which introduces a large amount of strain energy. A previous study calculated the effect of the strain energy for determining the coherent spinodal line and found that the spinodal line was largely depressed to below 610 K for all compositions in the PbTe-PbS system[123]. In addition, the DP process was observed in the (Pb,Sn,Ge)Te system for compositions inside the miscibility gap[130].

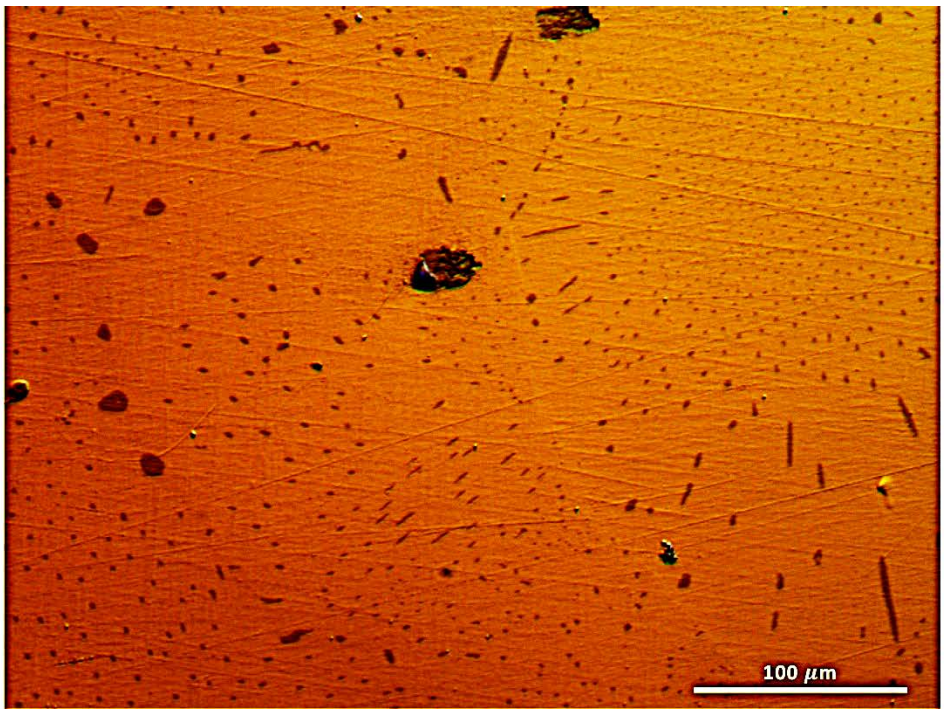

Figure 7.9: Optical micrograph illustrating possible discontinuous precipitation process in $PbTe_{.90}S_{.10}$. Preferential precipitation on moving grain boundaries cause the stripes, which break up in a spheroidization process caused by Rayleigh instabilities.

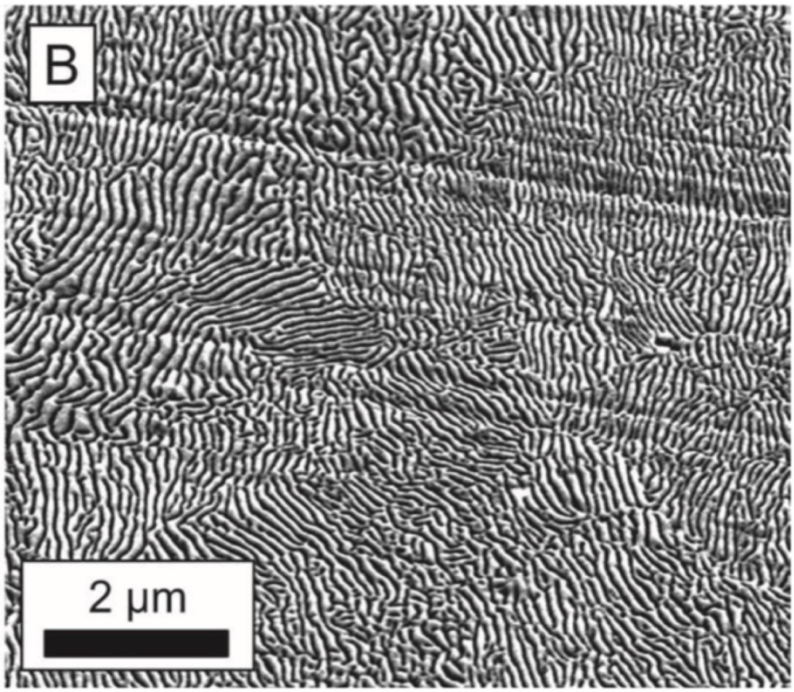

Figure 7.10: Microstructure of $PbTe_{.70}S_{.30}$ from Girard et al[233] showing lamellar structure that is likely caused by discontinuous precipitation instead of spinodal decomposition.

The spherical particles are likely created through a spheroidization process that occurs when the samples are annealed. The lamellar structure forms perpendicular to the moving grain boundary that create aligned rods. Upon further annealing, a Rayleigh instability causes infinitesimal perturbations that cause the structure to break apart at a characteristic length and becomes a spheroid[234]. The resulting microstructure are aligned spheres with consistent spacing, that is evident in Figure 7.8 (a) and **Error! Reference source not found.**. This DP and spheroidization process has been seen in dilute Co-Cu alloys[230] as well as in Au nanowires[235]. In addition, the Rayleigh instabilities created through discontinuous precipitation has been modeled using phase field methods and a similar microstructure to those in the previous studies and here are seen giving further evidence that the microstructural evolution is caused by DP and spheroidization[236].

7.6 Conclusion

The process for which a thermoelectric material can be designed using these models has been described. A Debye-Callaway model can be used to determine the optimal precipitate radius, which lowers the thermal conductivity for a fixed volume fraction. The thermodynamic phase diagram can be used to determine the composition necessary to achieve a desired volume fraction as well as the amount of point defects found in the matrix. A single parabolic band model can be used to determine the optimal carrier concentration, which is related to the solubility of Na in PbTe dictated by the phase diagram. The thermodynamic and kinetic assessments are used with PrecipiCalc to determine the processing conditions for the optimal microstructure. Due to the limited literature data, the microstructure of annealed $PbTe_{0.90}S_{0.10}$ was examined. A microstructure that was indicative of discontinuous precipitation was observed, which would create added complexity in the evolution modeling of second phase structures.

Conclusions

The thermodynamic descriptions using the CALPHAD method have been developed on the Pb(S,Se,Te) system. First-principles calculations were performed to gain insight into the dominant defects of the system as well as physically relevant values such as formation energies and ionization energies of the defects. These calculations served as inputs into two CALPHAD models, a 5SL and 2SL model, to describe the intrinsic carriers of the system. The 2SL model is a new description and improves on the previously founded 5SL model by being multicomponent compatible while still maintaining physical relevance.

The 2SL model was used to model the pseudobinaries and pseudoternary in the Pb(S,Se,Te) system and incorporated Na doping in the PbX compounds. These models can be used to determine the carrier concentration of Na doped alloys in the PbX system. The PbS-PbTe was chosen to perform a kinetic assessment on and diffusion couples were created to determine the interdiffusion coefficients of S and Te. The CALPHAD method was used to determine the mobilities and is in good agreement with the modeled diffusion coefficients and diffusion profile.

The methodology of the 2SL model was used to create a 3SL model for the A-Q (A=Bi, Sb; Q=Te, Se) systems. The species of the model depend on the individual dominant defects of the system, but the optimized interaction parameters can be used to determine formation energies. Full assessments of each of the systems were performed and a method for modeling homologous compounds that appear within the system has been proposed.

Lastly, the methodology for how the thermodynamic and kinetic models can be used to optimize a thermoelectric material have been shown. The Debye-Callaway model can be used to determine an optimal precipitate radius and uses the solubility of alloying elements to determine the effect of solid solution scattering on the lattice thermal conductivity. A single parabolic band

model can be used to determine the optimal carrier concentration for maximum power factor. The carrier concentration can then be linked back to the solubility of Na in the individual compounds to determine if it is accessible. The thermodynamic and kinetic databases can be used with PrecipiCalc to determine the processing conditions that produce a desired microstructure. In order for proper calibration of the PrecipiCalc simulations, controlled annealing experiments of Pb(S,Te) alloys were conducted. The resulting microstructure indicates that the material evolves through a discontinuous precipitation process instead of nucleation and growth and that many examples in the literature that were interpreted as spinodally decomposed are likely a result of this discontinuous precipitation process.

References

[1] N.A.o. Engineering, NAE Grand Challenges for Engineering, National Academy of Sciences (2017).

[2] A. White, The Materials Genome Initiative: One year on, Mrs Bulletin 37(8) (2012) 715-716.

[3] N.R. Council, *Integrated Computational Materials Engineering: A Transformational Discipline for Improved Competitiveness and National Security*, The National Academies Press, Washington, DC, 2008.

[4] N.R. Council, Accelerating Technology Transition: Bridging the Valley of Death for Materials and Processes in Defense Systems, Washington, DC, 2004.

[5] H.L. Lukas, Computational thermodynamics : the CALPHAD method / Hans Lukas, Suzana G. Fries, Bo Sundman, Cambridge : Cambridge University Press, Cambridge, 2007.

[6] Z.K. Liu, First-Principles Calculations and CALPHAD Modeling of Thermodynamics, Journal of Phase Equilibria and Diffusion 30(5) (2009) 517-534.

[7] F.J. DiSalvo, Thermoelectric cooling and power generation, Science 285(5428) (1999) 703-706.

[8] L.L.N.L.a.D.o. Energy, Estimated US Energy Consumption in 2015, (2016).

[9] J. He, T.M. Tritt, Advances in thermoelectric materials research: Looking back and moving forward, Science 357(6358) (2017).

[10] G.J. Snyder, E.S. Toberer, Complex thermoelectric materials, Nature Materials 7(2) (2008) 105-114.

[11] Y.Z. Pei, Z.M. Gibbs, A. Gloskovskii, B. Balke, W.G. Zeier, G.J. Snyder, Optimum Carrier Concentration in n-Type PbTe Thermoelectrics, Advanced Energy Materials 4(13) (2014) 12.

[12] G.J. Tan, F.Y. Shi, S.Q. Hao, L.D. Zhao, H. Chi, X.M. Zhang, C. Uher, C. Wolverton, V.P. Dravid, M.G. Kanatzidis, Non-equilibrium processing leads to record high thermoelectric figure of merit in PbTe-SrTe, Nature Communications 7 (2016).

[13] Y.Z. Pei, X.Y. Shi, A. LaLonde, H. Wang, L.D. Chen, G.J. Snyder, Convergence of electronic bands for high performance bulk thermoelectrics, Nature 473(7345) (2011) 66-69.

[14] R.F. Brebrick, R.S. Allgaier, COMPOSITION LIMITS OF STABILITY OF PBTE, Journal of Chemical Physics 32(6) (1960) 1826-1831.

[15] Y.Z. Pei, J. Lensch-Falk, E.S. Toberer, D.L. Medlin, G.J. Snyder, High Thermoelectric Performance in PbTe Due to Large Nanoscale Ag-2 Te Precipitates and La Doping, Advanced Functional Materials 21(2) (2011) 241-249.

[16] W.D. Callister, Materials Science and Engineering, John Wiley & Sons (8) (2010).

[17] U. Ozgur, Y.I. Alivov, C. Liu, A. Teke, M.A. Reshchikov, S. Dogan, V. Avrutin, S.J. Cho, H. Morkoc, A comprehensive review of ZnO materials and devices, Journal of Applied Physics 98(4) (2005).

[18] C. Freysoldt, B. Grabowski, T. Hickel, J. Neugebauer, G. Kresse, A. Janotti, C.G. Van de Walle, First-principles calculations for point defects in solids, Reviews of Modern Physics 86(1) (2014).

[19] C.G. Van de Walle, J. Neugebauer, First-principles calculations for defects and impurities: Applications to III-nitrides, Journal of Applied Physics 95(8) (2004) 3851-3879.

[20] A.F. Kohan, G. Ceder, D. Morgan, C.G. Van de Walle, First-principles study of native point defects in ZnO, Physical Review B 61(22) (2000) 15019-15027.

[21] J.W. Doak, K.J. Michel, C. Wolverton, Determining dilute-limit solvus boundaries in multi-component systems using defect energetics: Na in PbTe and PbS, Journal of Materials Chemistry C 3(40) (2015) 10630-10649.

[22] S. Bajaj, G.S. Pomrehn, J.W. Doak, W. Gierlotka, H.J. Wu, S.W. Chen, C. Wolverton, W.A. Goddard, G.J. Snyder, Ab initio study of intrinsic point defects in PbTe: an insight into phase stability, Acta Materialia 92 (2015) 72-80.

[23] A. Goyal, P. Gorai, E.S. Toberer, V. Stevanovic, First-principles calculation of intrinsic defect chemistry and self-doping in PbTe, Npj Computational Materials 3 (2017).

[24] Y. Wang, S. Curtarolo, C. Jiang, R. Arroyave, T. Wang, G. Ceder, L.Q. Chen, Z.K. Liu, Ab initio lattice stability in comparison with CALPHAD lattice stability, Calphad-Computer Coupling of Phase Diagrams and Thermochemistry 28(1) (2004) 79-90.

[25] P.E.A. Turchi, I.A. Abrikosov, B. Burton, S.G. Fries, G. Grimvalle, L. Kaufman, P. Korzhavyi, V.R. Manga, M. Ohno, A. Pisch, A. Scott, W.Q. Zhang, Interface between quantum-mechanical-based approaches, experiments, and CALPHAD methodology, Calphad-Computer Coupling of Phase Diagrams and Thermochemistry 31(1) (2007) 4-27.

[26] Y. Zhong, C. Wolverton, Y.A. Chang, Z.K. Liu, A combined CALPHAD/first-principles remodeling of the thermodynamics of Al-Sr: unsuspected ground state energies by "rounding up the (un)usual suspects", Acta Materialia 52(9) (2004) 2739-2754.

[27] K. Ozturk, Y. Zhong, L.Q. Chen, C. Wolverton, J.O. Sofo, Z.K. Liu, Linking first-principles energetics to CALPHAD: An application to thermodynamic modeling of the Al-Ca binary system, Metallurgical and Materials Transactions a-Physical Metallurgy and Materials Science 36A(1) (2005) 5-13.

[28] D. Shin, J.E. Saal, Z.K. Liu, Thermodynamic modeling of the Cu-Si system, Calphad-Computer Coupling of Phase Diagrams and Thermochemistry 32(3) (2008) 520-526.

[29] Y. Zhong, M. Yang, Z.K. Liu, Contribution of first-principles energetics to Al-Mg thermodynamic modeling, Calphad-Computer Coupling of Phase Diagrams and Thermochemistry 29(4) (2005) 303-311.

[30] Y. Wang, L.G. Hector, H. Zhang, S.L. Shang, L.Q. Chen, Z.K. Liu, A thermodynamic framework for a system with itinerant-electron magnetism, Journal of Physics-Condensed Matter 21(32) (2009).

[31] J. Rogal, S.V. Divinski, M.W. Finnis, A. Glensk, J. Neugebauer, J.H. Perepezko, S. Schuwalow, M.H.F. Sluiter, B. Sundman, Perspectives on point defect thermodynamics, Physica Status Solidi B-Basic Solid State Physics 251(1) (2014) 97-129.

[32] S. Lany, A. Zunger, Assessment of correction methods for the band-gap problem and for finite-size effects in supercell defect calculations: Case studies for ZnO and GaAs, Physical Review B 78(23) (2008).

[33] G. Makov, M.C. Payne, PERIODIC BOUNDARY-CONDITIONS IN AB-INITIO CALCULATIONS, Physical Review B 51(7) (1995) 4014-4022.

[34] S. Bajaj, H. Wang, J.W. Doak, C. Wolverton, G.J. Snyder, Calculation of dopant solubilities and phase diagrams of X-Pb-Se (X = Br, Na) limited to defects with localized charge, Journal of Materials Chemistry C 4(9) (2016) 1769-1775.

[35] W. Kohn, L.J. Sham, SELF-CONSISTENT EQUATIONS INCLUDING EXCHANGE AND CORRELATION EFFECTS, Physical Review 140(4A) (1965) 1133-&.

[36] P. Hohenberg, W. Kohn, INHOMOGENEOUS ELECTRON GAS, Physical Review B 136(3B) (1964) B864-+.

[37] G. Kresse, J. Hafner, AB-INITIO MOLECULAR-DYNAMICS SIMULATION OF THE LIQUID-METAL AMORPHOUS-SEMICONDUCTOR TRANSITION IN GERMANIUM, Physical Review B 49(20) (1994) 14251-14269.

[38] G. Kresse, J. Furthmuller, Efficient iterative schemes for ab initio total-energy calculations using a plane-wave basis set, Physical Review B 54(16) (1996) 11169-11186.

[39] G. Kresse, D. Joubert, From ultrasoft pseudopotentials to the projector augmented-wave method, Physical Review B 59(3) (1999) 1758-1775.

[40] J.P. Perdew, K. Burke, M. Ernzerhof, Generalized gradient approximation made simple, Physical Review Letters 77(18) (1996) 3865-3868.

[41] A. Belsky, M. Hellenbrandt, V.L. Karen, P. Luksch, New developments in the Inorganic Crystal Structure Database (ICSD): accessibility in support of materials research and design, Acta Crystallographica Section B-Structural Science 58 (2002) 364-369.

[42] H.J. Monkhorst, J.D. Pack, SPECIAL POINTS FOR BRILLOUIN-ZONE INTEGRATIONS, Physical Review B 13(12) (1976) 5188-5192.

[43] M. Gajdos, K. Hummer, G. Kresse, J. Furthmuller, F. Bechstedt, Linear optical properties in the projector-augmented wave methodology, Physical Review B 73(4) (2006).

[44] S. Baroni, R. Resta, ABINITIO CALCULATION OF THE MACROSCOPIC DIELECTRIC-CONSTANT IN SILICON, Physical Review B 33(10) (1986) 7017-7021.

[45] X. Wu, D. Vanderbilt, D.R. Hamann, Systematic treatment of displacements, strains, and electric fields in density-functional perturbation theory, Physical Review B 72(3) (2005).

[46] R.F. Brebrick, E. Gubner, PBSE COMPOSITION STABILITY LIMITS, Journal of Chemical Physics 36(1) (1962) 170-&.

[47] E.O. Wrasse, P. Venezuela, R.J. Baierle, Ab initio study of point defects in PbSe and PbTe: Bulk and nanowire, Journal of Applied Physics 116(18) (2014).

[48] N. Ohashi, K. Igaki, PHYSICO-CHEMICAL STUDY ON LEAD SELENIDE, Transactions of the Japan Institute of Metals 5(2) (1964) 94-&.

[49] N. Chou, K. Komarek, E. Miller, RETROGRADE SOLUBILITY OF PBS, PBSE, AND PBTE, Transactions of the Metallurgical Society of Aime 245(7) (1969) 1553-&.

[50] O. Madelung, Semiconductors: Data Handbook / by Otfried Madelung, 3rd edition.. ed., Berlin, Heidelberg : Springer Berlin Heidelberg : Imprint: Springer2004.

[51] A.R. Calawa, T.C. Harman, M. Finn, P. Youtz, CRYSTAL GROWTH ANNEALING AND DIFFUSION OF LEAD-TIN CHALCOGENIDES, Transactions of the Metallurgical Society of Aime 242(3) (1968) 374-&.

[52] B.J. Sealy, A.J. Crocker, TheP-T-x phase diagram of PbTe and PbSe, Journal of materials science 8(12) (1973) 1737-1743.

[53] N. Wang, D. West, J.W. Liu, J. Li, Q.M. Yan, B.L. Gu, S.B. Zhang, W.H. Duan, Microscopic origin of the p-type conductivity of the topological crystalline insulator SnTe and the effect of Pb alloying, Physical Review B 89(4) (2014).

[54] P.J. Spencer, A brief history of CALPHAD, Calphad-Computer Coupling of Phase Diagrams and Thermochemistry 32(1) (2008) 1-8.

[55] L. Kaufman, H. Bernstein, Computer calculation of phase diagrams with special reference to refractory metals, in: A. Press (Ed.) New York, 1970.

[56] M. Hillert, The compound energy formalism, Journal of Alloys and Compounds 320(2) (2001) 161-176.

[57] S.M. Huang, Y.J. Liu, Y. Chen, Z.T. Kang, Thermodynamic Descriptions and Phase Diagrams for Pb-S and Bi-S Binary Systems, Journal of Electronic Materials 43(4) (2014) 1237-1243.

[58] Y. Liu, Z. Kang, G. Sheng, L. Zhang, J. Wang, Z. Long, Phase Equilibria and Thermodynamic Basis for the Cd-Se

and Pb-Se Binary Systems, Journal of Electronic Materials 41(7) (2012) 1915-1923.

[59] Q. Chen, M. Hillert, B. Sundman, W.A. Oates, S.G. Fries, R. Schmid-Fetzer, Phase equilibria, defect chemistry and semiconducting properties of CdTe(s) - Thermodynamic modeling, Journal of Electronic Materials 27(8) (1998) 961-971.

[60] R.F. Brebrick, E. Gubner, COMPOSITION STABILITY LIMITS OF PBTE. .2, Journal of Chemical Physics 36(5) (1962) 1283-&.

[61] W.W. Scanlon, PRECIPITATION OF TE AND PB IN PBTE CRYSTALS, Physical Review 126(2) (1962) 509-&.

[62] T.C. Harman, Control of Imperfections in Crystals of Pb1-xSnxTe, Pb1-xSnxSe, and PbS1-xSex Journal of Nonmetals, 1973, pp. 183-194.

[63] C.R. Hewes, M.S. Adler, S.D. Senturia, ANNEALING STUDIES OF PBTE AND PB1-XSNXTE, Journal of Applied Physics 44(3) (1973) 1327-1332.

[64] W. Albers, C. Haas, H.J. Vink, Phillips Res. Rep, 1963, p. 372.

[65] M. Muhlberg, D. Hesse, TEM PRECIPITATION STUDIES IN TE-RICH AS-GROWN PBTE SINGLE-CRYSTALS, Physica Status Solidi a-Applied Research 76(2) (1983) 513-524.

[66] M. Schenk, H. Berger, A. Klimakow, M. Muhlberg, M. Wienecke, NONSTOICHIOMETRY AND POINT-DEFECTS IN PBTE, Crystal Research and Technology 23(1) (1988) 77-84.

[67] F.A. Kroger, H.J. Vink, RELATIONS BETWEEN THE CONCENTRATIONS OF IMPERFECTIONS IN CRYSTALLINE SOLIDS, Solid State Physics 3 (1956) 307-435.

[68] Y.G. Sha, R.F. Brebrick, EXPLICIT INCORPORATION OF THE ENERGY-BAND STRUCTURE INTO AN ANALYSIS OF THE DEFECT CHEMISTRY OF PBTE AND SNTE, Journal of Electronic Materials 18(3) (1989) 421-443.

[69] J. Bloem, F.A. Kroger, The P-T-X Phase Diagram of the Lead-Sulfur System, Z. Phys. Chem 7 (1956) 1-14.

[70] Y. Nensberg, A. Petrov, Thermally Generated Charge Carriers in PbS, InOrganic Material, 1965, p. 1365.

[71] A.J. Strauss, RETROGRADE SOLUBILITY OF LEAD IN N-TYPE PBS, Transactions of the Metallurgical Society of Aime 239(6) (1967) 794-&.

[72] A. Walsh, Defect Processes in a PbS Metal Organic Framework: A Quantum-Confined Hybrid Semiconductor, Journal of Physical Chemistry Letters 1(8) (2010) 1284-1287.

[73] W.F. Li, C.M. Fang, M. Dijkstra, M.A. van Huis, The role of point defects in PbS, PbSe and PbTe: a first principles study, Journal of Physics-Condensed Matter 27(35) (2015) 14.

[74] R.C. Sharma, J.C. Lin, Y.A. Chang, A THERMODYNAMIC ANALYSIS OF THE PB-S SYSTEM AND CALCULATION OF THE PB-S PHASE-DIAGRAM, Metallurgical Transactions B-Process Metallurgy 18(1) (1987) 237-244.

[75] J.C. Lin, R.C. Sharma, Y.A. Chang, The Pb-Se (lead-selenium) system, Journal of Phase Equilibria 17(3) (1996) 253-260.

[76] U. Kattner, H.L. Lukas, G. Petzow, OPTIMIZATION AND CALCULATION OF THE PB-TE SYSTEM, Calphad-Computer Coupling of Phase Diagrams and Thermochemistry 10(2) (1986) 103-116.

[77] W. Gierlotka, J. Lapsa, D. Jendrzejczyk-Handzik, Thermodynamic description of the Pb-Te system using ionic liquid model, Journal of Alloys and Compounds 479(1-2) (2009) 152-156.

[78] W.A. Oates, G. Eriksson, H. Wenzl, THERMODYNAMIC MODELING OF SOLID GALLIUM-ARSENIDE, Journal of Alloys and Compounds 220(1-2) (1995) 48-52.

[79] Q. Chen, M. Hillert, The compound energy model for compound semiconductors, Journal of Alloys and Compounds 245 (1996) 125-131.

[80] J.B. Li, J.C. Tedenac, Thermodynamic modeling of native point defects and dopants of GaN semiconductors, Journal of Electronic Materials 31(4) (2002) 321-326.

[81] J.B. Li, L.L. Kerr, Thermodynamic modeling of native defects in ZnO, Optical Materials 35(6) (2013) 1213-1217.

[82] Y.Z. Pei, A. LaLonde, S. Iwanaga, G.J. Snyder, High thermoelectric figure of merit in heavy hole dominated PbTe, Energy & Environmental Science 4(6) (2011) 2085-2089.

[83] H. Wang, E. Schechtel, Y.Z. Pei, G.J. Snyder, High Thermoelectric Efficiency of n-type PbS, Advanced Energy Materials 3(4) (2013) 488-495.

[84] Q. Zhang, F. Cao, W.S. Liu, K. Lukas, B. Yu, S. Chen, C. Opeil, D. Broido, G. Chen, Z.F. Ren, Heavy Doping and Band Engineering by Potassium to Improve the Thermoelectric Figure of Merit in p-Type PbTe, PbSe, and PbTe1-ySey, Journal of the American Chemical Society 134(24) (2012) 10031-10038.

[85] H. Wang, Y.Z. Pei, A.D. LaLonde, G.J. Snyder, Weak electron-phonon coupling contributing to high thermoelectric performance in n-type PbSe, Proceedings of the National Academy of Sciences of the United States of America 109(25) (2012) 9705-9709.

[86] A.T. Dinsdale, SGTE DATA FOR PURE ELEMENTS, Calphad-Computer Coupling of Phase Diagrams and Thermochemistry 15(4) (1991) 317-425.

[87] P. Franke, Modeling of Thermal Vacancies in Metals within the Framework of the Compound Energy Formalism, Journal of Phase Equilibria and Diffusion 35(6) (2014) 780-787.

[88] A.T. Dinsdale, A.V. Khvan, A. Watson, Critical Assessment 5: Thermodynamic data for vacancies, Materials Science and Technology 30(14) (2014) 1715-1718.

[89] B. Jansson, Ph.D. Thesis, Royal Institute of Technology, Stockholm, Sweden, 1984.

[90] B. Sundman, B. Jansson, J.O. Andersson, THE THERMO-CALC DATABANK SYSTEM, Calphad-Computer Coupling of Phase Diagrams and Thermochemistry 9(2) (1985) 153-190.

[91] J.C. Lin, K.C. Hsleh, R.C. Sharma, Y.A. Chang, The Pb-Te (lead-tellurium) system, Bulletin of alloy phase diagrams. 10(4) (1989) 340-347.

[92] J.C. Lin, R.C. Sharma, Y.A. Chang, The Pb−S (Lead-Sulfur) system, Bulletin of alloy phase diagrams. 7(4) (1986) 374-381.

[93] M. Stan, B. Reardon, A Bayesian approach to evaluating the uncertainty of thermodynamic data and phase diagrams, Calphad-Computer Coupling of Phase Diagrams and Thermochemistry 27(3) (2003) 319-323.

[94] R.A. Otis, Z.K. Liu, High-Throughput Thermodynamic Modeling and Uncertainty Quantification for ICME, Jom 69(5) (2017) 886-892.

[95] Y.F. Liu, L. You, C.Y. Wang, J.Y. Zhang, J. Yang, K. Guo, J. Luo, W.Q. Zhang, Enhancing Thermoelectric Performance of PbSe by Se Vacancies, Journal of Electronic Materials 47(5) (2018) 2584-2590.

[96] M.H. Zhao, C. Chang, Y. Xiao, L.D. Zhao, High performance of n-type (PbS)(1-x-y)(PbSe)(x)(PbTe)(y) thermoelectric materials, Journal of Alloys and Compounds 744 (2018) 769-777.

[97] S. Johnsen, J.Q. He, J. Androulakis, V.P. Dravid, I. Todorov, D.Y. Chung, M.G. Kanatzidis, Nanostructures Boost the Thermoelectric Performance of PbS, Journal of the American Chemical Society 133(10) (2011) 3460-3470.

[98] H. Wang, Z.M. Gibbs, Y. Takagiwa, G.J. Snyder, Tuning bands of PbSe for better thermoelectric efficiency, Energy & Environmental Science 7(2) (2014) 804-811.

[99] S.N. Girard, J.Q. He, X.Y. Zhou, D. Shoemaker, C.M. Jaworski, C. Uher, V.P. Dravid, J.P. Heremans, M.G. Kanatzidis, High Performance Na-doped PbTe-PbS Thermoelectric Materials: Electronic Density of States Modification and Shape-Controlled Nanostructures, Journal of the American Chemical Society 133(41) (2011) 16588-16597.

[100] J.Q. He, S.N. Girard, M.G. Kanatzidis, V.P. Dravid, Microstructure-Lattice Thermal Conductivity Correlation in Nanostructured PbTe0.7S0.3 Thermoelectric Materials, Advanced Functional Materials 20(5) (2010) 764-772.

[101] H. Wang, A.D. LaLonde, Y.Z. Pei, G.J. Snyder, The Criteria for Beneficial Disorder in Thermoelectric Solid Solutions, Advanced Functional Materials 23(12) (2013) 1586-1596.

[102] S.A. Yamini, H. Wang, Z.M. Gibbs, Y.Z. Pei, S.X. Dou, G.J. Snyder, Chemical composition tuning in quaternary p-type Pb-chalcogenides - a promising strategy for enhanced thermoelectric performance, Physical Chemistry Chemical Physics 16(5) (2014) 1835-1840.

[103] S.A. Yamini, D.R.G. Mitchell, Z.M. Gibbs, R. Santos, V. Patterson, S. Li, Y.Z. Pei, S.X. Dou, G.J. Snyder, Heterogeneous Distribution of Sodium for High Thermoelectric Performance of p-type Multiphase Lead-Chalcogenides, Advanced Energy Materials 5(21) (2015).

[104] D. Ginting, C.C. Lin, R. Lydia, H.S. So, H. Lee, J. Hwang, W. Kim, R.A.R. Al Orabi, J.S. Rhyee, High thermoelectric performance in pseudo quaternary compounds of (PbTe)(0.95-

x)(PbSe)(x)(PbS)(0.05) by simultaneous band convergence and nano precipitation, Acta Materialia 131 (2017) 98-109.

[105] R.J. Korkosz, T.C. Chasapis, S.H. Lo, J.W. Doak, Y.J. Kim, C.I. Wu, E. Hatzikraniotis, T.P. Hogan, D.N. Seidman, C. Wolverton, V.P. Dravid, M.G. Kanatzidis, High ZT in p-Type (PbTe)(1-2x)(PbSe)(x)(PbS)(x) Thermoelectric Materials, Journal of the American Chemical Society 136(8) (2014) 3225-3237.

[106] Y.Z. Pei, A.F. May, G.J. Snyder, Self-Tuning the Carrier Concentration of PbTe/Ag2Te Composites with Excess Ag for High Thermoelectric Performance, Advanced Energy Materials 1(2) (2011) 291-296.

[107] J.Q. He, L.D. Zhao, J.C. Zheng, J.W. Doak, H.J. Wu, H.Q. Wang, Y. Lee, C. Wolverton, M.G. Kanatzidis, V.P. Dravid, Role of Sodium Doping in Lead Chalcogenide Thermoelectrics, Journal of the American Chemical Society 135(12) (2013) 4624-4627.

[108] A.J. Crocker, ROLE OF SODIUM IN LEAD TELLURIDE, Journal of Physics and Chemistry of Solids 28(10) (1967) 1903-&.

[109] Y. Takagiwa, Y.Z. Pei, G. Pomrehn, G.J. Snyder, Validity of rigid band approximation of PbTe thermoelectric materials, Apl Materials 1(1) (2013).

[110] A.A. Volykhov, L.V. Yashina, V.I. Shtanov, Phase relations in pseudobinary systems of germanium, tin, and lead chalcogenides, Inorganic Materials 42(6) (2006) 596-604.

[111] H. Liu, L.L.Y. Chang, PHASE-RELATIONS IN THE SYSTEM PBS-PBSE-PBTE, Mineralogical Magazine 58(393) (1994) 567-578.

[112] M.C. Peters, Doak, Jeff W., Zhang, W-.W., Saal, J.E., Olson, G.B., Voorhees, P.W., Thermodynamic modeling of the PbX (X=S,Te) phase diagram using a five sub-lattice and two

sub-lattice model, Calphad-Computer Coupling of Phase Diagrams and Thermochemistry 58 (2017) 17-24.

[113] J.I. Ganguly, S.K. Saxena, Mixtures and Mineral Reactions (1987) 291.

[114] S.A. Yamini, T. Ikeda, A. Lalonde, Y.Z. Pei, S.X. Dou, G.J. Snyder, Rational design of p-type thermoelectric PbTe: temperature dependent sodium solubility, Journal of Materials Chemistry A 1(31) (2013) 8725-8730.

[115] M.S. Darrow, W.B. White, R. Roy, Phase Relations in the System PbS-PbTe, Trans. Metall. Soc. AIME 236 (1966) 654-658.

[116] V.N. Demin, I.G. Bukreeva, A.M. Gaskov, V.P. Zlomanov, A.V. Novoselova, CRYSTAL-GROWTH FROM VAPOR-PHASE AND THE REGION OF HOMOGENEITY OF THE SOLID-SOLUTION PB1-Y(SXTE1-X)Y, Inorganic Materials 22(1) (1986) 27-29.

[117] V. Leute, N. Volkmar, A Contribution to the Phase Diagram of the Quasibinary System Pb(Se,Te), Z. Phys. Chez. Neue Folge 144 (1985) 145-155.

[118] Elagina, Investigation of the PbTe-PbSe System, Doklady Akademii nauk SSSR 111(2) (1956) 334-336.

[119] D.E. Grimes, Pb-PbTe-PbSe Subternary System, Transactions of Metallurgical Society of AIME 233(7) (1965) 1442.

[120] J. Steininger, PHASE DIAGRAM OF PBTE-PBSE PSEUDOBINARY SYSTEM, Metallurgical Transactions 1(10) (1970) 2939-+.

[121] M.S. Kim, W.J. Lee, K.H. Cho, J.P. Ahn, Y.M. Sung, Spinodally Decomposed PbSe-PbTe Nanoparticles for High-Performance Thermoelectrics: Enhanced Phonon Scattering and Unusual Transport Behavior, ACS Nano 10(7) (2016) 7197-7207.

[122] D. Usanmaz, P. Nath, J.J. Plata, G.L.W. Hart, I. Takeuchi, M.B. Nardelli, M. Fornari, S. Curtarolo, First principles thermodynamical modeling of the binodal and spinodal curves in lead chalcogenides, Physical Chemistry Chemical Physics 18(6) (2016) 5005-5011.

[123] J.W. Doak, C. Wolverton, Coherent and incoherent phase stabilities of thermoelectric rocksalt IV-VI semiconductor alloys, Physical Review B 86(14) (2012).

[124] S.D. Gromakov, I.V. Zoroatskaya, Z.M. Latypov, M.A. Chvala, E.A. Eidelman, L.I. Badygina, L.G. Zaripova, K METODIKE IZUCHENIYA FAZOVYKH DIAGRAMM POLUPROVODNIKOVYKH SISTEM, Zhurnal Neorganicheskoi Khimii 9(10) (1964) 2485-2487.

[125] A.J. Strauss, T.C. Harman, Pseudobinary Phase Diagram and Existence Regions for PbS1-xSex, Journal of Electronic Materials 2(1) (1973) 71.

[126] L.A. Kuznetsova, V.I. Shtanov, V.P. Zlomanov, V.L. Kuznetsov, THE T-X-Y DIAGRAM OF THE PBSE-PB-PBS SYSTEM, Inorganic Materials 23(3) (1987) 342-345.

[127] S.A. Yamini, H. Wang, D. Ginting, D.R.G. Mitchell, S.X. Dou, G.J. Snyder, Thermoelectric Performance of n-Type (PbTe)(0.75)(PbS)(0.15)(PbSe)(0.1) Composites, Acs Applied Materials & Interfaces 6(14) (2014) 11476-11483.

[128] Y.B. Kang, A.D. Pelton, Modeling short-range ordering in liquids: The Mg-Al-Sn system, Calphad-Computer Coupling of Phase Diagrams and Thermochemistry 34(2) (2010) 180-188.

[129] J. Androulakis, C.H. Lin, H.J. Kong, C. Uher, C.I. Wu, T. Hogan, B.A. Cook, T. Caillat, K.M. Paraskevopoulos, M.G. Kanatzidis, Spinodal decomposition and nucleation and growth as a means to bulk nanostructured thermoelectrics: Enhanced performance in Pb1-xSnxTe-PbS, Journal of the American Chemical Society 129(31) (2007) 9780-9788.

[130] Y. Rosenberg, Y. Gelbstein, M.P. Dariel, Phase separation and thermoelectric properties of the Pb0.25Sn0.25Ge0.5Te compound, Journal of Alloys and Compounds 526 (2012) 31-38.

[131] H.E. Lippard, C.E. Campbell, T. Bjorklind, U. Borggren, P. Kellgren, V.P. Dravid, G.B. Olson, Microsegregation behavior during solidification and homogenization of AerMet100 steel, Metallurgical and Materials Transactions B-Process Metallurgy and Materials Processing Science 29(1) (1998) 205-210.

[132] A. Gustafson, J. Agren, Modelling of carbo-nitride nucleation in 10% Cr steel, Acta Materialia 46(1) (1998) 81-90.

[133] L. Sproge, J. Argen, Journal of Heat Treatment 6 (1998) 9-19.

[134] J.O. Andersson, J. Agren, MODELS FOR NUMERICAL TREATMENT OF MULTICOMPONENT DIFFUSION IN SIMPLE PHASES, Journal of Applied Physics 72(4) (1992) 1350-1355.

[135] A. Borgenstam, A. Engstrom, L. Hoglund, J. Agren, DICTRA, a tool for simulation of diffusional transformations in alloys, Journal of Phase Equilibria 21(3) (2000) 269-280.

[136] J.C. Zhao, X. Zheng, D.G. Cahill, High-throughput diffusion multiples, Materials Today 8(10) (2005) 28-37.

[137] L. Onsager, Reciprocal relations in irreversible processes. I, Physical Review 37(4) (1931) 405-426.

[138] A. Engstrom, J. Agren, Assessment of diffusional mobilities in face-centered cubic Ni Cr Al alloys, Zeitschrift Fur Metallkunde 87(2) (1996) 92-97.

[139] Q.F. Zhang, J.C. Zhao, Extracting interdiffusion coefficients from binary diffusion couples using traditional methods and a forward-simulation method, Intermetallics 34 (2013) 132-141.

[140] J.S. Kirkaldy, D.J. Young, J.E. Lane, DIFFUSION PROFILES ASSOCIATED WITH THE ONSAGER MATRIX IN NONEQUILIBRIUM A-A-STAR-VACANCY AND A-B-VACANCY SOLUTIONS, Acta Metallurgica 35(6) (1987) 1273-1279.

[141] M.P. Gomez, D.A. Stevenson, R.A. Huggins, SELF-DIFFUSION OF PB AND TE IN LEAD TELLURIDE, Journal of Physics and Chemistry of Solids 32(2) (1971) 335-+.

[142] M.S. Seltzer, J.B. Wagner, DIFFUSION OF SULFUR 35 IN SINGLE CRYSTALS OF LEAD SULFIDE AS A FUNCTION OF STOICHIOMETRY AND DOPING ADDITIONS, Journal of Physics and Chemistry of Solids 26(2) (1965) 233-+.

[143] R. McGraw, THE THERMODYNAMIC BARRIER TO NUCLEATION NEAR A CRITICAL-POINT, Journal of Chemical Physics 91(9) (1989) 5655-5664.

[144] X.J. Liu, H.H. Hu, J.J. Han, Y. Lu, C.P. Wang, Assessment of the diffusional mobilities in fcc Ni-Nb and fcc Ni-Mo alloys, Calphad-Computer Coupling of Phase Diagrams and Thermochemistry 38 (2012) 140-145.

[145] R. Venkatasubramanian, E. Siivola, T. Colpitts, B. O'Quinn, Thin-film thermoelectric devices with high room-temperature figures of merit, Nature 413(6856) (2001) 597-602.

[146] T.J. Zhu, L.P. Hu, X.B. Zhao, J. He, New Insights into Intrinsic Point Defects in V2VI3 Thermoelectric Materials, Advanced Science 3(7) (2016).

[147] R.F. Brebrick, HOMOGENEITY RANGES AND TE2-PRESSURE ALONG 3-PHASE CURVES FOR BI2TE3(C) AND A 55-58-AT PERCENT TE PERITECTIC PHASE, Journal of Physics and Chemistry of Solids 30(3) (1969) 719-&.

[148] B.S. Sa, J. Zhou, Z.M. Sun, J. Tominaga, R. Ahuja, Topological Insulating in GeTe/Sb2Te3 Phase-Change Superlattice, Physical Review Letters 109(9) (2012).

[149] D. Loke, L.P. Shi, W.J. Wang, R. Zhao, H.X. Yang, L.T. Ng, K.G. Lim, T.C. Chong, Y.C. Yeo, Ultrafast switching in nanoscale phase-change random access memory with superlattice-like structures, Nanotechnology 22(25) (2011).

[150] J.W.G. Bos, H.W. Zandbergen, M.H. Lee, N.P. Ong, R.J. Cava, Structures and thermoelectric properties of the infinitely adaptive series (Bi-2)(m)(Bi2Te3)(n), Physical Review B 75(19) (2007).

[151] K. Kifune, Y. Kubota, T. Matsunaga, N. Yamada, Extremely long period-stacking structure in the Sb-Te binary system, Acta Crystallographica Section B-Structural Science 61 (2005) 492-497.

[152] T. Valla, H.W. Ji, L.M. Schoop, A.P. Weber, Z.H. Pan, J.T. Sadowski, E. Vescovo, A.V. Fedorov, A.N. Caruso, Q.D. Gibson, L. Muchler, C. Felser, R.J. Cava, Topological semimetal in a Bi-Bi2Se3 infinitely adaptive superlattice phase, Physical Review B 86(24) (2012).

[153] K. Govaerts, M.H.F. Sluiter, B. Partoens, D. Lamoen, Homologous series of layered structures in binary and ternary Bi-Sb-Te-Se systems: Ab initio study, Physical Review B 89(5) (2014).

[154] S.N. Chizhevskaya, L.E. Shelimova, V.S. Zemskov, V.I. Kosyakov, D.V. Malakhov, EXPERT ESTIMATION AND MATCHING OF DATA ON THE PHASE-DIAGRAM OF THE BI-TE SYSTEM, Inorganic Materials 30(1) (1994) 1-8.

[155] H. Okamoto, The Bi-Se (Bismuth-Selenium) System, Journal of Phase Equilibria, 1994, pp. 195-201.

[156] H. Okamoto, 1990, ASM International, Binary Alloy Phase Diagrams: Sb-Te (Antimony-Tellurium), pp. 3308-3310.

[157] C. Mao, M. Tn, L. Zhang, D. Wu, W. Bai, L. Liu, Experimental reinvestigation and thermodynamic description of Bi-Te
binary system CALPHAD, 2018, pp. 81-89.

[158] Y. Chen, Y.J. Liu, M.Y. Chu, L.J. Wang, Phase diagrams and thermodynamic descriptions for the Bi-Se and Zn-Se binary systems, Journal of Alloys and Compounds 617 (2014) 423-428.

[159] C.P. Guo, C.R. Li, Z.M. Du, Thermodynamic Re-modeling of the Sb-Te System Using Associate and Ionic Models, Journal of Electronic Materials 43(11) (2014) 4082-4089.

[160] M. Hansen, Constitution of binary alloys: Bi-Te Phase Diagram, McGraw-Hill
1958.

[161] N.K. Abrikosov, V.F. Bankina, ISSLEDOVANIE DIAGRAMMY SOSTOYANIYA SISTEMY BI-TE, Zhurnal Neorganicheskoi Khimii 3(3) (1958) 659-667.

[162] H. Okamoto, L.E. Tanner, Bi-Te (Bismuth-Tellurium), Binary Alloy Phase Diagrams 1 (1990) 800-801.

[163] G. Offergeld, J. Vancakenberghe, STOICHIOMETRY OF BISMUTH TELLURIDE AND RELATED COMPOUNDS, Nature 184(4681) (1959) 185-186.

[164] D. West, Y.Y. Sun, H. Wang, J. Bang, S.B. Zhang, Native defects in second-generation topological insulators: Effect of spin-orbit interaction on Bi2Se3, Physical Review B 86(12) (2012).

[165] L.L. Wang, M.L. Huang, S. Thimmaiah, A. Alam, S.L. Bud'ko, A. Kaminski, T.A. Lograsso, P. Canfield, D.D. Johnson, Native defects in tetradymite Bi-2(TexSe3-x) topological insulators, Physical Review B 87(12) (2013).

[166] B. Predel, J. Piehl, M.J. Pool, CONTRIBUTION TO THERMODYNAMIC PROPERTIES OF LIQUID BINARY-ALLOYS OF TE WITH SN, PB AND BI, Zeitschrift Fur Metallkunde 66(6) (1975) 347-352.

[167] Y. Feutelais, G. Morgant, B. Legendre, LIQUID-STATE ELECTROCHEMICAL STUDY OF BISMUTH TELLURIUM LIQUID ALLOYS, Journal of the Less-Common Metals 169(2) (1991) 197-207.

[168] T. Maekawa, T. Yokokawa, K. Niwa, ENTHALPIES OF MIXING IN LIQUID STATE - TL+TE AND BI+TE, Journal of Chemical Thermodynamics 3(1) (1971) 143-&.

[169] G. Morgant, Y. Feutelais, B. Legendre, R. Castanet, A. Coulet, THERMODYNAMIC BEHAVIOR OF BI-TE ALLOYS, Zeitschrift Fur Metallkunde 81(1) (1990) 44-48.

[170] S.K. Feng, S.M. Li, H.Z. Fu, First-principle calculation and quasi-harmonic Debye model prediction for elastic and thermodynamic properties of Bi2Te3, Computational Materials Science 82 (2014) 45-49.

[171] A.F. Zurhelle, V.L. Deringer, R.P. Stoffel, R. Dronskowski, Ab initio lattice dynamics and thermochemistry of layered bismuth telluride (Bi2Te3), Journal of Physics-Condensed Matter 28(11) (2016).

[172] N. Parravano, The System: Bismuth-Selenium, Gazzetta Chimica Italiana, 1913, pp. 201-209.

[173] N. Tomoshige, Metallographic Investigation of the System Bismuth-Selenium, Memoirs of the College of Science, Kyoto Imperial University, 1919, pp. 55-60.

[174] N.K. Abrikosov, V.F. Bankina, K.F. Kharitonovich, ISSLEDOVANIE DIAGRAMMY SOSTOYANIYA SISTEMY BI-SE, Zhurnal Neorganicheskoi Khimii 5(9) (1960) 2011-2016.

[175] T. Ohashi, Z. Kozuka, J. Moriyama, Vapor Pressure Measurements on Bismuth-Selenium Alloys, Nippon Kinzoku Gkkaishi, 1966, pp. 785-788.

[176] B. Gather, R. Blachnik, GOLD-BISMUTH SELENIUM SYSTEM, Zeitschrift Fur Metallkunde 66(6) (1975) 356-359.

[177] H. Bros, R. Castanet, H. Kehiaian, Calorimetric Study of the Bi-Se System, High temperatures - high pressures, 1976, pp. 271-278.

[178] A.A. Sher, I.N. Odin, A.V. Novoselova, PHASE INVESTIGATION IN THE BI-SE SYSTEM, Zhurnal Neorganicheskoi Khimii 31(3) (1986) 764-767.

[179] F.T. Huang, M.W. Chu, H.H. Kung, W.L. Lee, R. Sankar, S.C. Liou, K.K. Wu, Y.K. Kuo, F.C. Chou, Nonstoichiometric doping and Bi antisite defect in single crystal Bi2Se3, Physical Review B 86(8) (2012).

[180] J. Horak, Z. Stary, P. Lostak, J. Pancir, ANTI-SITE DEFECTS IN N-BI2SE3 CRYSTALS, Journal of Physics and Chemistry of Solids 51(12) (1990) 1353-1360.

[181] J. Horak, S. Karamazov, P. Lost'ak, Point defects in Pb-doped Bi2Se3 single crystals, Radiation Effects and Defects in Solids 140(2) (1997) 181-196.

[182] B. Predel, J. Piehl, M.J. Pool, CONTRIBUTION TO UNDERSTANDING OF THERMODYNAMIC PROPERTIES OF LIQUID TL-SE-ALLOYS, BI-SE-ALLOYS AND SB-SE-ALLOYS, Zeitschrift Fur Metallkunde 66(7) (1975) 388-395.

[183] T. Maekawa, T. Yokokawa, K. Niwa, ENTHALPIES OF MIXING IN LIQUID STATE .4. BI+SE AND SB+SE, Journal of Chemical Thermodynamics 4(6) (1972) 873-&.

[184] A.S. Pashinkin, A.S. Malkova, Heat capacity of solid bismuth selenide (Bi2Se3), Russian Journal of Physical Chemistry 79(7) (2005) 1169-1171.

[185] S.M. Rasulov, COMPONENTS OF THE HEAT-CAPACITY OF THE COMPOUNDS AIVSE AND A2 VSE3, High Temperature 26(1) (1988) 70-75.

[186] R. Blachnik, A. Schneider, High-temperature enthalpies of As2Te3, Sb2Se3, Bi2Se3, GeAs, GeAs2, and SnAs, The Journal of Chemical Thermodynamics 3(2) (1971) 227-233.

[187] B.M. Gol'tsman, V.A. Kudinov, I.A. Smirnov, Semiconductor Thermoelectic Materials on the Bi2Te3 Base, Semiconducting Thermoelectric Materials Based on Bi2Te3 3(11) (1972).

[188] A.V. Antipov, E.B. Rudnyi, Z.V. Dobrokhotova, Thermodynamic evaluation of the Bi-Se system, Inorganic Materials 37(2) (2001) 126-132.

[189] M. Hansen, Constitution of Binary Alloys: Sb-Te, McGraw-Hill, 1958
pp. 1177-1178.

[190] N.K. Abrikosov, L.V. Poretskaya, I.P. Ivanova, ISSLEDOVANIE SISTEMY SURMA TELLUR, Zhurnal Neorganicheskoi Khimii 4(11) (1959) 2525-2530.

[191] G. Ghosh, H.L. Lukas, L. Delaey, A THERMODYNAMIC ASSESSMENT OF THE SB-TE SYSTEM, Zeitschrift Fur Metallkunde 80(10) (1989) 731-736.

[192] L.V. Poretskaya, N.K. Abrikosov, V.M. Glazov, ISSLEDOVANIE SISTEMY SB-TE V OBLASTI SOEDINENIYA SB2TE3 V TVERDOM I ZHIDKOM SOSTOYANIYAKH, Zhurnal Neorganicheskoi Khimii 8(5) (1963) 1196-&.

[193] Y.P. Jiang, Y.Y. Sun, M. Chen, Y.L. Wang, Z. Li, C.L. Song, K. He, L.L. Wang, X. Chen, Q.K. Xue, X.C. Ma, S.B. Zhang, Fermi-Level Tuning of Epitaxial Sb2Te3 Thin Films on Graphene by Regulating Intrinsic Defects and Substrate Transfer Doping, Physical Review Letters 108(6) (2012).

[194] Y. Feutelais, B. Legendre, G. Morgant, ENTHALPIES OF FORMATION FOR THE ANTIMONY-TELLURIUM SYSTEM AT 909.30-K, 911.85-K AND 917.95-K, Journal of Thermal Analysis 34(4) (1988) 1093-1100.

[195] T. Maekawa, K. Niwa, T. Yokokawa, ENTHALPIES OF MIXING IN LIQUID STATE .3. IN + TE AND SB + TE, Journal of Chemical Thermodynamics 4(1) (1972) 153-&.

[196] B. Onderka, K. Fitzner, THERMODYNAMIC STUDY OF SB-TE ALLOYS BY EMF-MEASUREMENTS USING SOLID ZIRCONIA ELECTROLYTE, Zeitschrift Fur Metallkunde 86(5) (1995) 313-318.

[197] B.W. Howlett, M.B. Bever, S. Misra, ON THERMODYNAMIC PROPERTIES OF COMPOUNDS SB2SE3 SB2TE3 + B12TE3, Transactions of the Metallurgical Society of Aime 230(6) (1964) 1367-&.

[198] Y.I. Gerasimov, A.V. Nikoskaya, Problems of the Metallurgy and Physics of Semiconductorss (1961).

[199] A.A. Vecher, L.A. Mechkovskii, A.S. Skoropanov, Determination of the heats of formation of certain tellurides, Zh. Fiz. Khim. 45 (1974) 1615.

[200] L.E. Shelimova, O.G. Karpinskii, V.I. Kosyakov, V.A. Shestakov, V.S. Zemskov, F.A. Kuznetsov, Homologous series of layered tetradymite-like compounds in Bi-Te and GeTe-Bi2Te3 systems, Journal of Structural Chemistry 41(1) (2000) 81-87.

[201] G. Kresse, J. Hafner, ABINITIO MOLECULAR-DYNAMICS FOR LIQUID-METALS, Physical Review B 47(1) (1993) 558-561.

[202] N.P. Gorbachuk, A.S. Bolgar, V.R. Sidorko, L.V. Goncharuk, Heat capacity and enthalpy of Bi2Si3 and Bi2Te3 in the temperature range 58-1012 K, Powder Metallurgy and Metal Ceramics 43(5-6) (2004) 284-290.

[203] S. Bordas, M.T. Clavagueramora, B. Legendre, C. Hancheng, PHASE-DIAGRAM OF THE TERNARY-SYSTEM GE-SB-TE .2. THE SUBTERNARY GE-GETE-SB2TE3-SB, Thermochimica Acta 107 (1986) 239-265.

[204] A. Brown, B. Lewis, SYSTEMS BISMUTH-TELLURIUM AND ANTIMONY-TELLURIUM AND SYNTHESIS OF MINERALS HEDLEYITE AND WEHRLITE, Journal of Physics and Chemistry of Solids 23(11) (1962) 1597-&.

[205] V.R. Sidorko, L.V. Goncharuk, R.V. Antonenko, Thermodynamic properties of bismuth sesquiselenide and sesquitelluride and their solid solutions, Powder Metallurgy and Metal Ceramics 47(3-4) (2008) 234-241.

[206] Y.I. Gerasimov, A.V. Nikolskaya, V.A. Geiderikh, E.M.F. study of thermodynamic properties of some semiconductor alloys, Chemical Bonds in Semiconductors and Solids (1965) 113-121.

[207] G. Offergeld, J. Vancakenberghe, DETERMINATION DE LA COMPOSITION A FUSION CONGRUENTE DE SEMICONDUCTEURS BINAIRES PAR ANALYSE THERMIQUE DIFFERENTIELLE - APPLICATION A BI2TE3, SB2TE3 ET BI2SE3, Journal of Physics and Chemistry of Solids 11(3-4) (1959) 310-314.

[208] D. Lide, CRC Handbook of Chemistry and Physics, CRC Press/Taylor & Frances 98 (2018) 95-124.

[209] H.S. Kim, N.A. Heinz, Z.M. Gibbs, Y.L. Tang, S.D. Kang, G.J. Snyder, High thermoelectric performance in (Bi0.25Sb0.75)(2)Te-3 due to band convergence and improved by carrier concentration control, Materials Today 20(8) (2017) 452-459.

[210] T. Caillat, M. Carle, P. Pierrat, H. Scherrer, S. Scherrer, THERMOELECTRIC PROPERTIES OF (BIXSB1-X)2TE3 SINGLE-CRYSTAL SOLID-SOLUTIONS GROWN BY THE THM METHOD, Journal of Physics and Chemistry of Solids 53(8) (1992) 1121-1129.

[211] J.P. Fleurial, L. Gailliard, R. Triboulet, H. Scherrer, S. Scherrer, THERMAL-PROPERTIES OF HIGH-QUALITY SINGLE-CRYSTALS OF BISMUTH TELLURIDE .1. EXPERIMENTAL CHARACTERIZATION, Journal of Physics and Chemistry of Solids 49(10) (1988) 1237-1247.

[212] S. Il Kim, K.H. Lee, H.A. Mun, H.S. Kim, S.W. Hwang, J.W. Roh, D.J. Yang, W.H. Shin, X.S. Li, Y.H. Lee, G.J. Snyder, S.W. Kim, Dense dislocation arrays embedded in grain boundaries for high-performance bulk thermoelectrics, Science 348(6230) (2015) 109-114.

[213] Y.L. Tang, S.W. Chen, G.J. Snyder, Temperature dependent solubility of Yb in Yb-CoSb3 skutterudite and its effect on preparation, optimization and lifetime of thermoelectrics, Journal of Materiomics 1(1) (2015) 75-84.

[214] S.H. Lo, J.Q. He, K. Biswas, M.G. Kanatzidis, V.P. Dravid, Phonon Scattering and Thermal Conductivity in p-Type Nanostructured PbTe-BaTe Bulk Thermoelectric Materials, Advanced Functional Materials 22(24) (2012) 5175-5184.

[215] Y.L. Pei, G.J. Tan, D. Feng, L. Zheng, Q. Tan, X.B. Xie, S.K. Gong, Y. Chen, J.F. Li, J.Q. He, M.G. Kanatzidis, L.D. Zhao, Integrating Band Structure Engineering with All-Scale Hierarchical Structuring for High Thermoelectric Performance in PbTe System, Advanced Energy Materials 7(3) (2017).

[216] M.J. Yin, D. Wu, J.Q. He, Evolvement of microstructure and lattice thermal conductivity in Na doped PbTe-PbS pseudo-binary system, Journal of Materiomics 2(2) (2016) 150-157.

[217] J. Callaway, H.C. Vonbaeyer, EFFECT OF POINT IMPERFECTIONS ON LATTICE THERMAL CONDUCTIVITY, Physical Review 120(4) (1960) 1149-1154.

[218] N. Mingo, D. Hauser, N.P. Kobayashi, M. Plissonnier, A. Shakouri, "Nanoparticle-in-Alloy" Approach to Efficient Thermoelectrics: Silicides in SiGe, Nano Letters 9(2) (2009) 711-715.

[219] B. Abeles, LATTICE THERMAL CONDUCTIVITY OF DISORDERED SEMICONDUCTOR ALLOYS AT HIGH TEMPERATURES, Physical Review 131(5) (1963) 1906-&.

[220] H. Zhang, A.J. Minnich, The best nanoparticle size distribution for minimum thermal conductivity, Scientific Reports 5 (2015).

[221] K. Biswas, J.Q. He, I.D. Blum, C.I. Wu, T.P. Hogan, D.N. Seidman, V.P. Dravid, M.G. Kanatzidis, High-performance bulk thermoelectrics with all-scale hierarchical architectures, Nature 489(7416) (2012) 414-418.

[222] K. Kishimoto, T. Koyanagi, Preparation of sintered degenerate n-type PbTe with a small grain size and its thermoelectric properties, Journal of Applied Physics 92(5) (2002) 2544-2549.

[223] L.D. Zhao, H.J. Wu, S.Q. Hao, C.I. Wu, X.Y. Zhou, K. Biswas, J.Q. He, T.P. Hogan, C. Uher, C. Wolverton, V.P. Dravid, M.G. Kanatzidis, All-scale hierarchical thermoelectrics: MgTe in PbTe facilitates valence band convergence and suppresses bipolar thermal transport for high performance, Energy & Environmental Science 6(11) (2013) 3346-3355.

[224] Y.I. Ravich, B.A. Efimova, I.A. Smirnov, Semiconducting Lead Chalcogenides, Plenum Press (1970).

[225] A.F. May, E.S. Toberer, A. Saramat, G.J. Snyder, Characterization and analysis of thermoelectric transport in n-type Ba8Ga16-xGe30+x, Physical Review B 80(12) (2009).

[226] H.J. Jou, PrecipiCalc Software User Guide, QuesTek Innovations LLC 0.9.4 (2012).

[227] H.J. Jou, P. Voorhees, G.B. Olson, Computer simulations for the prediction of microstructure/property variation in aeroturbine disks, Superalloys 2004 (2004) 877-886.

[228] D.M. Collins, B.D. Conduit, H.J. Stone, M.C. Hardy, G.J. Conduit, R.J. Mitchell, Grain growth behaviour during near-gamma ' solvus thermal exposures in a polycrystalline nickel-base superalloy, Acta Materialia 61(9) (2013) 3378-3391.

[229] J.Q. He, I.D. Blum, H.Q. Wang, S.N. Girard, J. Doak, L.D. Zhao, J.C. Zheng, G. Casillas, C. Wolverton, M. Jose-Yacaman, D.N. Seidman, M.G. Kanatzidis, V.P. Dravid, Morphology Control of Nanostructures: Na-Doped PbTe-PbS System, Nano Letters 12(11) (2012) 5979-5984.

[230] A.L. Rocha, I.G. Solrzano, J.B.V. Sande, Heterogeneous and homogeneous nanoscale precipitation in dilute Cu-Co alloys, Materials Science & Engineering C-Biomimetic and Supramolecular Systems 27(5-8) (2007) 1215-1221.

[231] H. Ramanarayan, T.A. Abinandanan, Grain boundary effects on spinodal decomposition II. Discontinuous microstructures, Acta Materialia 52(4) (2004) 921-930.

[232] L. Amirouche, M. Plapp, Phase-field modeling of the discontinuous precipitation reaction, Acta Materialia 57(1) (2009) 237-247.

[233] S.N. Girard, K. Schmidt-Rohr, T.C. Chasapis, E. Hatzikraniotis, B. Njegic, E.M. Levin, A. Rawal, K.M. Paraskevopoulos, M.G. Kanatzidis, Analysis of Phase Separation in High Performance PbTePbS Thermoelectric Materials, Advanced Functional Materials 23(6) (2013) 747-757.

[234] L. Rayleigh, Proceedings of the London Math Society 10 (1878) 4.

[235] S. Karim, M.E. Toimil-Molares, A.G. Balogh, W. Ensinger, T.W. Cornelius, E.U. Khan, R. Neumann, Morphological evolution of Au nanowires controlled by Rayleigh instability, Nanotechnology 17(24) (2006) 5954-5959.

[236] C. Joshi, T.A. Abinandanan, A. Choudhury, Phase field modelling of rayleigh instabilities in the solid-state, Acta Materialia 109 (2016) 286-291.